2016

Bidirectional Distribution Reflection Function of Algodones Dunes

Mahesh Shrestha
South Dakota State University

BIDIRECTIONAL REFLECTION DISTRIBUTION FUNCTION OF THE ALGODONES DUNES

BY

MAHESH SHRESTHA

A thesis submitted in partial fulfillment of the requirements for the

Master of Science

Major in Electrical Engineering

South Dakota State University

2016

BIDIRECTIONAL REFLECTION DISTRIBUTION FUNCTION OF ALGODONES DUNES

This thesis is approved as a creditable and independent investigation by a candidate for the Master of Science in Electrical Engineering degree and is acceptable for meeting the thesis requirements for this degree. Acceptance of this thesis does not imply that the conclusions reached by the candidates are necessarily the conclusions of the major department.

Larry Leigh
Thesis Advisor Date

Dennis Helder, Ph.D.
Major Advisor Date

Steven Hietpas, Ph.D.
Head, Electrical Engineering and Computer Science Date

Dean, Graduate School Date

ACKNOWLEDGEMENTS

My first thanks goes to my major advisor, Dr.Dennis Helder, for the support and encouragement he gave me during my stay at South Dakota State University. His constant confidence in me and my work has been an inspiration for me and he has also surrounded me with the people and technology that made the work possible. I would also like to thank my advisor Larry Leigh, whose wisdom and encouragement are responsible for guiding me in right direction. I am also greatly indebted to Dave Aaron and Morakot Kaewmanee for their constant help throughout the project.

Special thanks to Dr.Gary Hatfield and Joseph Robertson for giving me proper guidance in rigorous statistical analysis.

I would like to thank Shiva Poudel and Bijen Shrestha for helping me with LaTeX. My special thanks goes to Leah Ervin for her tremendous help in improving my thesis writing and providing valuable comments. I would also like to acknowledge SDSU Image Processing Lab crew for improving me by giving valuable feedback and advice.

I would like to dedicate this thesis to my father Madan Shrestha and mother Bishnu Shrestha.

Finally, I am grateful to my brother Manoj Shrestha, Rojesh Maharjan, Manisha Maharjan, Prajina Tandukar, Lekhnath Kafle, Lok Raj Joshi and Sudeep Ghimire for their constant inspiration and support.

CONTENTS

ABBREVIATIONS

ANIF	Anisotropy Factor
ASD	Analytical Spectral Device
BRDF	Bidirectional Reflectance Distribution Function
BRF	Bidirectional Reflectional Factor
CEOS	International Committee on Earth Observation Satellite
FIGOS	Field Goniometer
GOPHER	Goniometer For Outdoor Portable Hyperspectral Earth Reflectance
LMM	Linear Mixed Model
NIR	Near Infrared
NIST	National Institute of Standards and Technology
OLI	Operational Land Imager
PCA	Principal Component Analysis
PICS	Pseudo Invariant Calibration Site
QQ	Quantile Quantile
RSR	Relative Spectral Response
SFG	Sandmeirer Field Gonimeter
SMACAA	SDSU MODTRAN ATMOSPHERIC CORRECTION ANYWHERE ANYTIME
SWIR	Shortwave Infrared
TOA	Top of Atmosphere

ULB	University of Lethbridge
ULGS	University of Lethbridge Goniometer System
VZA	View Zenith Angle
WGCV	Working Group on Calibration

LIST OF FIGURES

LIST OF TABLES

ABSTRACT

BIDIRECTIONAL REFLECTION DISTRIBUTION FUNCTION OF THE ALGODONES DUNES

MAHESH SHRESTHA

2016

The primary objective of this project was to develop the Algodones Dunes as a pseudo-invariant calibration site (PICS) suitable for absolute calibration of satellite sensors based on a surface reflectance model. Two approaches were taken during this research: a field campaign and laboratory measurements.

The first approach, the field campaign, was accomplished with a trip to the Algodones Dunes from the 8^{th} to the 13^{th} of March, 2015. During the field campaign, several test points from spatially different regions of the Algodones Dunes were studied. Reflectance of the sand at each test point was observed from different view angles.

The second approach, laboratory testing, involved bringing several sand samples from different regions of the Algodones Dunes back to SDSU for further analysis. The laboratory setup was built in the SDSU optics laboratory and included the use of a light source, digital power supply, and mechanical arm to study the spectral responses of the sand samples from the field. During the laboratory measurements, the reflectance of each of the sand sample, was observed from different view angles to replicate field measurement techniques. Through both approaches it was found that the reflectance of sand samples from the Algodones Dunes changes quadratically with respect to view zenith angle.

To correlate field and laboratory measurements, two solar zenith angles were chosen for laboratory simulation, i.e. 45° and 54.4°. Since the solar zenith angle varies from 20° to 60° over a year in the Algodones Dunes, angles within that range were chosen for the solar zenith angles used in the laboratory measurements. The spectral response of different sand samples were only observed under those two chosen solar zenith angles. Since different equipment was used in the laboratory than in the field, there was some degree of uncertainty due to each of the differing instruments which influenced the data. A Linear Mixed Model was therefore developed in order to incorporate the laboratory uncertainties and predict a more accurate model using the raw data acquired in the laboratory. The data modeled by the Linear Mixed Model approach for different BRDF runs of the same sample, and for different sand samples, were compared to determine whether the spectral response of sand samples from the Algodones Dunes is the same or not. Based on the data modeled by the Linear Mixed Model, it was found that the spectral responses of sand samples brought from the Algodones Dunes are the same. A simple BRDF model was then developed for those angles that are perpendicular to the principal plane of the solar illumination.

CHAPTER 1 INTRODUCTION

1.1 Remote Sensing and Its Applications

Remote Sensing is the science of the acquisition of information about an object or area without having intimate contact with the object or area [1]. Remote sensors acquire information by sensing the emitted or reflected energy from an object.

Satellite remote sensing involves gathering information about the features of the earth from orbiting satellites in a repetitive and consistent manner to monitor the short-term and long-term changes on the Earth's surface. Remotely sensed data acquired by earth observation satellites provide a number of benefits for studying the Earth's surface, including [2]:

- Continuous acquisition of data
- Regular revisit capabilities with broad regional coverage
- High spectral and spatial resolution
- Ability to manipulate/enhance digital data
- Ability to combine satellite digital data with other digital data

1.2 Optical Imaging System

In optical remote sensing, sensors sensitive to different wavelengths are used to form an image of the earth by detecting the amount of radiation reflected or emitted by the earth's surface. Since different objects absorb and reflect the light differently in different wavelengths, objects can be distinguished by observing their spectral signature. Optical imaging systems are categorized on the basis of numbers of spectral bands used: In a

multispectral imaging system, the sensor has detectors sensitive to a few spectral bands. Since each channel is sensitive to an assigned narrow wavelength band, an image is captured with different wavelength ranges. Hyperspectral imaging system consists of hundreds of continuous spectral bands. So finer details of the target can be observed, which helps for better characterization of the target.

1.3 Remote Sensor

A remote sensor is a device which measures the electromagnetic energy reflected by the earth's surface, and thus can determine intrinsic properties of an object remotely. A remote sensor can be classified into two categories:

1.3.1 Active Remote Sensor

Active sensors are those sensors which have their own source, that can artificially radiate energy as shown in Figure 1.1. These sensors emit the energy and detect the amount of reflected energy from an object, examples include Lidar and Radar. One of the advantages of the active sensor over the passive sensor is it can take the measurement at any time regardless of day or night. It can also be used for examining wavelengths that are not sufficiently provided by the sun, like microwaves.

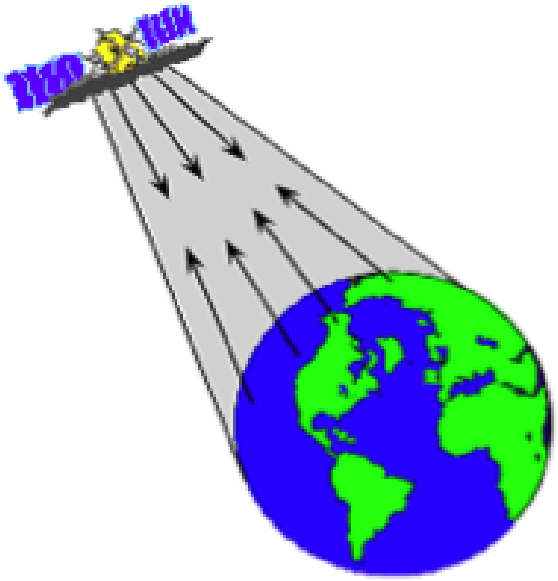

Figure 1.1. Active sensor [3].

1.3.2 Passive Remote Sensor

A passive remote sensor doesn't have its own source; it depends on external sources of energy, usually the sun as shown in Figure 1.2. It detects the reflected amount of electromagnetic radiation from an object.

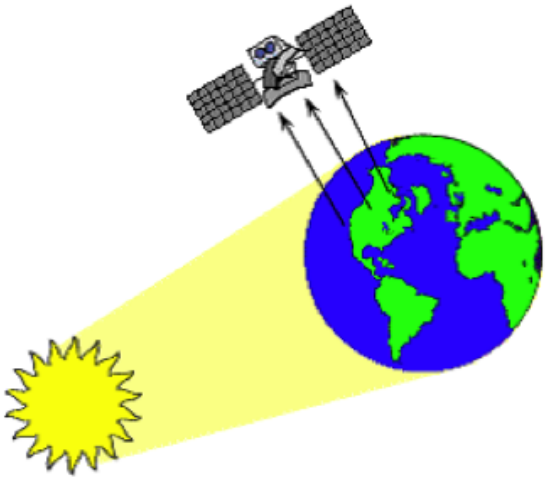

Figure 1.2. Passive sensor [3].

1.4 Interaction with the Atmosphere

Electromagnetic radiation used for remote sensing has to travel through the Earth's atmosphere before reaching the Earth's surface. The gases and particles present in the atmosphere will affect electromagnetic energy propagating through it, allowing electromagnetic energy to pass at certain wavelengths and absorbing energy at certain wavelengths. The ability of the atmosphere to allow radiation to pass through it is referred to as its transmissivity, which varies with the wavelength of the radiation [4].

1.4.1 Scattering

Atmospheric scattering is one of the crucial reasons why electromagnetic energy is lost as it propagates through the atmosphere. Molecules present in the atmosphere disturb the electromagnetic field of the propagating beam. As a result, the direction and spectral distribution of the energy in the beam changes. Scattering in the atmosphere depends on several factors such as the wavelength of the radiation, the abundance of particles or gases and the distance travelled by radiation through the atmosphere. Generally, scattering is categorized into three groups:

1.4.1.1 Rayleigh Scattering

Rayleigh scattering occurs when the particles are very small, as compared to the wavelength of the radiation, like nitrogen and oxygen molecules. The percentage of light scattered is inversely proportional to the fourth power of the wavelength of the radiation, so smaller particles will scatter a higher percentage of shorter wavelength light compared to longer wavelength light. Rayleigh scattering also describes two phenomena which is observed daily. Since short wavelength energy will be scattered more than the long

wavelength energy, this causes the sky to appear blue. At sunrise and sunset, light has to travel a much longer distance through the atmosphere, than in the day, so the shorter wavelength largely scatter out leaving a greater portion of longer wavelength light to penetrate the atmosphere. This is why the Sun appears red at sunrise and sunset.

1.4.1.2 Mie Scattering

Mie-Scattering occurs when particle size is about the same size as the wavelength of the radiation, examples include water vapor, dust, and smoke. Mie scattering is not as strongly dependent on the wavelength of radiation.

1.4.1.3 Non-Selective Scattering

Non-selective scattering occurs when the particle size is much larger than the wavelength of the radiation like water droplets and large dust particles. This scattering gets its name from the fact that it scatters all wavelengths of light equally. Since this type of scattering scatters the visible light equally, the color of clouds and fog appears to be white.

1.4.2 Absorption

Absorption is another main phenomenon that affects electromagnetic radiation propagating through the atmosphere. Absorption is defined as removal of energy from the beam by conversion of electromagnetic energy to another form of energy. This results in the absorption of photons of selected energy levels by the constituent molecules in the atmosphere. Due to these phenomena, molecules of the atmosphere absorb energy at particular wavelengths and allow energy to pass at other wavelengths.

Several gases in the atmosphere absorb the electromagnetic energy in selected

portions of the electromagnetic spectrum. For remote sensing, such portions of the electromagnetic spectrum which are not severely affected by absorption, are called atmospheric windows as shown in Figure 1.3.

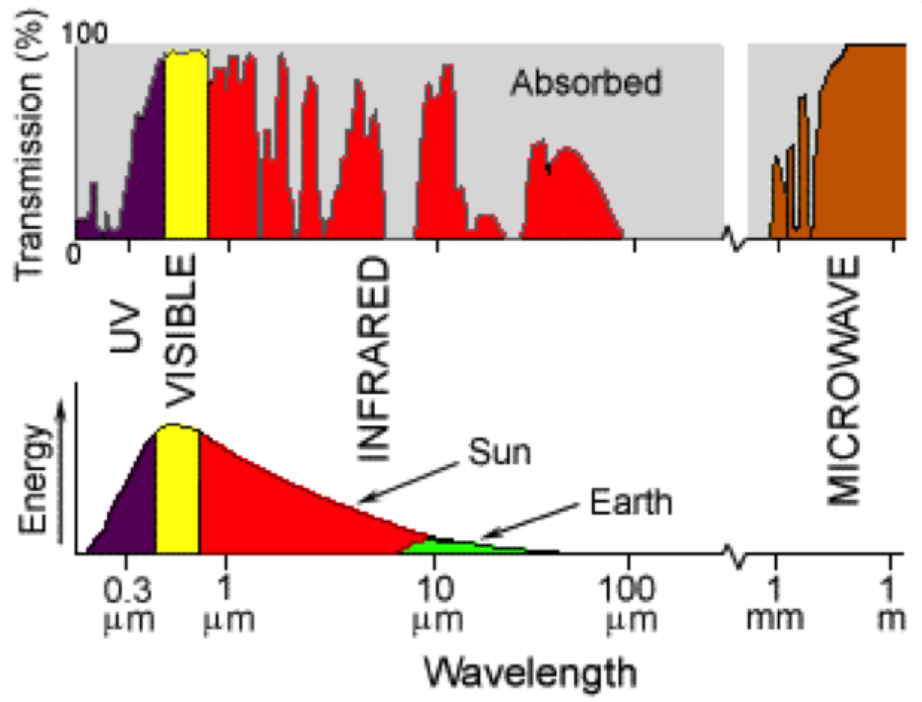

Figure 1.3. Atmospheric transmission.

Atmospheric windows are the ranges of wavelength which can be used for remote sensing. The visible portion of the spectrum, to which our eyes are most sensitive, corresponds to both an atmospheric window and the peak energy of the sun. Note also that heat energy emitted by the Earth corresponds to a window around 10 micrometers in the thermal IR portion of the spectrum, while the large window at wavelengths beyond 1 mm is associated with the microwave region [2].

1.5 Radiometric Parameters

Radiometry is defined as the science of characterizing how much electromagnetic energy is associated with a particular location or direction in space. Radiometric image

analysis involves a quantitative assessment of the energy or flux recorded by an imaging system and some form of reverse engineering to determine the parameters that control the energy levels observed [1]. Some radiometric parameters, which help for better understanding of electromagnetic radiation, are as follows:

1.5.1 Radiant Flux (ϕ)

Radiant Flux is defined as the rate of flow of radiant energy. It is also defined as the first derivative of the radiant energy with respect to time [1].

$$\phi = \frac{dQ}{dt}[Watt, w] \tag{1.1}$$

Irradiance (E) and Exitance (M)

Irradiance is defined as radiant flux onto the surface [1]. Mathematically, it is expressed as:

$$E = E(x,y) = \frac{d\phi}{dA}[wm^{-2}] \tag{1.2}$$

where dA [m^2] is the area of the interested surface.

Radiant Exitance is very similar to irradiance. Irradiance is used to describe incoming light whereas exitance is used to describe outgoing light. So Radiant Exitance is defined as radiant flux away from the surface. Mathematically, it is expressed as,

$$M = M(x,y) = \frac{d\phi}{dA}[wm^{-2}] \tag{1.3}$$

1.5.2 Radiant Intensity (I)

Radiant Intensity describes the flux per unit solid angle from a point source to a specific direction. Mathematically, radiant intensity is expressed as:

$$I = (\theta, \phi) = \frac{d\phi}{d\Omega}[wsr^{-1}] \tag{1.4}$$

Irradiance and Exitance have only spatial information but not any directional information. Radiant Intensity provides the directional information of radiant flux.

1.5.3 Radiance (L)

Radiance is the radiant flux that passes through a surface per unit solid angle per unit projected area. Mathematically, radiance is expressed as:

$$L = L(x, y, \theta, \phi) = \frac{d^2\phi}{dAcos\theta d\Omega} \tag{1.5}$$

Since it has both spatial and directional information about radiant flux, it is the most useful and ubiquitous term in radiometry. Electromagnetic radiation, which is not absorbed and scattered by the atmosphere, reaches and interacts with the Earth's surface. There are three phenomena that could take place when electromagnetic radiation interacts with Earth's surfaces and they are as follows:

1.5.4 Reflectance

Reflectance is the fraction of incident radiant energy that is reflected off an interface. It can be expressed as the ratio of exitance from the front of the surface to the

irradiance on the front of the surface. It is also shown in Figure 1.4

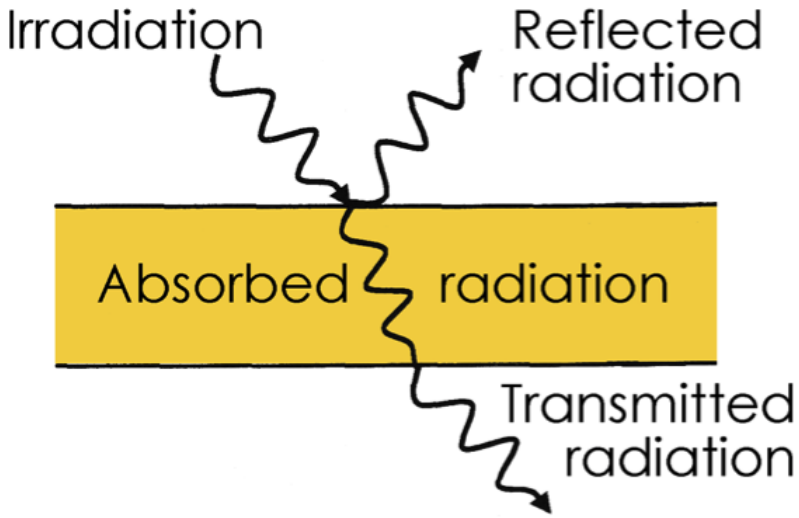

Figure 1.4. Extinction of radiation(absorption, transmission and reflection)

$$R = \frac{M_r}{E_i} \tag{1.6}$$

1.5.5 Absorption

Absorption is the reduction in intensity of radiant energy as it passes through certain medium. The absorbed energy is converted in another form of energy, typically heat. It can be expressed as the amount of incident radiant energy that is converted to another form of energy to the irradiance onto the surface.

$$\alpha = \frac{M_\alpha}{E_i} \tag{1.7}$$

1.5.6 Transmittance

Transmittance is the fraction of incident radiant energy that is transmitted through a medium. It can be expressed as the ratio of exitance from the back of the surface to the irradiance to the front of the surface.

$$\tau = \frac{M_\tau}{E_i} \tag{1.8}$$

1.6 Bidirectional Reflectance Distribution Function(BRDF)

Taking a closer look at the reflectance of light off a medium, the bidirectional reflectance distribution function (BRDF) is an expression of the physical property of a material, which describes the pattern of light reflected from a surface of the material to all directions of incident light. BRDF values will also change as a function of wavelength so the complete characterization of BRDF would include wavelength. It is a five-dimensional function. For any target, BRDF determines the appearance of a target from different viewing angles.

The geometry of bidirectional process is shown in Figure 1.5. The incident light on the surface is from the direction (θ_i,ϕ_i) and the light is reflected in the direction (θ_r,ϕ_r).

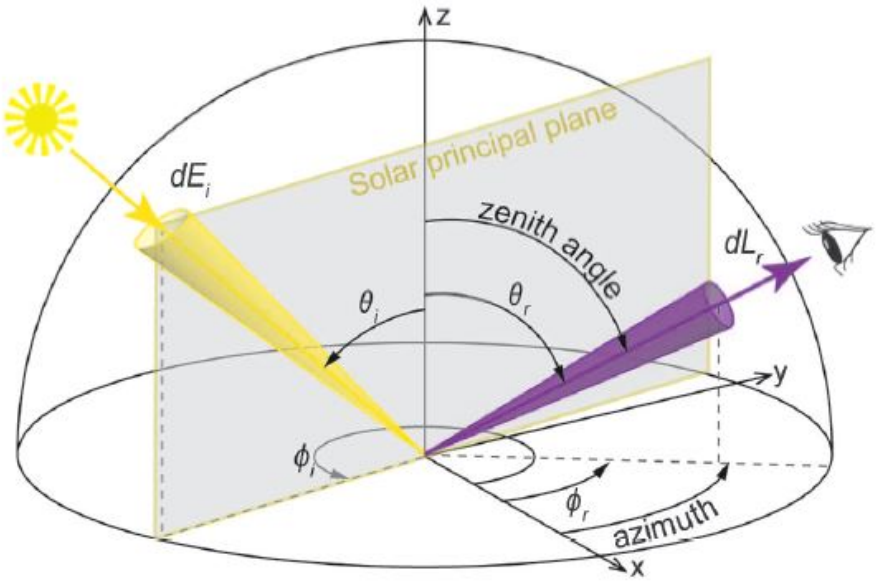

Figure 1.5. Concept of incident and reflected angles in spherical coordinate system [5]

The bidirectional reflection distribution function is given by the ratio of the radiance scattered into the direction described by the orientation angles θ_r,ϕ_r to the irradiance from θ_i,ϕ_i direction.

$$r_{BRDF}(\theta_r, \phi_r, \theta_i, \phi_i, \lambda) = \frac{L(\theta_r, \phi_r)}{E(\theta_i, \phi_i)}[sr^{-1}] \tag{1.9}$$

1.7 Calibration

In the context of remote sensing, the Working Group on Calibration and Validation (WGCV) of the International Committee on Earth Observation Satellites (CEOS) defines calibration as "the process of quantitatively defining the system response to known controlled signal inputs" [6]. Earth observation satellite sensors provide a repetitive and consistent view of the earth that is invaluable to monitor the dynamic changes of the Earth's surface over a long period of time. The image observed by the satellite needs to be calibrated to remove radiometric and geometric artifacts before using the imagery. These

artifacts are caused by many factors such as sensor degradation over the life of the satellite, optical aberrations or misalignment of multiple detectors and atmospheric influence [7]. Satellite calibration is a vital process in the field of remote sensing used to derive reliable and accurate quantitative measurements of the ground surface and also to compare data obtained from different satellite sensors [8]. Thus satellite calibration should be done frequently during the lifetime of a satellite to determine the accuracy of the data acquired by the satellite sensor [9]. As remote sensing has become more quantitative over time, sensor calibration has become an important issue for quantitative temporal studies of surface features [10]. Furthermore, absolute calibration is needed to find the degradation of the sensor because, without proper sensor calibration, the temporal changes of any surfaces viewed by the sensor could be masked by the degrading performance of the sensor.

Prior to launch, satellites are calibrated in a lab. The main objective of pre-launch calibration is to ensure that satellite sensors meet the desired specifications for radiometric accuracy before they are placed into orbit. Also, laboratory calibrations are easier to perform and control than calibration after the satellite has been placed in orbit [7]. A satellite sensor is generally calibrated several months or years before launch. The characteristics of satellite sensors, spectral filters, and other electronic equipment may change during the time between calibration and launch. Furthermore, after launch the sensor is in a new environment and aging may take place which ultimately leads to the degradation of the responsivity of a sensor over its lifetime [6]. So, in order to trace the performance of the sensors on a satellite, post-launch calibration is also important. Both onboard calibration instruments and ground reference targets are used for post-launch

calibration [11]. On-board calibration sources are any device present on the platform or connected to the sensor that supplies a known output to the sensor [12], while ground reference targets refer to Pseudo-Invariant Calibration Sites (PICS), or vicarious calibration sites. Typically onboard systems include direct solar illumination, solar diffusers, and onboard lamps [10]. The advantage of using onboard calibration systems is that calibration can be performed with high temporal frequency. The main problem associated with onboard calibration is the degradation of the onboard calibration system over time. Measurements taken from these on-board calibrators allow radiometric gains to be calculated which can be applied to sensor data [13]. Since the degradation of online calibrators from aging and other effects limit the accuracy, ground-based calibration has become widely adopted as a means to provide independent assurance of the quality of remotely sensed data. Any in-flight methods that do not use an onboard calibrator for calibration are known as vicarious calibration [10]. To get rid of the problem caused by degradation of a sensor over time, vicarious calibration provides an independent technique for absolute calibration using a full-system, full-aperture approach [10]. Some major disadvantages of vicarious calibration are that it requires manpower and it limits the number of vicarious calibration opportunities in a given timeframe.

PICS have been shown to be an excellent independent source of radiometric calibration due to their high spatial and temporal stability [14]. Typically, pseudo-invariant sites are located in arid regions where very little temporal and spatial change occurs over long periods of time [14]. Ideal PICS are located at high altitudes with reduced atmospheric effects and are nearly Lambertian [15]. Lambertian surface are those surface whose brightness appears uniform from all view angles. However, in the real

world, these criteria may not always be met. Even if such a site on the Earth was found, the invariant site technique may not be applicable due to lack of sufficient data acquisitions from the site. So, selection of invariant sites requires spatial and temporal stability as well as adequate cloud-free data collection from the site on a repetitive basis [16].

1.8 Need for BRDF Modeling

Deserts are used frequently to calibrate the optical satellite sensors because of their low temporal variability (less than 3% approaching to 1%). The calibration of airborne and satellite remote sensing sensors is a fundamental step in the rigorous validation of products derived from satellite data [17]. After the cross-calibration of Landsat MSS sensors done by Helder et.al, uncertainties associated with this calibration were found to be within 5% [17]. In order to improve the use of PICS for calibration, small variability in that site should be studied carefully. Atmosphere and BRDF are the main sources of uncertainty in the cross-calibration of a satellite using these sites. If the atmospheric effect and BRDF of these sites are well understood then the uncertainty of the cross-calibration using these sites can be brought down to less than 5%. In order to understand the surface reflectance of one of the PICS sites, preliminary field measurement was done at the Algodones Dunes.Those data can provide a better understanding of the reflective properties of the sand of the Algodones Dunes which can be used for the better calibration purposes. Although Algodones Dunes is not the best PICS in the world, it's location provides easy access for on site investigation and collection of ground validation data.

1.9 Organization of Thesis

The rest of the thesis will be as follows. Chapter 2 gives review of previous work done for analyzing the BRDF of sand and measurement systems that have been used for taking BRDF measurements in the field and the lab. Chapter 3 describes the methods that were used during the field campaign to take field measurements and in the laboratory to build the BRDF measurement system and take measurements in the laboratory. Chapter 4 presents the results describing the nature of BRDF curve, SDSU laboratory measurement repeatability, statistical analysis of the data which were measured in the lab, and a simple BRDF model for perpendicular to the principal plane was modeled. The conclusions drawn after completion of the research and extension for future work are proposed in chapter 5.

CHAPTER 2 LITERATURE REVIEW

2.1 Bidirectional Reflectance Distribution Function(BRDF)

Reflectance is an inherent property of a target that is independent of time, location, illumination intensity, atmospheric conditions, and weather [18]. Previous studies have shown that the Earth's surface is non-Lambertian and reflects differing amounts of energy in different directions. Most of the Earth's surfaces generate spectral reflectance signatures that are anisotropic with respect to view and illumination zenith angles [19]. Thus, any surface on earth has a different reflectance value when observed from a different orientation. When reflectance is measured from all possible angles, a bidirectional reflectance distribution function (BRDF) is created [18]. Bidirectional means that both the incoming light and the observed light are directional and are measured in infinitesimally small solid angles [5]. By definition, BRDF relates the incident irradiance from one given direction to its contribution to the reflected radiance in another direction [20] according to equation 2.1:

$$f_{DD}(\theta_i\phi_i;\theta_r\phi_r) = \frac{dL_r(\theta_i,\phi_i;\theta_r,\phi_r)}{dE_i(\theta_i\phi_i)} \tag{2.1}$$

where f_{DD} is the BRDF, L is the radiance, E is the irradiance, i and r denote the incident and the reflected light, and θ and ϕ mark the zenith and the azimuth angles, respectively. The units of BRDF are [1⁄Sr]. The BRDF describes the angular behavior by which light interacts with surfaces [5] and represents all possible illuminations and viewing geometries. The BRDF is an important factor to be taken under consideration while

characterizing the Earth's surface from remotely sensed data. Satellites measure different reflectance value of any surface on the Earth when it is looking at the surface from different view angles; this phenomena is termed BRDF effect. Since remotely sensed data has numerous applications, it is very important to understand the BRDF effect and how to remove it from an image. Figure 2.1 shows how reflectance changes as both solar and viewing geometry change.

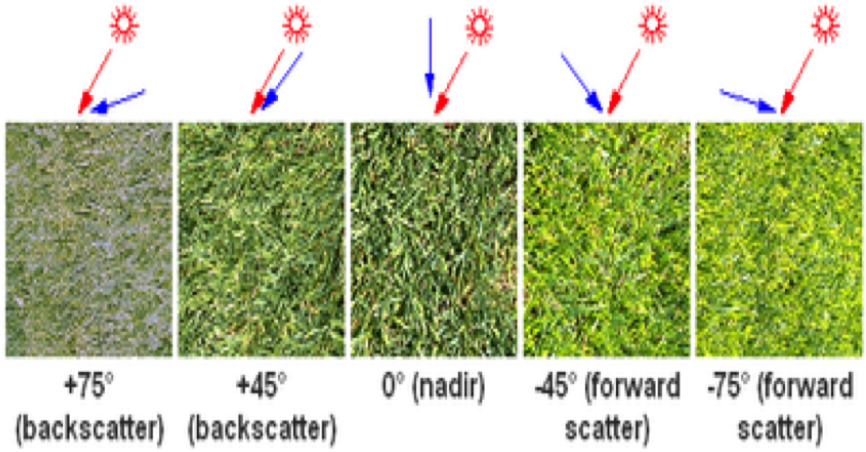

Figure 2.1. Forward and backward scattering [Ref: David Roy, GSE/GEOG-741-S01, lecture-8].

Figure 2.1 clearly shows the change in reflectance dependent upon the position of the sun and the viewing angle used. When the sun and sensor positions are in opposing directions, the effect is called forward scattering. Conversely, when the sun and sensor positions are in the same direction, the effect is called backward scattering and is clearly shown in Figure 2.2.

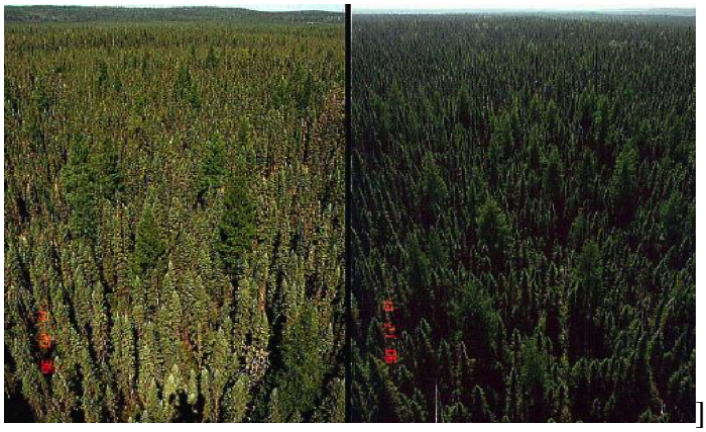]

Figure 2.2. Forward scattering (right) and backward scattering (left).

Figure 2.3 shows a hot spot where the sensor and the sun are in the same direction and as a result a portion of the image is significantly brighter than the rest.

Figure 2.3. Hot spot.

2.2 How BRDF Measurements are Done

In theory, the BRDF is a deterministic quantity of a surface that can be estimated by measuring the wavelength-dependent ratio of radiance to irradiance from a hemispherical perspective [18]. Goniometers are the basic devices used to measure directional reflection properties of surfaces. These instruments can be used in the field as well as in a laboratory

setting. To provide data sufficient for developing a BRDF model, a sensor should be capable of acquiring reflectance values throughout the full range of hemispherical positions over a target. Using a goniometer, the sensor can be directed to sample various view zenith and azimuth angles.

When a goniometer is used in the field, generally it has two main components: one is the sensor and another is the structure to adjust the sensor at various angles. The two main goniometer designs which are suitable for different applications are :

- "a sensor that rotates its view around a fixed center point, thus viewing outwards from the center of the sphere and acquiring sensor data from a different target field of view for each measurement", and
- "a movable sensor from which the same target area is viewed but from a different angle and azimuth for each measurement using a sensor that is moved throughout the hemisphere at a fixed distance from the target[18] ".

The first goniometer system was named PARABOLA which made the fundamental assumption of homogeneity over the area encompassed by different target FOVs. As a result of this assumption, PARABOLA was prevented from being used over many common surfaces that characteristically possess heterogeneity [18]. To cope with this problem, most goniometers were made to view a constant target and only vary zenith and azimuth angles.

The University of Lethbridge presented their goniometer system as a low-cost, flexible, and capable alternative for estimating BRDF in a variety of field and laboratory situations [18]. It has a base ring and a rotatable arch for positioning the

spectroradiometer sensor above the target. The current configuration has an Analytical Spectral Device (ASD) as a spectroradiometer [22], which provides hyperspectral data over the range of 350-2500 nm. This instrument has a spectral resolution of 3 nm between 350 and 1000 nm, a resolution of 10 nm between 1000 and 2500 nm, and has a high acquisition rate of 10 spectra per second.

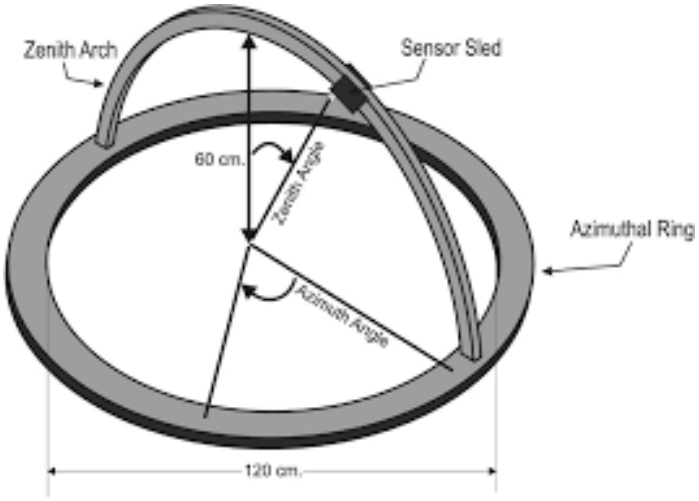

Figure 2.4. ULGS goniometer system layout and dimensions [18]

The University of Lethbridge Goniometer System ULGS was designed to be portable and flexible for both laboratory and field measurements. The zenith arch rides in a track on the azimuth ring and can change position to preassigned azimuth angles. Similarly, the sensor is located at certain zenith angles and can change position to preassigned zenith angles.

The radius of the zenith arch and azimuth ring is 60 cm. This dimension makes the goniometer compatible for both laboratory and field measurements. To make it flexible, legs can be attached to the base of goniometer in order to take measurements of sloped surfaces or plant canopies. The zenith arch is designed in such a way that it casts very

little or no shadow on the target area except along the principal plane. The ULGS system is also capable of taking measurements at any angular precision. Due to the sensor sled that accommodates the ASD pistol grip attachment, the sensor sled and zenith arch can capture measurements from only -60° to +60°. If an angular resolution of 10° is used, there will be 18 azimuth angles,each having 13 zenith angles, for a total of 234 measurements, each at a unique geometry.

2.3 Wavelength Dependence of the BRDF of Beach Sands

A researcher conducted a study to determine whether there is meaningful variance in the BRDF as a function of wavelength for beach sands, and to identify whether a subset of wavelengths is sufficient to characterize the dominant directional reflection for beach sands [5]. To determine the anisotropy factor, wavelength plot in a planar view of the BRDF and principal component analysis (PCA) of the BRDF was performed. Principal Component Analysis is used in multispecrtal and hyperspectral remotely sensed data in order to reduce the dimension of the data. It transforms an original correlated dataset into a smaller data set of uncorrelated variables such that it preserves most of the information of the original dataset [23].

The BRDF of the surface can be derived by measuring the radiance and then calculating the bidirectional reflectance factor (BRF) . The BRF is the ratio of the radiance reflected into a particular direction to the radiance that would be reflected into the same direction by a perfect Lambertian radiator illuminated in an identical fashion [1]. A perfect Lambertian radiator is defined to have a total reflectivity of unity, and because it is Lambertian, it is define to have the same radiance in all directions [1]. The Anisotropy

factor (ANIF) is a value used for examining the BRDF wavelength dependency. It is defined as the ratio of the BRF at a specific view direction to the nadir BRF. The ANIF provides a means to distinguish the spectral BRDF effects from the spectral signature of the sample and it is used to analyze the spectral variability of nadir reflectance with changes in the viewing geometry [5]. Principal Component Analysis (PCA), on the other hand, is an efficient way to analyze wavelength dependency. PCA is used to reduce the dimensionality of data by extracting the linearly independent, most informative subsample of a dataset to produce uncorrelated output bands and to segregate noise components [5]. In this case, PCA was used to analyze the wavelength dependency of the dominant directional reflective properties of beach sand. PCA can be performed using covariance or in its standardized version, the correlation matrix, which gives the same distribution result with a different scale factor. A correlation matrix is a two-dimensional diagonal matrix giving correlation between all pairs of wavelengths. The elements of the correlation matrix are calculated from covariance matrix elements as follows:

$$c_{ij} = \frac{v_{ij}}{\sqrt{v_{ii}}\sqrt{v_{jj}}} \tag{2.2}$$

where c_{ij} represents the elements of the correlation matrix, v_{ij} represents the i_{th} and j_{th} elements of the covariance matrix, and v_{ii} and v_{jj} represents the variances of the ith and jth wavelengths of the dataset [5]. The resulting correlation matrix was used to identify the correlation between each pair of wavelengths and to identity clusters of correlated wavelengths.

For wavelength-dependent analysis, sand from three beaches from eastern

Queensland, Australia were used: Freshwater Beach, Port Clinton Pocket Beach, and Sabina Point Beach. Measurements of beach sand radiance at locations with various sand properties were taken with the Goniometer for Outdoor Portable Hyperspectral Earth Reflectance (GOPHER) [5]. A dual spectrometer approach [25] was used to reduce the effects of varying light conditions while taking the measurements. The anisotropy factor and wavelength plots show that the BRDF of beach sand has minimal wavelength dependence. PCA performed on beach sand BRDF data showed a high correlation between the wavelengths at all sample stations. The correlation matrix from the PCA helps to visualize the wavelength dependence of the BRDF. Only a single wavelength is needed to represent the directional dependence of a visually smooth sand surface while three wavelengths (from the appropriate clusters) are needed to represent the directional dependence of the entire wavelength range for a visually rough beach sand surface.

The weak wavelength dependence of the BRDFs of beach sand can be captured with three broad wavelength regions instead of hundreds of individual wavelengths. The spectral range of the groups varies slightly from case to case, however, all are represented by three clear wavelength ranges: 350-450 nm, 700-1350 nm, and 1450-2400 nm. These ranges exclude the atmospheric water vapor absorptions bands.

2.4 Linear Mixed Model

General underlying linear models are present in most of the statistical analysis that is used in applied research [26]. Regression analysis is a statistical tool for investigation of relationships between variables. The purpose of a regression analysis is to observe sample measurements on different variables, called dependent variables, and to examine

the relationship between dependent variables. This relationship is expressed as a statistical model called a regression or linear model [27]. A simple linear regression model is expressed as

$$y = \alpha + \beta x + \varepsilon \tag{2.3}$$

where x and y represent independent and dependent variables respectively. This model is referred as the regression of y on x, and α and β are known as regression coefficients. β is the slope of the regression line, which represents a corresponding change in y per unit change in x, while α represents the intercept, or value when $x = 0$. Finally, ε represents the unexplained variance of independent variables. In equation 2.3, x is known as a fixed effect whereas ε is an error term which represents deviations from the prediction due to random factors which cannot be controlled. With linear models, the world is divided into two things: that which can be understood or is somehow systematic (fixed effect), and things that cannot be understood or controlled [28]. The non-systematic part of the linear model doesn't have any interesting structure; in a linear mixed model, random effects are added along with fixed effects, to give structure to the error term "ε". The mixture of random and fixed effects is what creates a mixed model [28]. Introducing random effects to a linear mixed model doesn't mean that error terms will not show up in a linear mixed model. Even if random terms were introduced to address error, there will still be an error term in the linear mixed model.

The Linear Mixed Model is a vital model for many case studies. Researchers have been using this type of model frequently as it is a very flexible and powerful tool for understanding the world. In one case study, researchers tried to see the relationship

between pitch of voice and politeness of an individual [28]. Voice pitch of an individual is affected by various factors like politeness and gender, which are fixed effects. When multiple responses from an individual were studied, differences in voice pitch for the same individual were observed. Ideally, the pitch of the voice remains the same, but in reality there are variations. This problem cannot be addressed using a fixed term; the only way to address these differences is to introduce a random term in the model to attempt to capture the random phenomena in the experiment.

The optics laboratory experiment for studying the spectral responses of sand samples is analogous to the study of pitch of voice described above. As in the aforementioned case, measurement of the spectral response of a sand sample also has fixed and random effects. Since there is a significant change in the spectral response of the sand when the view angle is changed, view angle has a fixed effect on spectral response. Furthermore, using the same sand and same laboratory conditions, there are slight differences in the spectral response of the sand between runs which is not systematic in nature and thus should be considered as a random effect. In the laboratory measurements, the sand itself is also considered as a random factor because despite being from the same desert, different samples possess slightly different spectral responses, an effect which is random in nature.

CHAPTER 3 METHODOLOGY

3.1 Selection of Site

An algorithm was developed by the SDSU Image Processing laboratory to identify extremely stable sites on the Earth's surface along their temporal variability [17]. Among them, the Sonoran Desert (WRS-2 Path 38 and Row 38) and the Algodones Dunes (WRS-2 Path 38 and Row 37), located at American-Mexican border, were selected as invariant sites. Although Libya 4 was found to be more stable than these two PICS, all Landsat satellites don't have an adequate number of acquisitions which prevent it for being used extensively for calibration work [17]. Since the Algodones Dunes is frequently imaged by earlier satellites, and the fact that this site is easily accessible, made it one of the favorite sites for calibration work.

3.2 Algodones Dunes Field Campaign Equipment

A field campaign was performed from 8^{th} to the 13^{th} March, 2015 at the Algodones Dunes to gain a better understanding of the surface reflectance of sand at the site. The field campaign to the Algodones Dunes involved the use of an ASD spectrometer and white reference panel along with a computer to store spectral data collected. The white reference panel was used to collect reference spectra which are used to calculate reflectance of the sand as observed in the field. The ideal method of measuring this reference is to measure the downwelling radiance looking up toward the sun, but to simplify the measurement a 99% reflective white panel is used to reflect solar irradiance upward. Knowing the absolute specular reflectance of the panel (BRDF characterized) the

exact downwelling solar radiance can then be calculated.

In Figure 3.1, a researcher was acquiring spectral measurements of sand at the Algodones Dunes.

Figure 3.1. Taking measurement in the Algodones Dunes.

Generally, he kneeled with the back end of the pole planted in the sand and with the optics positioned approximately 0.7 m above the sand. The entire assembly was then rotated while looking at the same spot in the sand. The area sampled thus consisted of a circular area approximately 10 cm in diameter becoming oval shaped as the apparatus rotates. The viewing angle was automatically recorded using an inclinometer attached to the optical assembly.

In Figure 3.2, researchers were measuring the white reference panel.

Figure 3.2. Taking measurement of white reference panel.

The optics were held around 0.3 m above the reference panel. While placing the white reference panel, the orientation of the panel towards the sun was maintained. More importantly, the panel was kept level.

The white reference panel was not a perfect reflector. As shown in Figure 3.3 reflectance changes depending upon view zenith and wavelength.

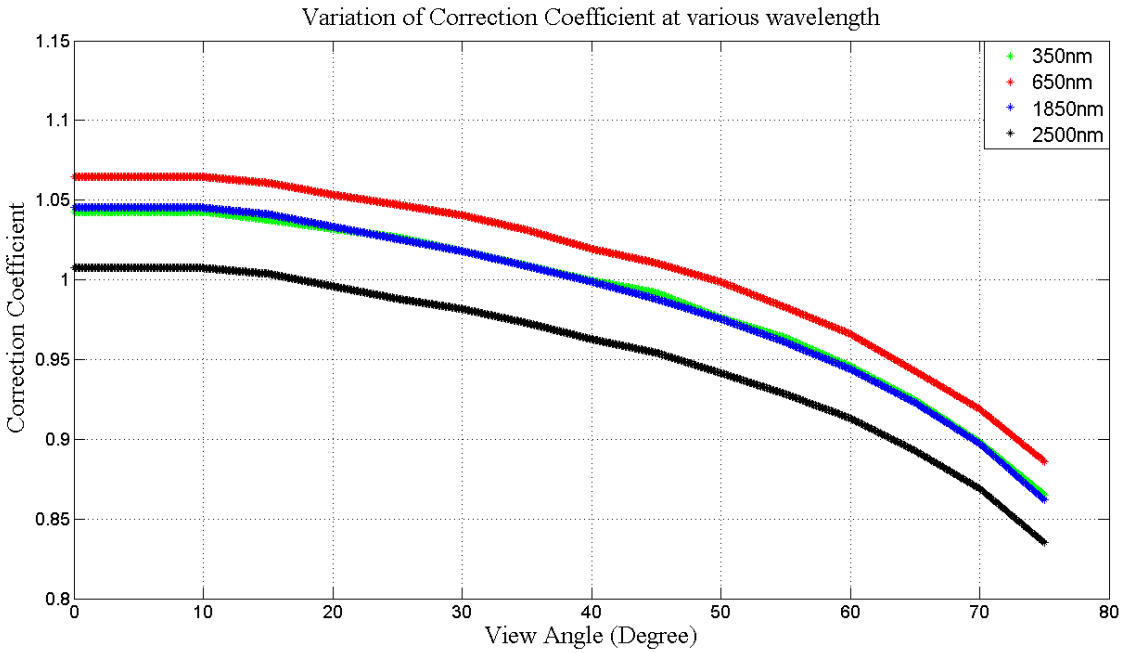

Figure 3.3. Variation of correction coefficient at various wavelength of white panel.

The reason the panel shows these differences is due to the characteristics of the material from which it is made. Therefore, before processing the spectrum from the white panel, it was divided by a correction coefficient in order to account for the spectrum of the white panel, to accurately compute downwelling radiance.

The calibration file consists of correction coefficients for specific view angles (ranging from nadir to 75°) and wavelengths (ranging from 350 nm to 2500 nm). This calibration correction was derived by comparing the output to a known National Institute of Standards and Technology(NIST) traceable standard. Due to the limited wavelength and angular measurements acquired during the panel calibration process, the reflectance coefficients need to be linearly interpolated to determine correction coefficients at each nm of wavelength and each degree of view angle, corresponding to the hyperspectral measurements of the ASD.

Figure 3.4 shows the normalized correction coefficients for four wavelengths: 350 nm, 650 nm, 1850 nm and 2500 nm.

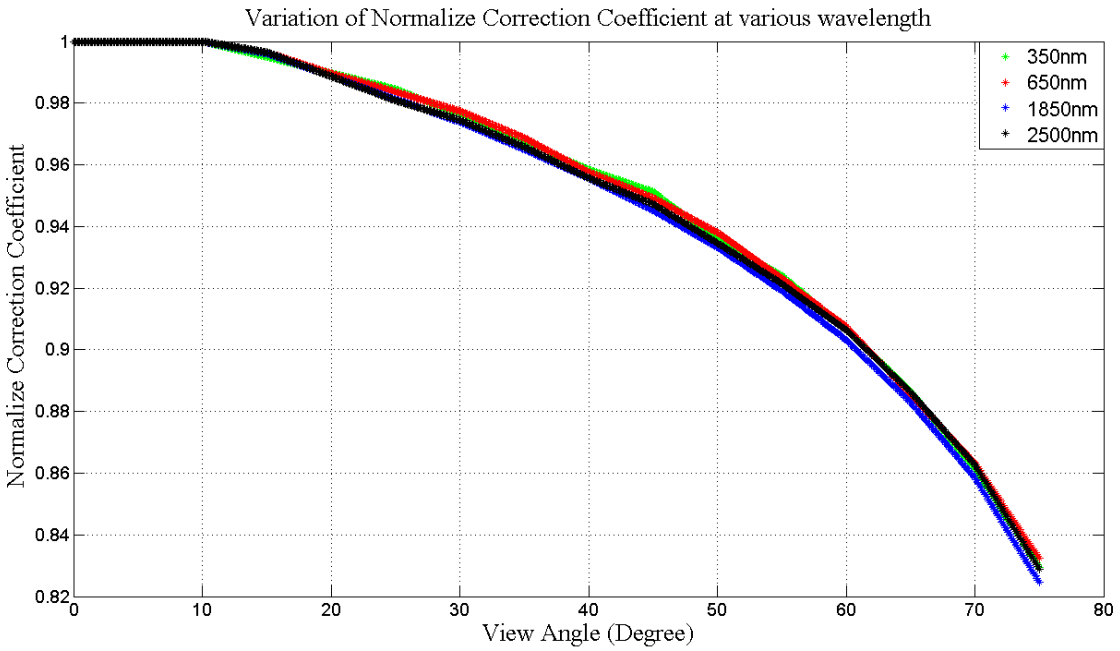

Figure 3.4. Variation of normalize correction coefficient at various wavelength of white panel.

These correction coefficients were normalized using the correction coefficient at nadir. The trend for the decrease in the correction coefficients with an increase in view angle is the same for all wavelengths, as is clearly shown in the Figure3.4.

3.3 Algodones Dunes Field Campaign Test Setup

While at the Algodones Dunes, the spectrum of sand from different locations was measured. These locations in the Algodones Dunes were confined by a rectangle whose latitude and region of interest are summarized in Table 3.1 below:

sfssf

Table 3.1. Latitude and longitude of rectangle within which sand samples were taken.

Corner	Latitude	Longitude
Upper Left	32°55’12.74”	115°7’2.37”
Upper Right	32°55’12.74”	115°6’32.43”
Lower Left	32°54’56.62”	115°7’2.37”
Lower Right	32°54’56.62”	115°6’32.42”

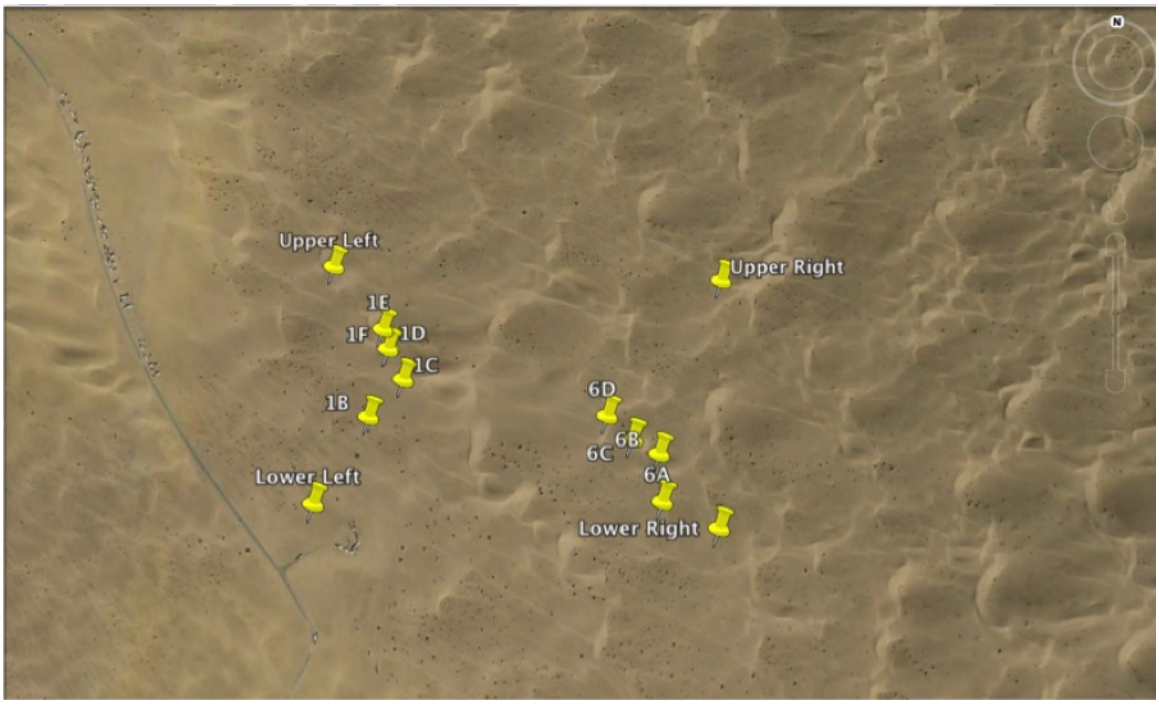

Figure 3.5. Location of sand samples in the Algodones Dunes.

Figure 3.5 shows locations where the sand spectrum was observed using the ASD. Labels 1A, 1B, 1C, 1D, 1E, and 1F were locations whose spectra were collected on 10 March, 2015 while the locations labeled as 6A, 6B, 6C and 6D were collected on 12 March, 2015. Altogether, measurements were done in the field at ten different locations and sand samples from those locations were brought to the lab for further analysis. Sand samples were taken from the bottom of the dunes, middle of the dunes and top of the dunes, so the reflective properties of sand samples from spatially different locations on a dune could be analyzed to determine if intrinsic differences do or do not occur. Sand

samples were also taken from different dunes for analysis of whether differences in spectra were present from one dune to another.

3.4 Algodones Dunes Field Campaign Data Processing

At each test point, two sets of measurements were taken. The first measurement was taken perpendicular to the principal plane while the second set of measurements was taken in the principal plane. A principal plane is a plane which is parallel to the rays of light (in this case rays of light from the sun). Perpendicular to the principal plane describes the plane which is perpendicular to the rays of light coming from the Sun. For each measurement, the ASD was optimized, then white panel measurements were taken by looking down at the panel at a nadir orientation. The spectrometer was set to 10-spectra/saved files so the instrument took 10 spectra, averaged them and then a file was stored. The file system starts with file 000 and then auto advances to 001, then 002 and so on. Three files were saved for each measurement. This means that it automatically ran through the first 10 spectra, averaged them, and saved the average as file 000. The process was automatically repeated, with the next file saved as 001, and a final set was done and saved as 002.

The first set of three files would be used as the reference, which gives the radiance of sun. Next, the radiance of the surface was measured and reflectance was later calculated by dividing by the absolute radiance of the surface by the radiance of the sun, thus giving a measured reflectance of the sand. Sand radiance measurements were made by placing the back end of the pole on ground and optics about 0.7 m above the sand as illustrated in Figure 3.1. An inclinometer, a device to measure the inclination, would run

free for about 2 minutes to warm up. Holding optics at nadir, the spectrometer was started by hitting the space bar and the first three sand spectra (003 through 005) were acquired. The optics were then rotated 5° clockwise, i.e. -5° (following physics sign convention where rotating clockwise is taken as negative), then the next set of spectra was acquired. This was repeated up to approximately -45°, then back to nadir. During that time interval, the inclinometer had been running automatically and took 10 sets of angle measurements. The above process was then repeated with measurements taken in the clockwise direction from nadir to +45°. At the end, reference panel measurements were taken again. After taking a measurement perpendicular to the principal plane, the position was rotated and the full process was repeated in the principal plane. Assuming Sun is at the south, rotating sensor head to west looking at east is considered as a clockwise direction and vice-versa as an anticlockwise direction in perpendicular to a principal plane. Assuming the Sun is at the south, rotating sensor head to the north looking at the south is considered as the clockwise direction in a principal plane.

In Figure 3.6, the yellow solid circle represents the sun at the time of data acquisition. Blue symbols represent measurements taken in the principal plane whereas black symbols represent measurements taken perpendicular to the principal plane. The measurement was taken in the principal plane up to +/-50° view zenith angle. Similarly, measurements were taken perpendicular to the principal plane.

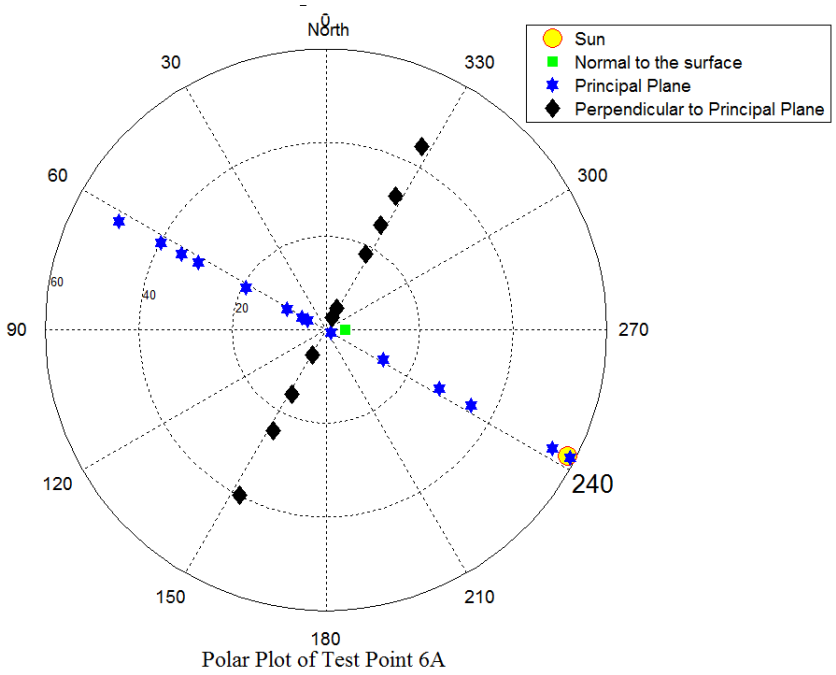

Figure 3.6. Pattern of data acquisition in test point.

3.5 Lab Setup for simulating Environment of Algodones Dunes

All laboratory measurements were carried out in a darkroom where the walls of the dark room were painted with black latex to avoid stray light effects. The equipment setup was also covered with black cloth to avoid unwanted reflection and scattering while collecting data.

Figure 3.7 shows the light source in a laboratory illuminating the target, a sand sample brought from the Algodones Dunes.

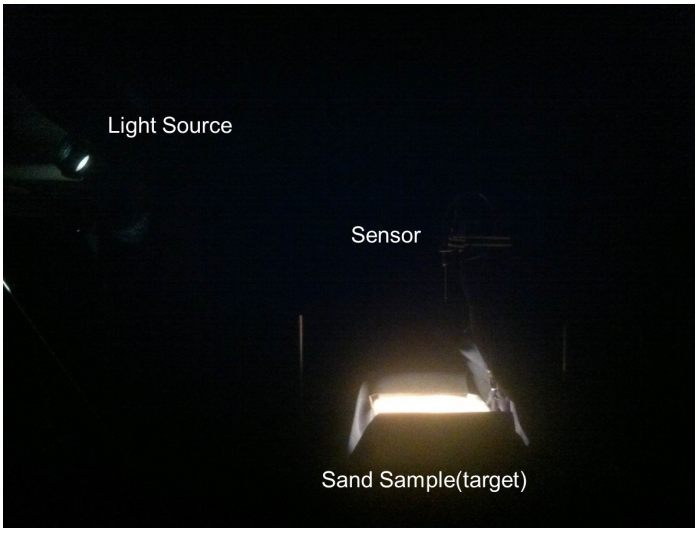

Figure 3.7. Light source illuminating sand target.

A halogen bulb was used as the main light source simulating the sun in the field. The angle between the light source and the sand target was maintained at approximately 45° which is within the range of solar zenith angle at the Algodones Dunes over a year.

Figure 3.8 and Figure 3.9 shows that the optics were positioned to observe the target at nadir view. The mechanical arm held the optics at a distance of 12 inches from the target.

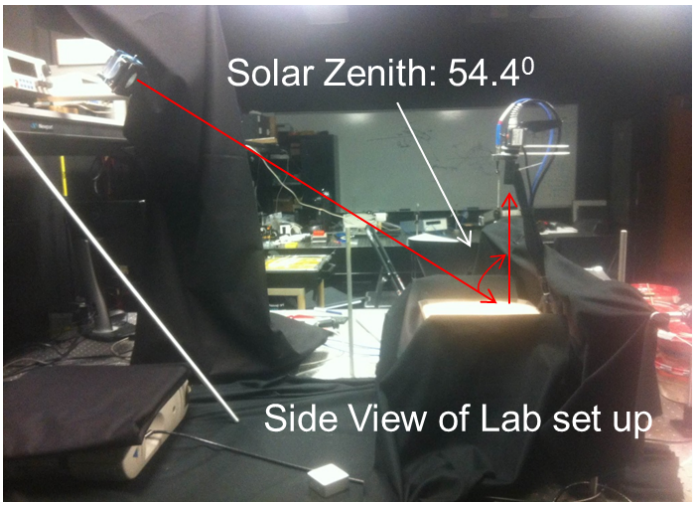

Figure 3.8. Light source illuminating target and optics collecting the numbers of photons reflected from target.

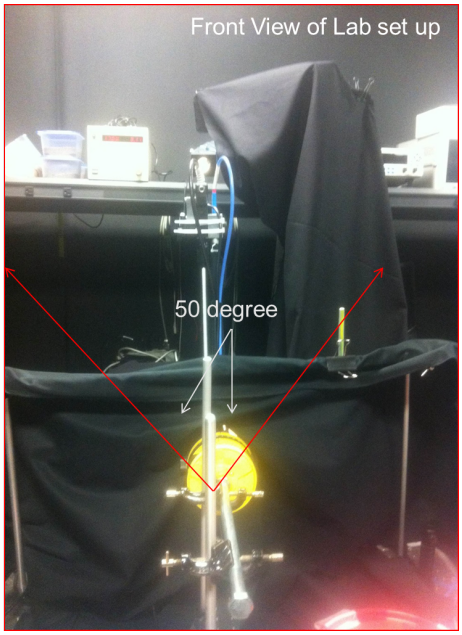

Figure 3.9. Mechanical arm holding optics looking at target.

The instantaneous field of view of the optics was set to be 5°. The first reason to choose the 5° field of view is that the spectrometer was calibrated for 5° so calibration coefficients are available for 5° and the second reason was the sample size was small and 5° of field of view guarantees that the sensor will see target at different field of view. The optics collected the light reflected by a small portion of the sand, which was kept in a tray and held by a stand to maintain a fixed distance between the optics and the target. In Figure 3.9, the optics was set to nadir view, but measurements at different view zenith angles were taken up to 50° due to limitations of the setup.

In Figure 3.10, point A represents the position of optics that collects the light, point B represents the target and length BC represent the radius of the circle at which the sensor is looking.

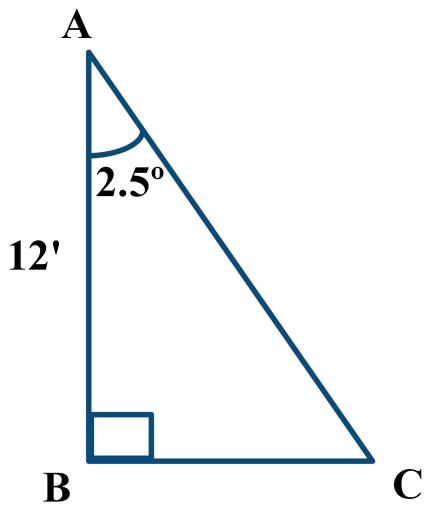

Figure 3.10. Right angled triangle ABC.

The area of a circle with radius BC gives the portion of the target which is observed by the optical sensor. The area of sand which is being observed is 5.47 cm^2.

3.5.1 Mechanical Arm

Spectra of the sand from various view angles was required for the analysis. The view zenith angles were confined between +25° to -25°. While the optics was moved from +25° to -25° and a mechanical arm was used to lock the optics at different angles. The mechanical arm enabled acquisition of a number of measurements at different view angles in the principal plane and perpendicular to the principal plane.

3.5.2 Illumination

A 150 Watt lamp was used as an artificial light source with a focused output beam. The lamp, an OSL2BIR from Thorlab, was used as it provides enhanced output in the near-IR due to the aluminum-coated reflector and lack of an integrated hot mirror [29]. Figure 3.11 below shows the emission spectrum of OSL2BIR, which clearly shows the

energy emitted in the infrared region. The halogen bulb used was not uniformly illuminated so slight shadows were projected along with the beam. The shadow might add some uncertainty since measurements are very sensitive to the brightness of the target when looking from different angles. The available solution was to adjust the bulb in such a way that the slight shadow was evenly distributed on both sides of the target.

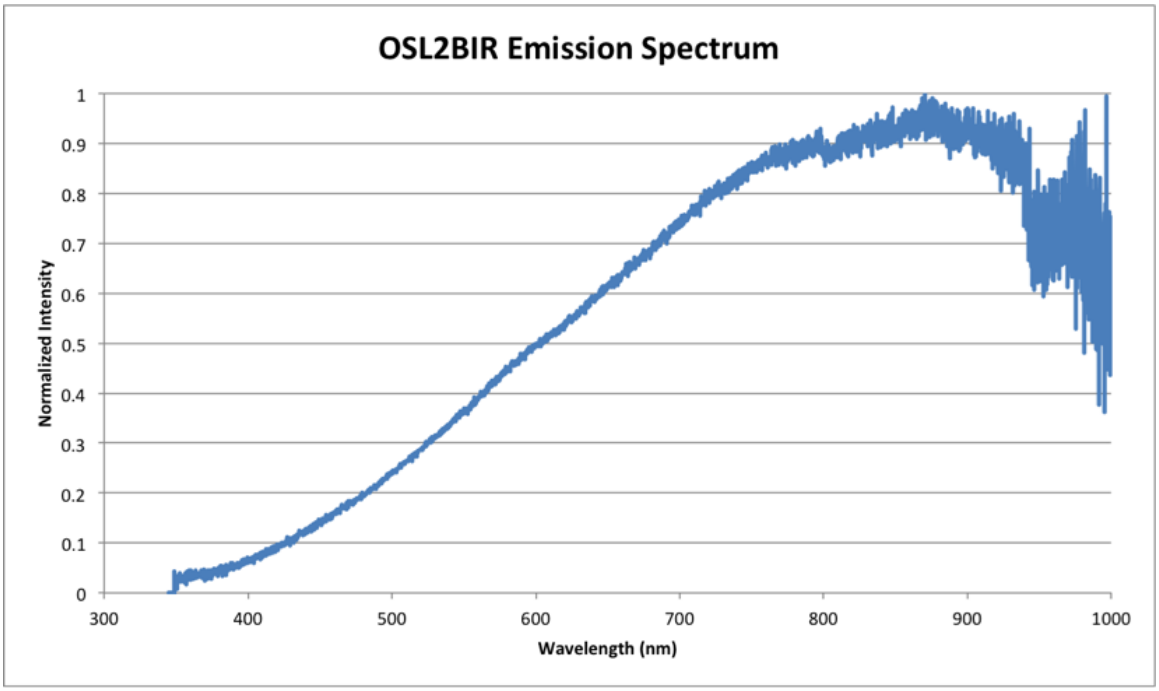

Figure 3.11. OSL2BIR emission spectrum

3.5.3 Sensors

Measurements of spectral radiance in the lab and field were obtained with an ASD Fieldspec 3 spectroradiometer. This measured the spectral radiance from 350 nm to 2500 nm, where the sampling interval for the FieldSpecFR is 1.4 nm for the range of 350-1000 nm and 2 nm for the range of 1000-2500 nm. The FieldSpec FR spectroradiometer uses a 1.5 meter long fiber optic input that feeds directly into the spectrometer. There are two advantages of this arrangement: “First, the fiber optic input allows the user to quickly

move and aim the very lightweight fiber optic probe from point to point without having to move the entire spectrometer. Secondly, since the fiber optic is connected directly into the spectroradiometer there are none of the signal losses otherwise associated with detachable couplings, which typically result in as high as 50% signal loss [22] ". The FieldSpec can record a complete 350-2500 nm spectrum in 0.1 seconds. This speed allowed for data collection in a short amount of time.

3.5.4 Software

The laboratory setup was controlled by a "Control PC" with custom-built software. ViewSpecPro software was used to view the spectral radiance measured by the ASD. A regular desktop or laptop could be used as the controller as long as requirements for connection options were met.

3.5.5 Lab Procedure

Electronic instruments such as the halogen bulb, digital power supply, and mechanical arm were used to simulate the field environment in a laboratory. To get rid of the transient response of the instruments the system was always stabilized by warming up for approximately 20 minutes before measurements were made. A halogen bulb was used as the light source in the laboratory. Even though the halogen bulb was capable of illuminating the target with more power, it was limited to only 102 Watts (current = 6 Amps and voltage = 17 Volts) due to a trade-off between the illuminating power of the bulb and the capacity of the cooling mechanism used for the system. Measurements were taken for solar zenith angles of 54.4° and 45° which were within the typical range of solar zenith angles at the Algodones Dunes over a year.

Generating a simple BRDF model requires measuring the reflectance of the sand sample from multiple view angles. Thus, the spectrum of the sand sample at different view angles was acquired by rotating the optical sensor in a clockwise direction starting from nadir up to 50° with an increment of 5° each time. After acquisition in the clockwise direction, the same process was repeated in the anticlockwise direction, similar to the measurement process in the field.

After setting up the lab, first three spectra of the gray reflectance panel were taken at nadir view. Then measurements of the sand at view angles from +50° to -50° were made. In order to track the repeatability of measurements, measurement of the gray panel at nadir view was repeated after completing the data acquisition in both clockwise and anticlockwise directions.

All the raw files were selected to process. Radiometric calculation option inside process menu was used to generate radiometrically corrected file asd.rad from a .asd file.

In order to eliminate drift that appeared in the intersection of the two spectrometers within the ASD, a parabolic correction was applied. Parabolic correction is the factory recommended correction for loss of sensitivity at a suboptimal wavelength. Due to the difference in sensor response at different wavelengths, the whole spectral range is divided into three region: 350 nm to 675 nm, 676 nm to 1400 nm and 1401 nm to 2150 nm. The different sensor is used in these range of wavelength. At the transition wavelength from one range to another range, slight drift was observed, meaning the curve wasn't smooth, which might contribute to slight variation in reflectance value. After applying parabolic correction, the corrected files were generated for further processing.

In Figure 3.12, two curves are exactly overlapped with each other except for

approximately 400 nm to 600 nm and from 1400 nm to 1450 nm.

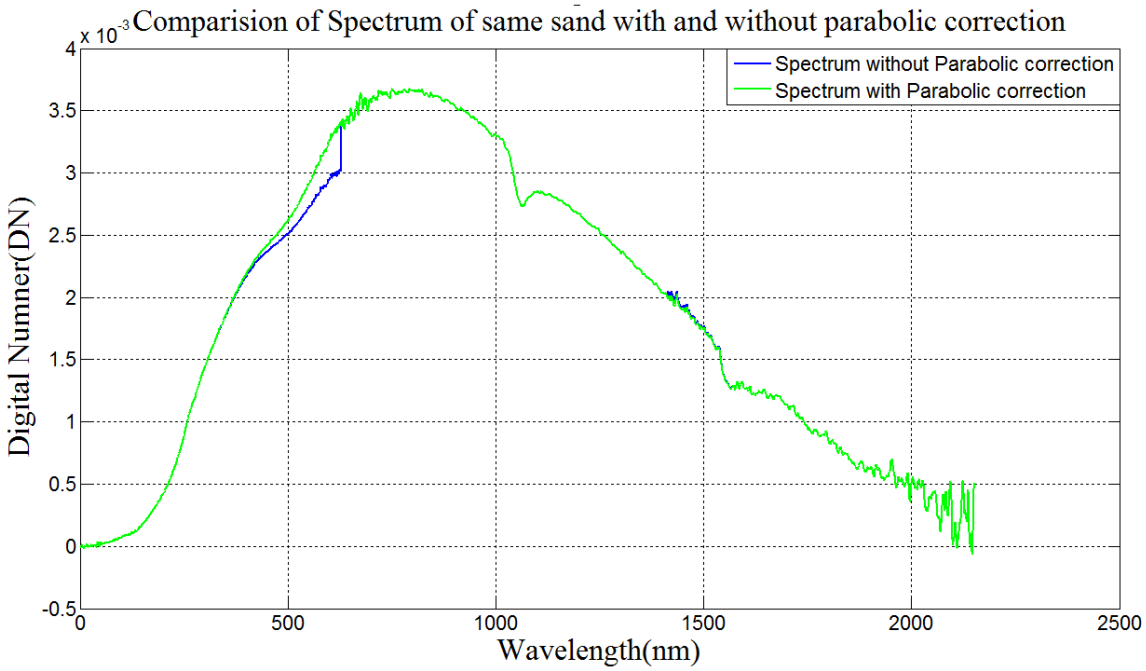

Figure 3.12. Comparison between spectrum with and without parabolic correction.

The blue curve represents the spectrum of the sand before applying a parabolic correction and the green spectrum represents the spectrum of sand after applying a parabolic correction.

A second calibration standard (nominal 80% reflective) is termed as “the gray panel”. The gray panel, which was used as a reference, is also somewhat nonlambertian. The reflectance of the gray panel is dependent on both view zenith and wavelength so the standard calibration file was used to correct the angular and wavelength dependency of the gray reference panel. As shown in Figure 3.13, the correction coefficient changes according to view angle and wavelength.

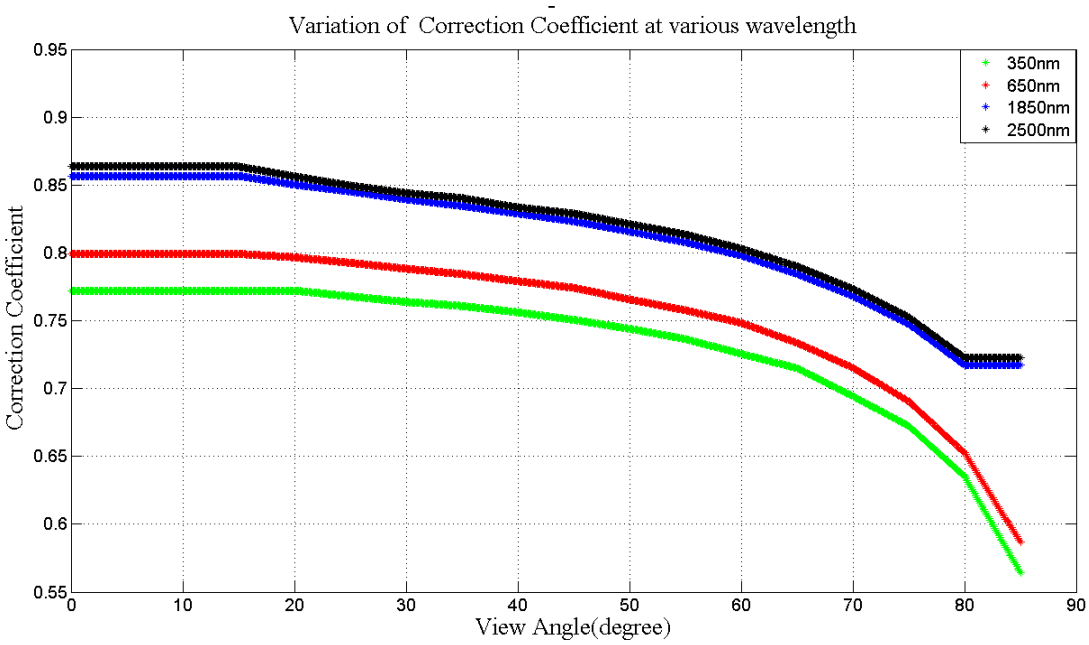

Figure 3.13. Variation of correction coefficient at various wavelength of gray panel.

At nadir, the gray panel is approximately 77% reflective at 350 nm but is approximately 86% reflective at 2500 nm. This is due to the characteristics of the material from which the gray panel is made up. As view angle increases, the correction coefficient decreases which indicates that the gray panel is also less reflective at larger view zenith angles. So before using the gray panel, the correction coefficients for corresponding solar zenith angles are applied.

The gray panel calibration file, which has correction coefficients at certain wavelengths and angles, was interpolated using linear interpolation to get correction coefficients at the desired ranges of wavelength and view angle. The correction coefficients for the gray panel were normalized at all view angles by the correction coefficient at nadir. In Figure 3.14, it is shown that the normalized correction coefficient varies with respect to view angle.

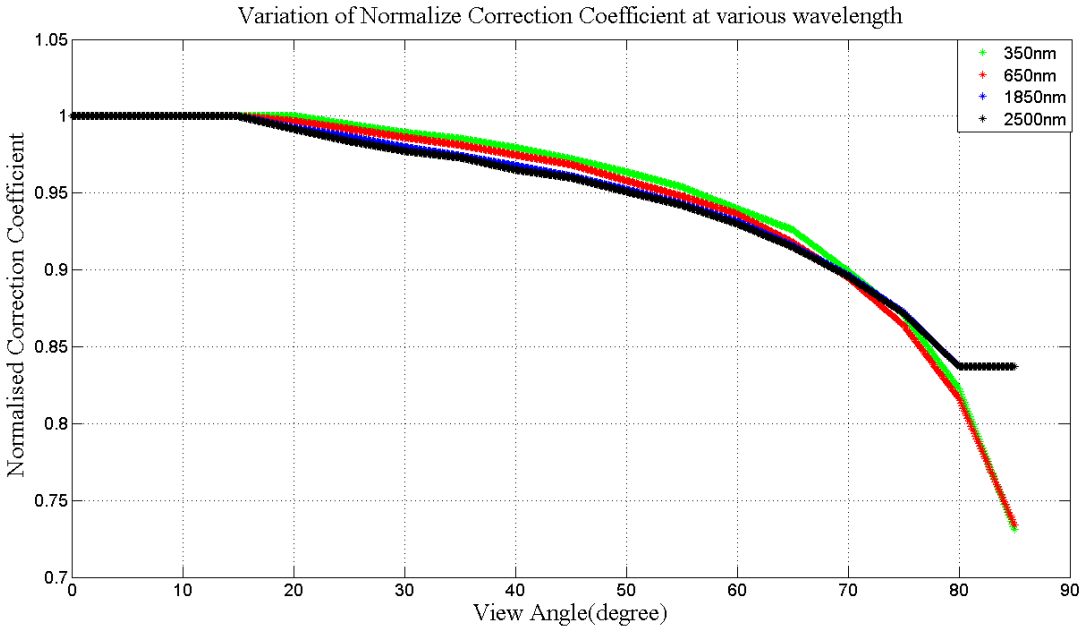

Figure 3.14. Variation of normalize correction coefficient at various wavelength.

3.5.6 Simulation of inclined surface in laboratory

Surfaces at the Algodones Dunes were not flat; the area consists of dunes with varying heights and slopes. Test points chosen for analysis also had different elevations. To simplify analysis of the orientation of test points, the surface normal of these test points was taken into account. Elevation angle and azimuth angle of the surface normal along with unit vectors of the surface normal are included in the Table 3.2:

Table 3.2. Surface normal components and compass measurement for test points from 12 March 2015.

Date	Time	Test Point	Surface Unit Normal (in terms of unit vector)			Using Compass Angle	
			i(east)	**j**(north)	**k**(up)	Elev(Deg)	Azi Ang (Deg)
11 March	16:30	6A	0.070	0.000	0.998	86	90
11 March	16:45	6B	-0.234	-0.251	0.937	69.9	223
11 March	17:03	6C	0.000	-0.105	0.995	84	180
11 March	17:22	6D	-0.363	-0.224	0.900	64.6	238

The vector product was utilized to calculate the angle between nadir and the surface

normal. Angles between nadir and test points 6A, 6B, 6C and 6D are summarized in Table 3.3:

Table 3.3. Angles between nadir and surface normal of test points.

Test Point	Angle Between Nadir and Surface Normal
6A	4.01 °
6B	20.52 °
6C	5.98 °
6D	25.98 °

To correlate field measurements with lab measurements, lab conditions should be the same as at the Algodones Dunes. To simulate the test points of the Algodones Dunes in the lab, the elevation angle of a surface in the field was compensated for by adjusting the view angle since only horizontal surfaces could be implemented in the lab.

In Figure 3.15, the **R** vector represents the surface normal, θ is the angle of elevation of the surface normal, and ϕ represents the azimuth angle of the surface normal.

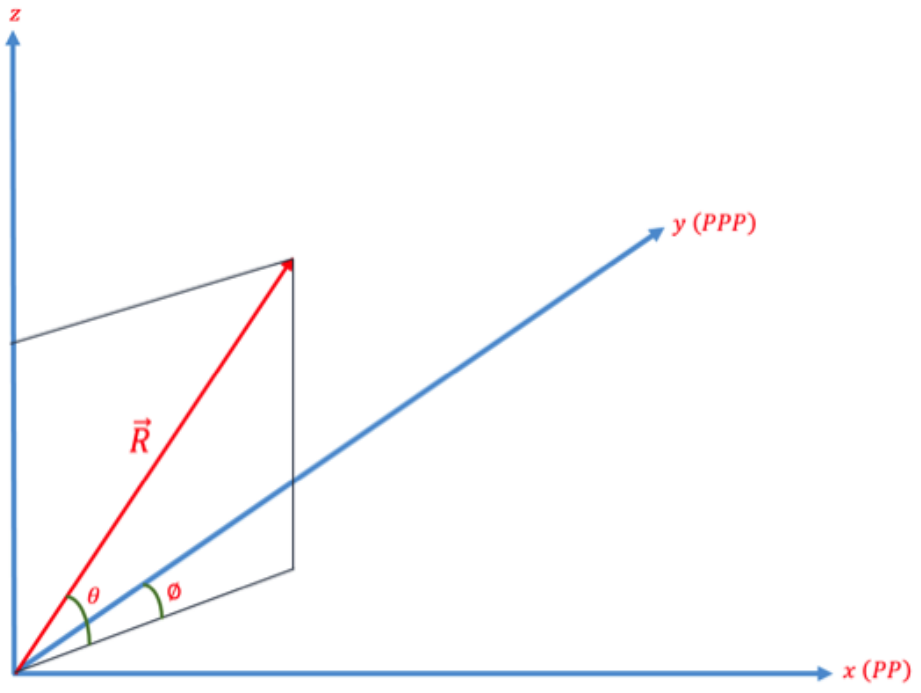

Figure 3.15. Surface normal.

Angles required to simulate an inclined surface in the lab were found by resolving the surface normal vector into the principal plane and the perpendicular to principal plane. Then, the angle between the resolved components, in the principal plane and perpendicular to the principal plane, and nadir was found. Using test point 6A as an example:

Zenith angle of surface normal (θ_{zenith}) = 4.01°

Elevation angle of surface normal($\theta_{elevation}$) = 90° – θ_{zenith} = 90°- 4.01° = 85.99°

The angle between the plane of the surface normal and perpendicular to the principal plane was found by subtracting the azimuth angle of the surface normal from the azimuth of the sun while taking measurements at test point 6A.

The azimuth of the surface normal is 90°, which is mentioned in Table 3.2, and the azimuth of the sun, while the spectrum was measured, is 117.66°. So the angle between the plane of the surface normal and perpendicular to the principal plane is:

ϕ = 117.66° - 90° = 27.66°

Surface normal component in x axis (principal plane):

$R_x = \cos(\theta_{elevation})\sin\phi$

= cos 85.99° sin 62.34° = 0.062

Surface normal component in y axis (perpendicular to principal plane):

$R_y = \cos(\theta_{elevation})\cos(\phi)$ = cos 85.99° sin 62.34° = 0.0325

Surface normal component in z axis (nadir):

$R_z = \sin(\theta_{elevation})$ = sin 85.99° = 0.998

Vector representation of resolved component of surface normal into PP and PPP:

Component in principal plane (x axis):

R_PP = [R_x 0 R_z] = [0.062 0 0.998]

Component on perpendicular to principal plane (y axis):

R_PPP = [0 R_y R_z] = [0 0.0325 0.998]

Component at nadir:

z axis = Nadir = [0 0 R_z] = [0 0 0.998]

The angle between the surface normal component perpendicular to the principal plane and nadir was found by using the following formula:

$$\delta = \cos^{-1} \frac{\vec{R}.\vec{N}}{|\vec{R}||\vec{N}|} \tag{3.1}$$

where $|\vec{R}|=\sqrt{r_x{}^2 + r_y{}^2 + r_z{}^2}$ and $|\vec{N}|=\sqrt{n_x{}^2 + n_y{}^2 + n_z{}^2}$ where vector R represents the surface normal component perpendicular to the principal plane and vector N represents nadir.

$$\delta = \cos^{-1} \frac{[0.06200.0998].[001]}{0.9985 * 1} = \cos^{-1} \frac{0.9980}{0.9985} = 1.87^{\circ}. \tag{3.2}$$

Similarly angle between surface normal component in principal plane and nadir was found using same way:

$$\delta = \cos^{-1} \frac{[00.03250.0998].[001]}{0.9999 * 1} = \cos^{-1} \frac{0.9980}{0.9999} = 3.56^{\circ}. \tag{3.3}$$

While simulating test points in the laboratory, certain angles should be compensated in both the PPP and PP. But due to limitation, in lab apparatus, compensation is only done in the PPP. For example, when lab measurements were performed for test point 6A, 2° south was considered to be nadir to compensate for the slope of the surface of the test

point. Similarly, while simulating other test points in the laboratory, view angle was adjusted in the same way. Angles which should be considered while simulating test points from 12 March, are summarized in Table 3.3.

3.6 Statistical Test

As mentioned previously, sand samples were taken from different locations in the Algodones Dunes. Before developing a BRDF model, it was necessary to determine whether the reflective properties of sand taken from different locations in the Algodones Dunes are the same or not. If the reflective properties of sand samples from various locations are different, then different BRDF models for each location should be developed. But, if the reflective properties of the sand from different locations are the same, then the same BRDF model can be used for any location within the Algodones Dunes.

For lab measurements, the solar zenith was fixed at one specific angle, i.e. 45°, then the reflectances of all sand samples at view zenith angles from +25° to -25° were determined. From the reflectance values at these view zenith angles, a BRDF curve was generated for each sand sample.

While doing statistical analysis for the reflective properties of sand, other factors, which could contribute to differences in the reflectance of the sand needed to be considered. Factors like uncertainty in the light source and uncertainty in the ASD were taken into consideration. In order to estimate the uncertainty of the lab setup, multiple measurements for the same sand were performed in the same environment. Linear mixed effect analysis was performed to test whether the reflective properties of the sand samples were the same or not. While developing the linear mixed model, random and fixed effects

of the model were determined.

3.6.1 Random Effect

A random effect is generally something that can be expected to have a non-systematic, idiosyncratic, unpredictable, or "random" influence on the data set [28]. For this experiment, sand samples and BRDF runs were considered random effects. Since sand samples were taken from random locationswithin the Algodones Dunes, this was considered a random effect. BRDF runs were also considered as random effects because even if everything in the lab was kept constant while taking measurements, the BRDF curve would not be identical for multiple BRDF runs.

3.6.2 Fixed Effect

Fixed effects, on the other hand, are expected to have a systematic and predictable influence on data. In this experiment, the effect of view zenith angle is a fixed effect because it is known that the reflectance of any sand sample will have a higher reflectance as view angles move away from nadir.

After determining the random and fixed effects present in the experiment, a linear mixed model was fitted to the data set. Like any other model, the linear model also relied on assumptions. The residual plot, histogram, and quantile-quantile plot were analyzed to check whether the assumptions made about the linear model, like linearity , or normality of residuals, were violated or not.

While designing the model, initially a random intercept model was used, keeping slopes for all BRDF curves of sand samples and BRDF runs the same.

CHAPTER 4 RESULTS

Results obtained from the field campaign and laboratory measurements using the methods present in Chapter 3 are presented in this chapter.

4.1 Results from the Algodones Dunes

4.1.1 Results from 12 March, 2015

During the field campaign, data was taken for two days, 10 March 2015 and 12 March 2015. Test points were selected from spatially different locations in the Algodones Dunes. At each test point, measurements of view zenith angles were taken in two different planes, PP and PPP. Results from one of the 12 March test points (6A) is presented in Figure 4.1 and 4.2:

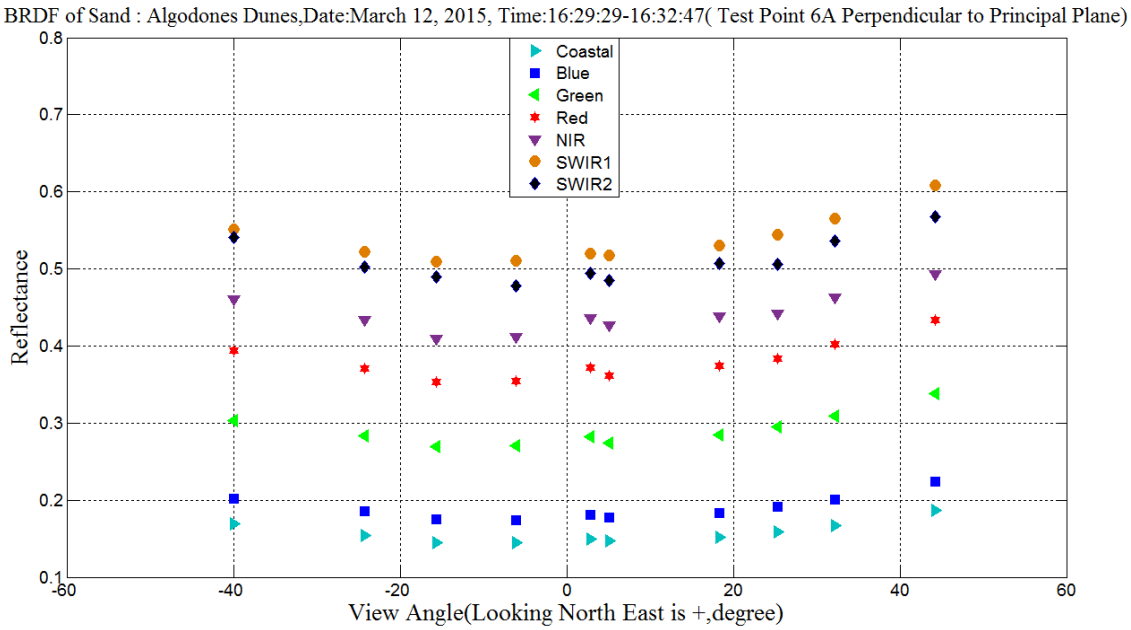

Figure 4.1. 6A perpendicular to principal plane.

4.1.1.1 Absolute Scale

Figure 4.1 shows the reflectance values of test point 6A plotted against view zenith angles perpendicular to the principal plane. As view zenith angles increase from nadir, reflectance of the sand increases.

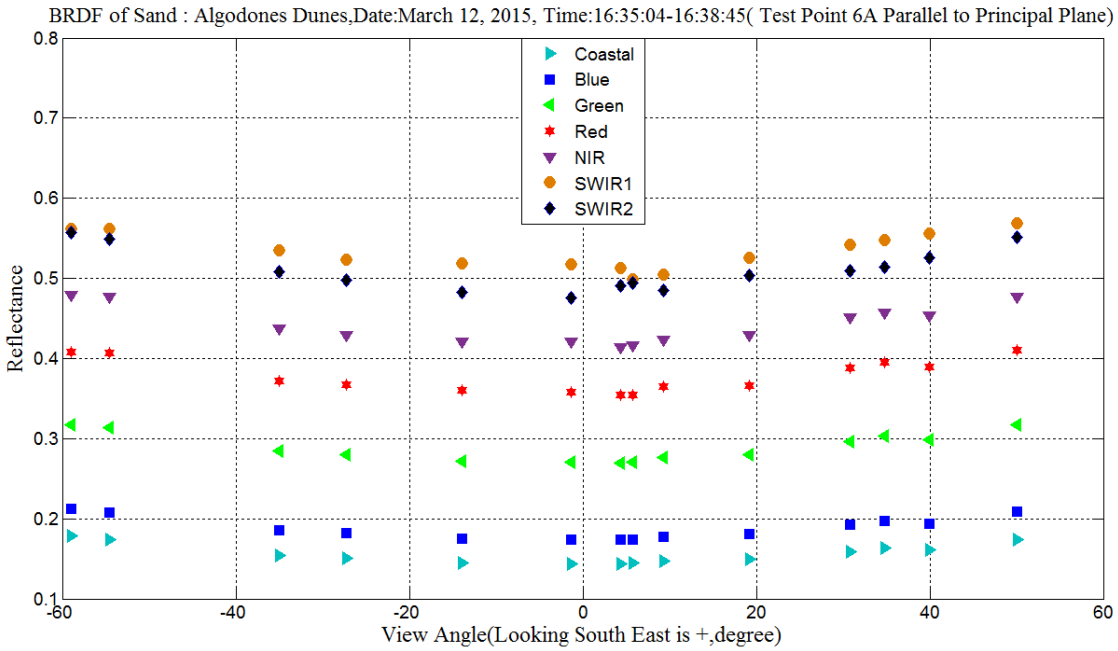

Figure 4.2. 6A principal plane.

Also in the PP, reflectance values increase as view zenith increases. As shown in the figure above, all bands have the same kind of angular dependency.

Spectra were also measured to calculate reflectance values for other test points such as 6B, 6C, and 6D. The same phenomena, an increase in reflectance with an increase in view zenith angle , was observed at all test points in both principal plane and perpendicular to the principal plane. Data from the remaining test points not shown here are included in Appendix A.1.1.1.

4.1.1.2 Normalized Scale

On an absolute scale, it is shown that all bands have a similar angular dependency. To determine which band was most affected by the BRDF, reflectance values at all view zenith angles were normalized which are presented in Figure 4.3 and 4.4.

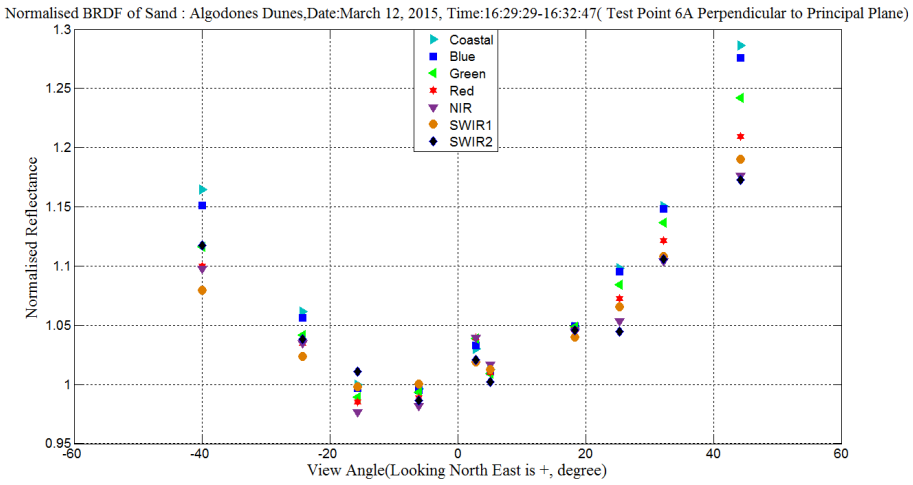

Figure 4.3. Normalized 6A perpendicular to principal plane.

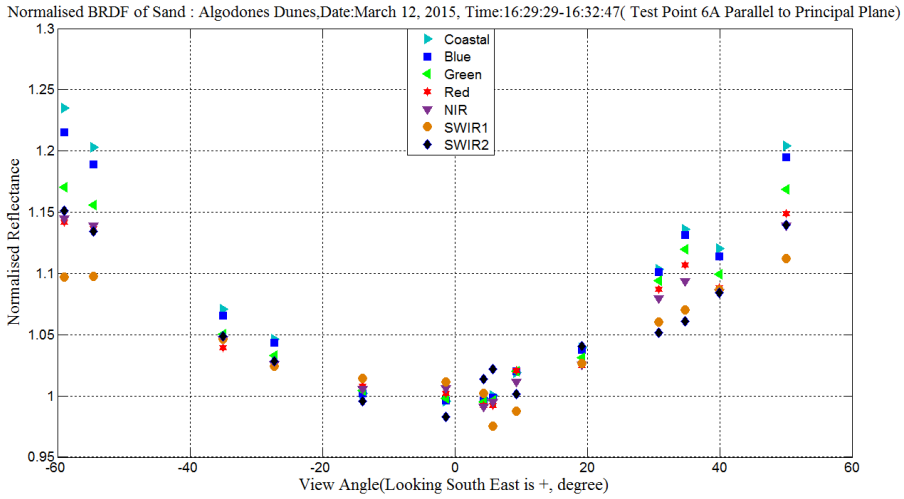

Figure 4.4. Normalized 6A principal plane.

Data from remaining test points not shown here are included in Appendix A.1.1.2. To normalize the data, first a quadratic equation of the following form was fitted to each

band.

$$y = ax^2 + bx + c \tag{4.1}$$

The minimum value of the above equation was found by differentiating with respect to x, dy/dx= 2ax + b. Thus the quadratic equation has a minimum value at $\frac{-b}{2a}$. The minimum value of the quadratic equation is then found by putting the calculated minimum value into 4.1. The reflectance values at all view zenith angles were normalized by dividing absolute reflectance values by the minimum value from the fitted quadratic equation. Since the absolute reflectance value is divided by the minimum value from the fitted curve, the normalized reflectance is less than 1 at some view angles. Figures 4.3 and 4.4 show that the Coastal band has the highest normalized reflectance. Also, generally the SWIR2 band has the lowest normalized reflectance, although at times the SWIR1 band has the lowest reflectance. Thus, it is observed that spectrally the BRDF effect is more pronounced in the shorter wavelengths than in the longer wavelengths. The effect is also more pronounced at higher view zenith angles than lower view zenith angles.

4.1.2 Comparing Two Flat Surfaces of the Algodones Dunes

While analyzing the spectral responses of spatially different sand samples from the Algodones Dunes, it is interesting to see how much similarity exists between the sand of similar surfaces but different locations of the dunes. In order to investigate this, measurements from two nearly flat surfaces of the dunes are compared with each other, shown in Figure 4.5:

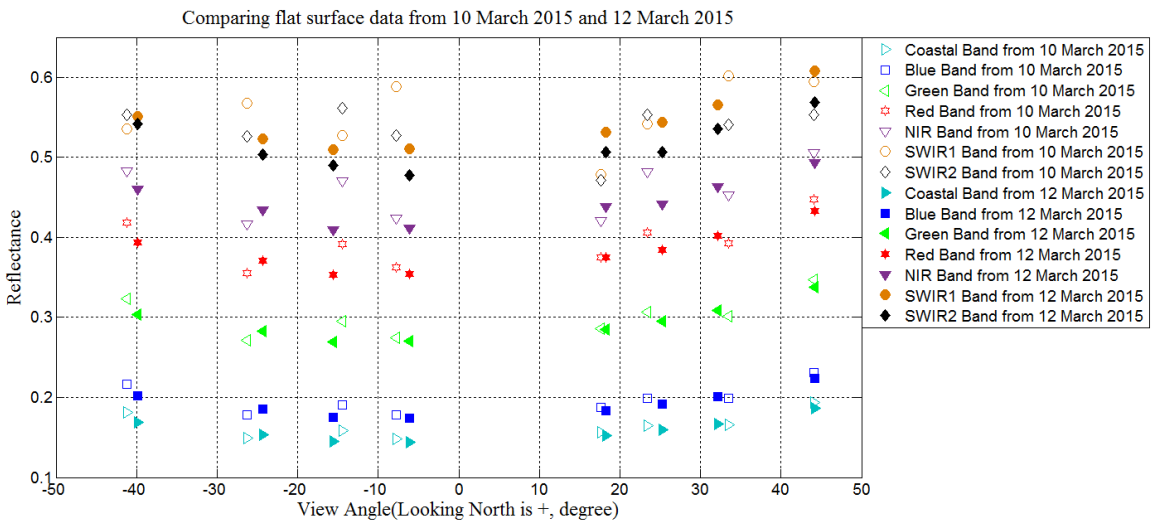

Figure 4.5. Comparison of flat surfaces of the Algodones Dunes.

Figure 4.5 shows a comparison between two different flat surface measurements from two different days. The solid symbols represent banded reflectance values of the flat surface from 12 March, 2015 and white hollow symbols represent the banded reflectance values of the flat surface from 10 March, 2015. The dataset from 10 March, 2015 was measured in the morning, at 8:42 AM, while the data set from 12 March 2015 was obtained in the morning at 9:30 AM. Measurements made at some view angles were eliminated to observe only common angles to simplify comparison between the two data sets. The two data sets look similar to each other, however, they have different reflectance values despite being flat surfaces since the data sets had slightly different acquisition times. The quantitative difference between two flat surfaces is summarized below in Figure 4.6 and Table 4.1.

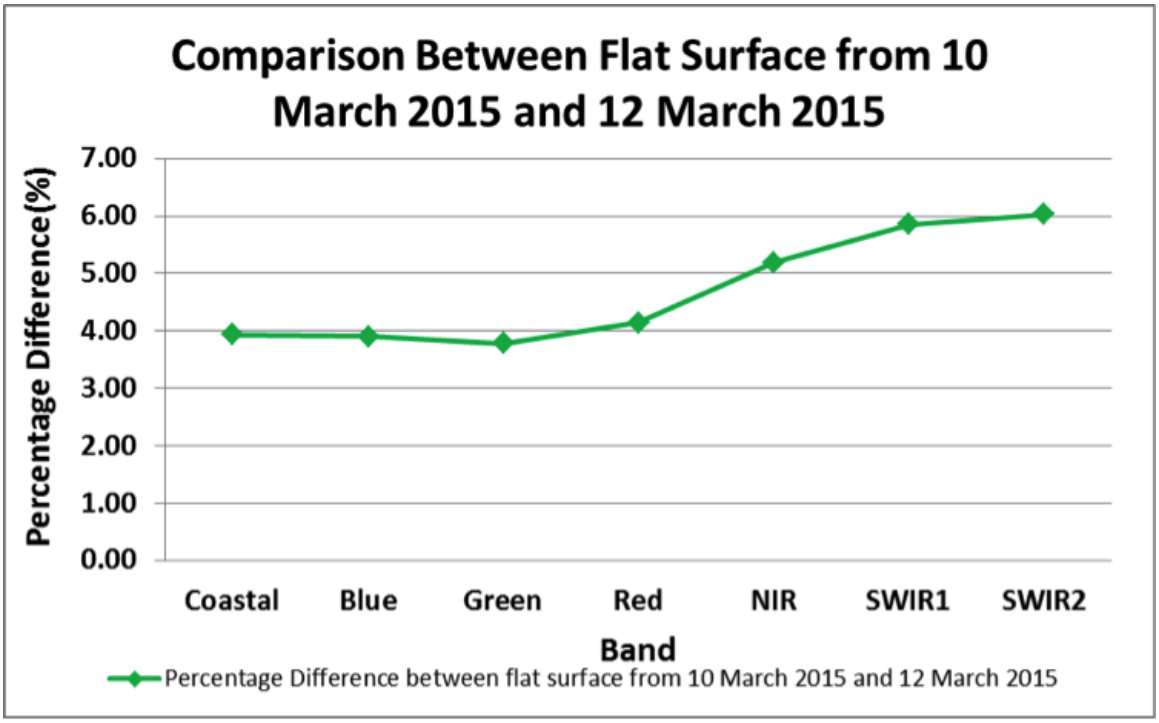

Figure 4.6. Comparison of flat surfaces of the Algodones Dunes from 10 March 2015 and 12 March 2015

Table 4.1. Comparison between flat surface from 10 March and 12 March 2015

Bands	Coastal	Blue	Green	Red	NIR	SWIR1	SWIR2
Percentage Difference(%)	3.94	3.90	3.79	4.14	5.19	5.86	6.03

Percentage difference was calculated by taking the absolute difference between the banded reflectance values of two flat surfaces and then dividing by the reflectance values of the flat surface from 10 March, 2015. Percentage difference was calculated at each view zenith angle for each band. The percentages for different view angles were averaged to obtain single percentage difference values for each band. The same process was repeated for all bands and results are summarized in Table 4.1 and Figure 4.6. Since, two measurements are from different locations in the field on different days, atmospheric conditions and solar angles were also different for the two measurements. Despite these

factors, percentage differences are within 6%, which is smaller than expected. If the two measurements were taken simultaneously, the percentage difference between them would have been less than 6% because difference in reflectance value due to different solar angles will be minimized.

4.2 Results from Laboratory

During the field campaign, only a limited number of measurements were taken. Since the amount of time that could be spent at the Algodones Dunes was limited, the idea was to correlate the field measurements with lab measurement and develop a BRDF model based on the lab measurements alone. In order to do so, sand samples were brought from the Algodones Dunes to the laboratory. The laboratory setup was developed to simulate the environment of the Algodones Dunes.

4.2.1 Comparison of Hyperspectral Data

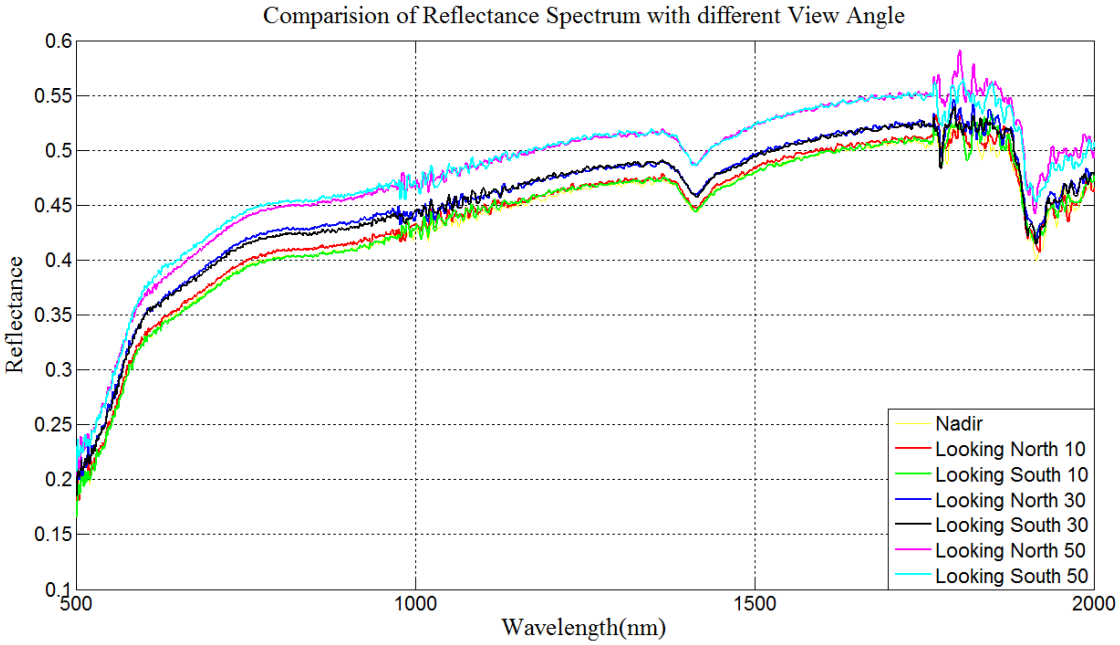

Figure 4.7. Comparison of hyperspectral reflectance spectrum with different view zenith angles.

Comparison of the reflectance spectrum while looking north or south in the perpendicular to principle plane is shown in Figure 4.7. In the lab, the name convention is as follows; if the light source is too the east, and if the optical head is rotated to the south then this is called ”looking north”, and if the optical head is rotated to the north then this is called ”looking south”. In laboratory measurements, when the mechanical arm was rotated in a clockwise direction it was assumed to be looking north and when the mechanical arm was rotated in an anticlockwise direction it was assumed to be looking south. Ideally, the spectra looking north and south should be the same because the sensor is looking in a series of directions that are orthogonal to the illumination direction, but in reality there will always be a slight difference between the hyperspectral data. In Figure 4.7 above, reflectance spectra look very similar from 1000 nm to 1700 nm, but beyond that there are slight differences between the hyperspectral curves looking north and south. However, at a shorter wavelengths the reflectance is slightly higher when looking from the south. Signal to noise ratio is low in higher wavelength which is clearly seen in Figure 4.7.

The hyperspectral curves shown in Figure 4.7 were banded to operational land imager (OLI) relative spectral response (RSR) and the result is presented in Figure 4.8. Operational land imager (OLI) is the Landsat-8 sensor which provides improved performance than the sensors from the previous Landsat sensors. Relative spectral response (RSR) profile is a curve showing the normalized response of a sensor to light at different wavelengths.

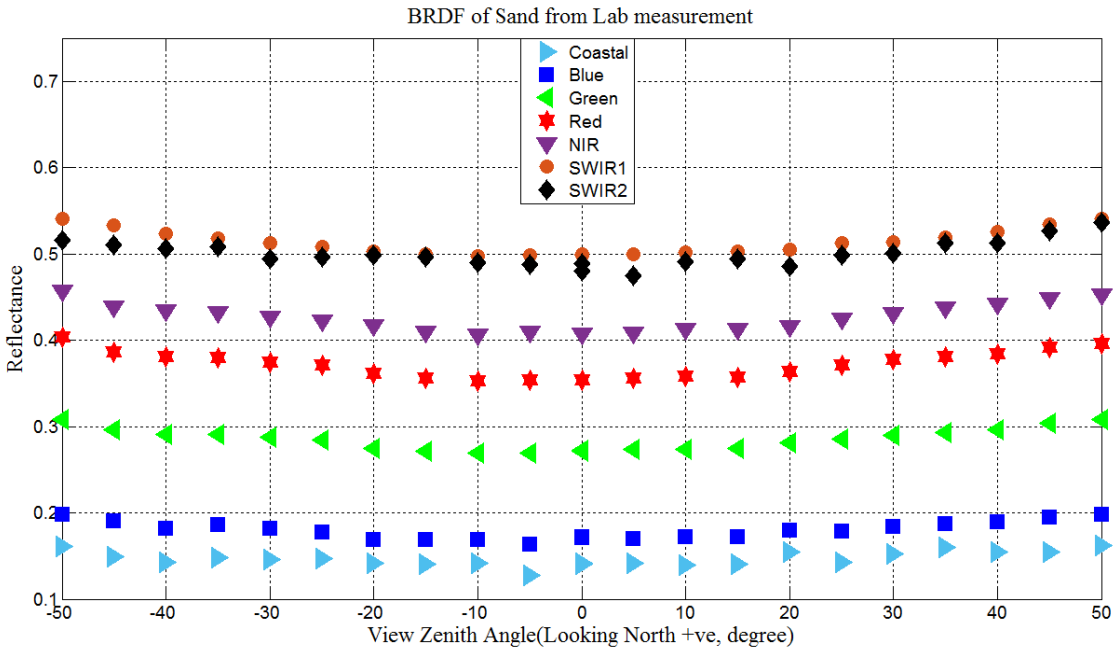

Figure 4.8. BRDF of sand sample from lab measurement.

As in the field measurements, all bands show an angular dependency: reflectance increases as view angle increases. The main objectives of performing laboratory measurements were to correlate lab measurements with field measurements. As shown in previous figures, there was no consistent angular resolution for view zenith angles while taking field measurements. Since the laboratory is a controlled environment, the angular resolution of view zenith angles was maintained for all measurements. While collecting data in the laboratory, view zenith angles varied from -50° to +50° in increments of 5°, where the clockwise direction was positive.

4.2.2 Repeatability of Lab measurement

The next step after being able to reproduce field measurements in a laboratory was to find out to what degree lab measurements were repeatable. In order to investigate the repeatability of laboratory measurments, three sets of measurements were taken with the

same illumination geometry, viewing geometry and sand sample. Those three sets of measurements were designated as first test run, second test run and third test run. The data of acquisition of those three test runs are mentioned in Table 4.2.

Table 4.2. Different test runs and their corresponding acquisition dates

Test run	Data of Acquisition(yyyy_mm_dd)
First	2015_10_14
Second	2015_10_14_second
Third	2015_10_19

The hyperspectral spectrum of each set of measurements was banded to the Operational Land Image(OLI) Relative Spectral Response (RSR) . The mean of all three sets of measurements was calculated to use as a reference. First, the absolute difference between the three sets of measurements and the reference was calculated. Then, each of the absolute difference values was divided by the reference to calculate percentage difference between an individual set of measurements and the reference. The results of the repeatability analysis of laboratory measurements are summarized above in Figure 4.9 and Table 4.3.

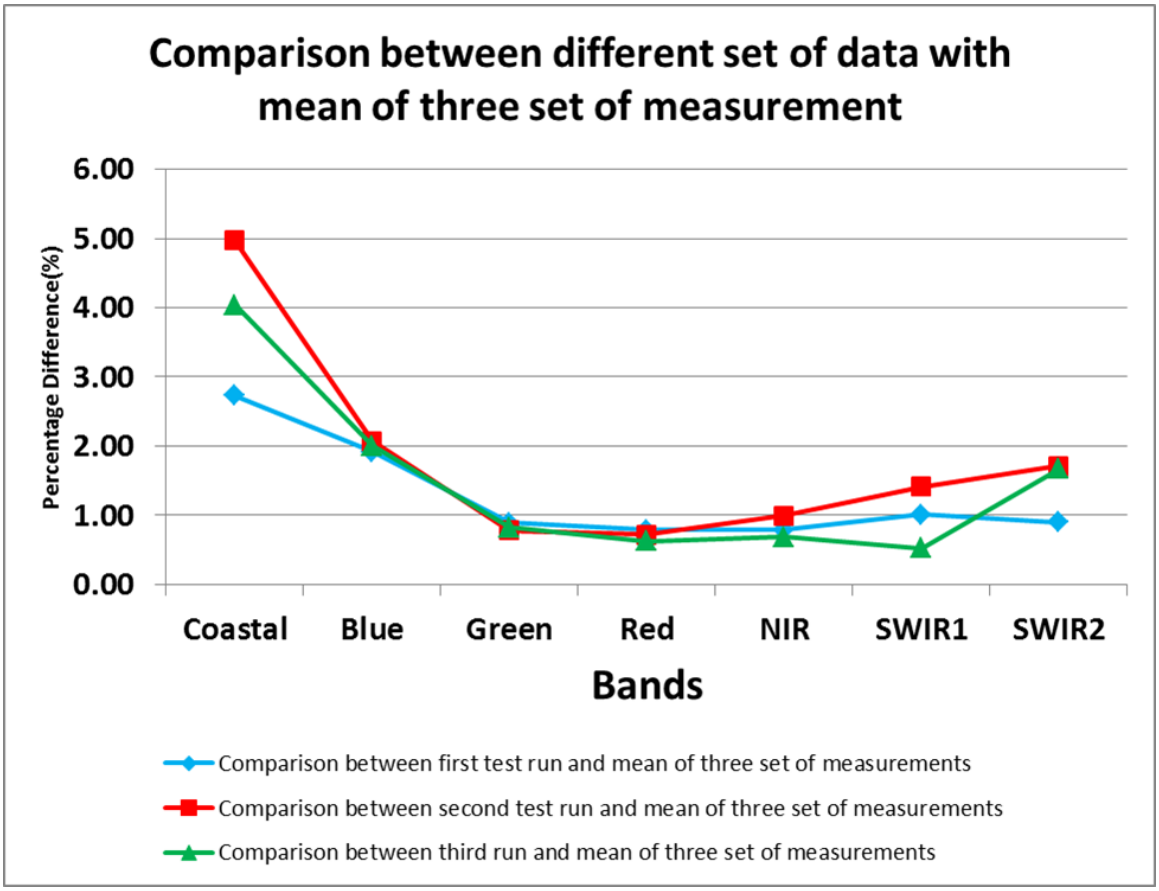

Figure 4.9. Repeatability of laboratory measurement

Table 4.3. Percentage difference between two sets of measurements.

Band	Percentage Differnce(%)		
	First Comparison	Second Comparison	Third Comparison
Coastal	2.73	4.97	4.04
Blue	1.92	2.07	2.00
Green	0.90	0.78	0.82
Red	0.79	0.72	0.63
NIR	0.79	1.00	0.69
SWIR1	1.01	1.42	0.52
SWIR2	0.90	1.72	1.67

In the laboratory, measurements could be repeated within approximately 2%, except for the Coastal Aerosol band. For the Coastal Aerosol band, a slightly higher degree of uncertainty is acceptable than other bands because the wavelengths of Coastal Aerosol are

prone to noise. Despite the uncertainties associated with the laboratory setup and the ASD spectrometer, the ability to repeat measurements within 2% showed that the setup was very consistent and reliable.

4.2.3 Comparison of Sand Samples from the Same Location in the Algodones Dunes

While collecting sand samples from the field, multiple sand samples were collected from the tops of different dunes. These sand samples from the tops of dunes were compared to determine whether their spectral responses were similar. Even though all three sand samples were from the tops of dunes, their spectral responses look different. The banded values for the spectral responses of sand samples from the tops of dunes are shown in Figure 4.10.

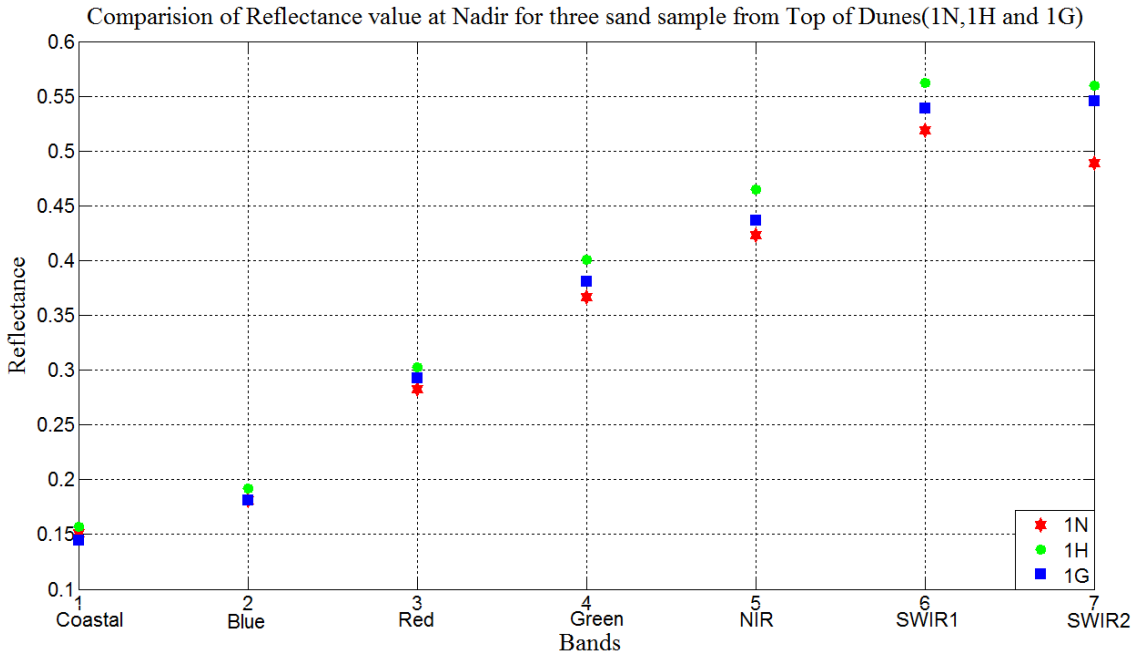

Figure 4.10. Comparison of banded value of nadir spectrum of three sand samples from top of dunes

Figure 4.10 and Table 4.4 show the difference between the reflectance of sands from the top of different dunes. As seen above, sand samples 1N and 1G are more similar to

each other in terms of reflective properties than 1N and 1H. The difference between the reflectances of sand samples in this case might be due to particle size, intrinsic brightness of the sand, or height of the dunes.

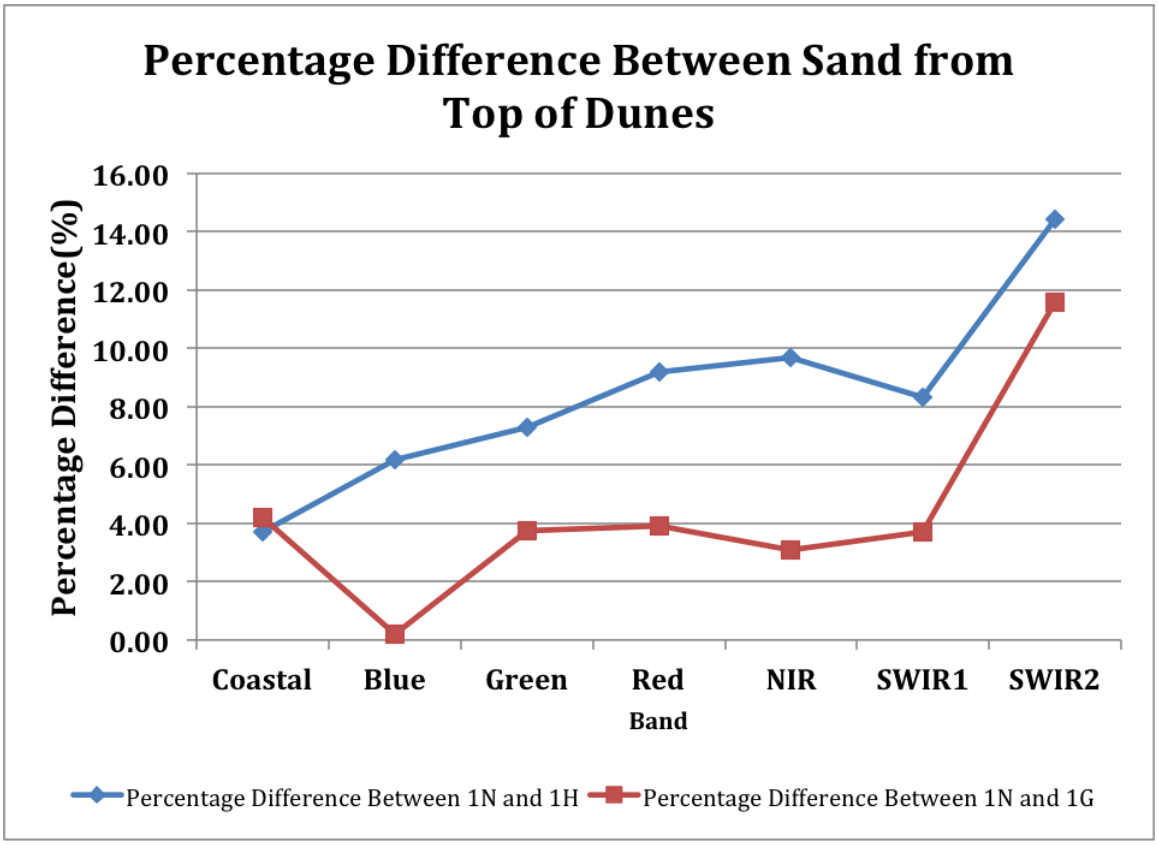

Figure 4.11. Percentage difference between sand samples from top of dunes

Table 4.4. Percentage difference between sand samples from top of dunes

Band	Sand Samples	Coastal	Blue	Green	Red	NIR	SWIR1	SWIR2
Pct Difference(%)	1N and 1H	3.70	6.18	7.30	9.20	9.70	8.33	14.45
	1N and 1G	4.19	0.19	3.75	3.91	3.10	3.72	11.58

4.2.4 Comparison of Sand Samples from Different Locations of Dunes

Sand samples brought from the Algodones Dunes were separated according to their location in the Dunes. The reflectance of sand samples was analyzed to see whether there is a pattern of reflectance according to the location of sand in the site. In Figure 4.12, it

was found that sand samples from the bottom of the dunes has a low reflectance, sand samples from the tops of dunes and leeward side of dunes are nearly the same, and a sand sample from the middle of dunes had the highest reflectance value.

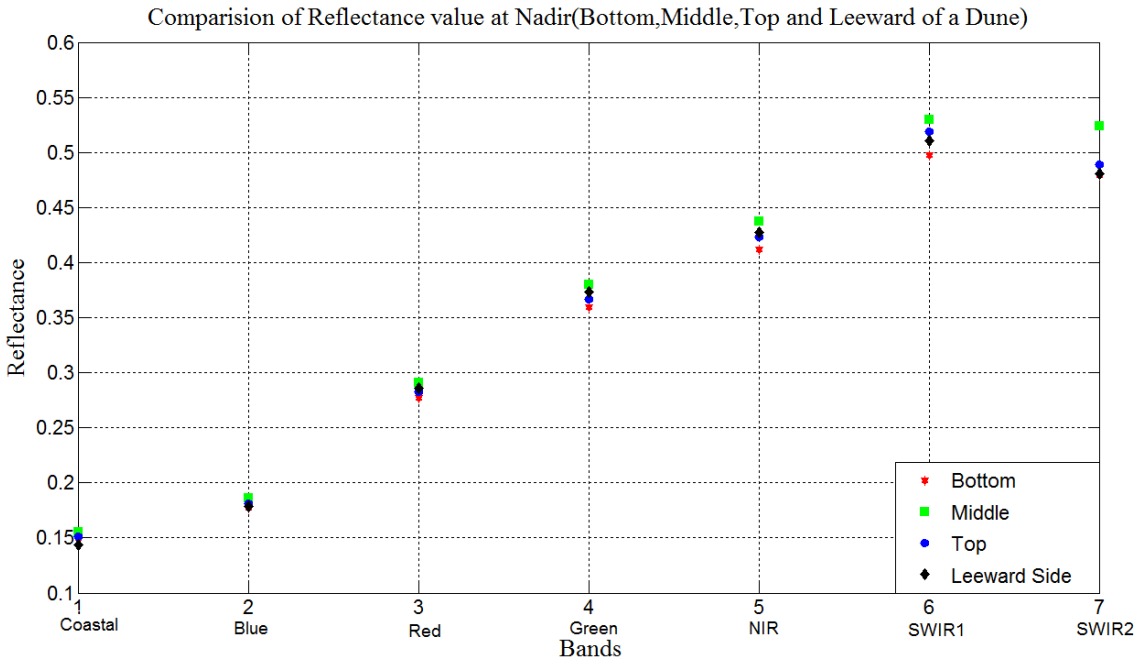

Figure 4.12. Comparison of banded value of nadir spectrum of sand sample from bottom, middle, top and leeward side of a dune.

The reason for this phenomena is that prevailing winds strike the windward side of the dunes and blow fine particles of sand on to the top of the dune, leaving heavier particles in the middle of the dune and leaving the heaviest particles at the bottom of the dune. Generally, winds deposit the finer particles of sand on top of the dune, but sometimes finer particles are deposited in the middle of the leeward side. So on the leeward side, sometimes finer particles of sand are left at the middle, heavier particles at the top, and the heaviest sand particles at the bottom of the dune. The finer particles of sand are brighter than the heavier particles of the sand. So the sand from the bottom of the dunes appears darkest and the sand from the middle of dunes appears brightest, there is

greater difference between reflectance values of sand from the bottom and the middle of the dunes, which is clearly shown in Figure 4.12 and Table 4.5.

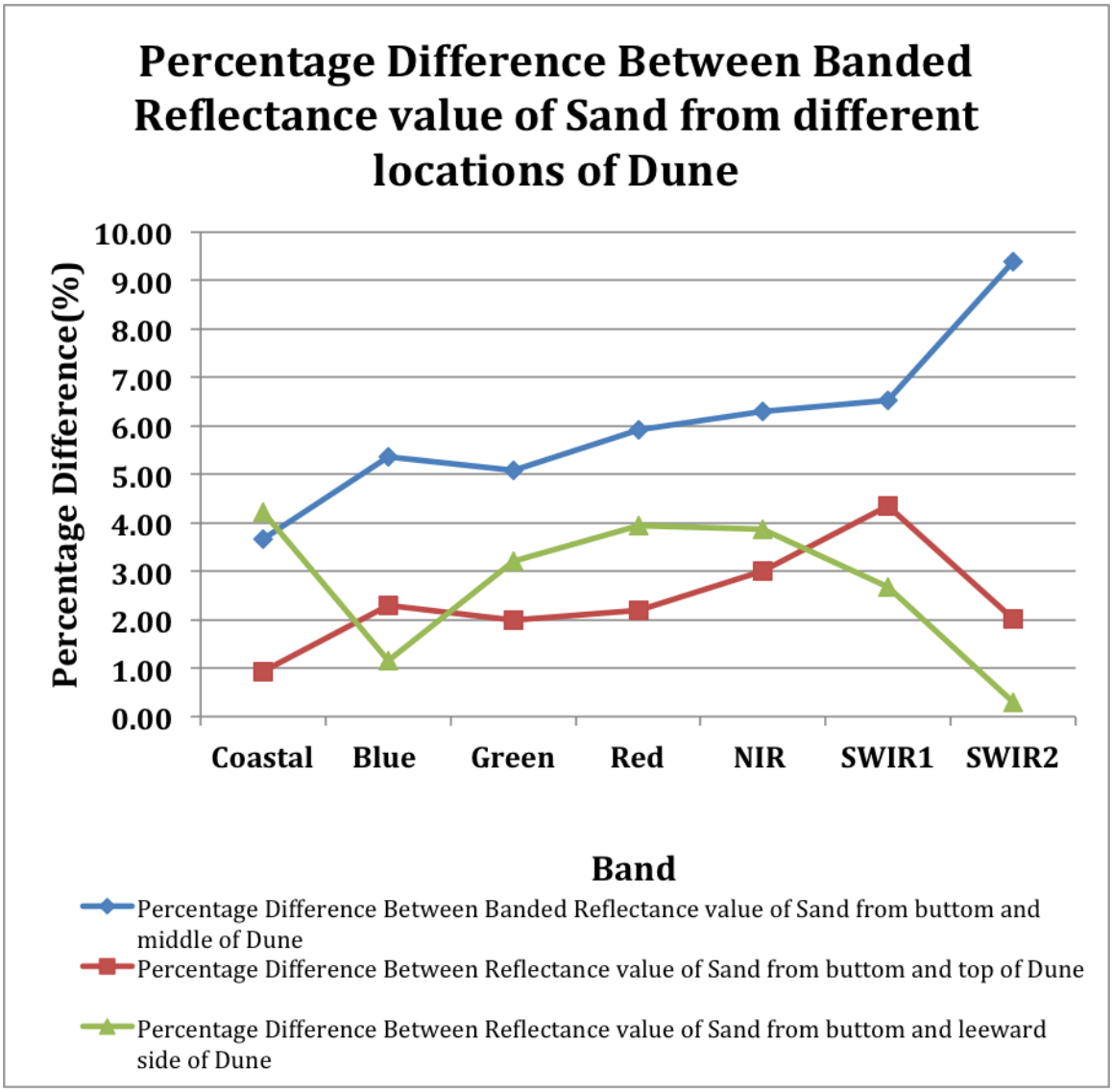

Figure 4.13. Percentage difference between banded reflectance value of sand from different location of dune.

Table 4.5. Percentage difference between banded value of sand samples from different location of Dune

Band	Sand Samples	Coastal	Blue	Green	Red	NIR	SWIR1	SWIR2
Pct Diff(%)	Bottom and Middle	3.66	5.36	5.09	5.93	6.31	6.52	9.39
	Bottom and Top	0.93	2.30	2.00	2.19	3.01	4.35	2.10
	Bottom and Leeward Side	4.22	1.17	3.21	3.94	3.87	2.67	0.3

4.2.5 Comparison Between Field Data and Lab Data

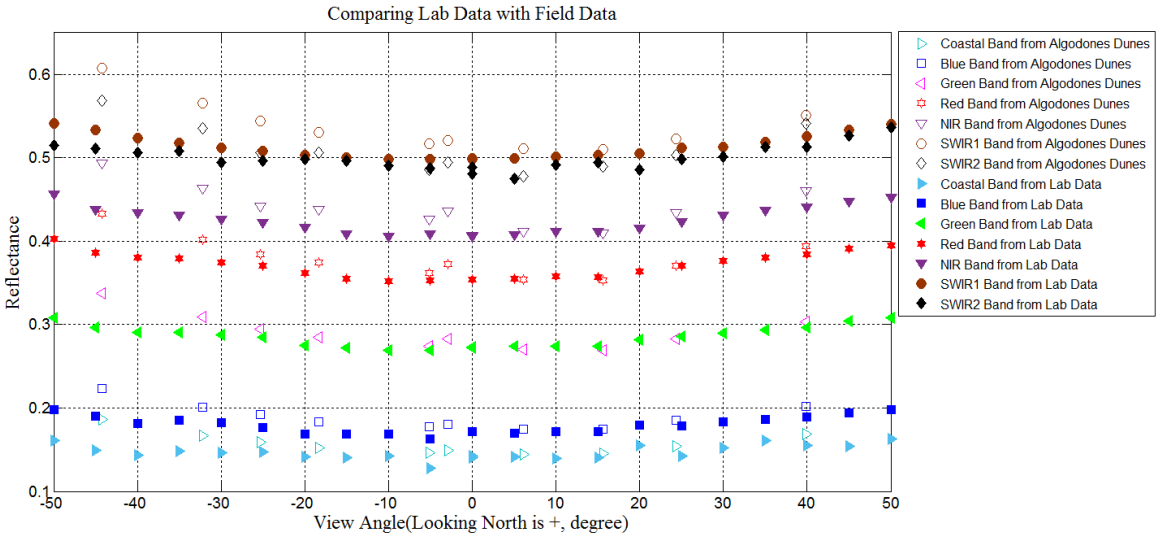

Figure 4.14. Comparison between field data and lab data

Since similar phenomena were observed in the laboratory as in the field, laboratory data were compared directly to the field data to see how accurately simulation of the the Algodones Dunes environment can be done in the laboratory. In Figure 4.14 above, laboratory data and field data were compared with each other, where solid symbols represent laboratory data and the hollow symbols represent data from the Algodones Dunes. The laboratory data line up closely with the field data for shorter wavelengths and for view angles less than or equal to 20°. Beyond view zenith angles of 20°, laboratory data showed less reflectance than in the field, and data from the lab deviates from the field data at longer wavelengths starting with the red band.

4.2.6 Comparison Between Field Data, Lab Data, and University of Lethbridge(ULB) Data

It can be seen that the nature of BRDF curves from the lab resemble the BRDF curves observed in the Algodones Dunes. A comparison is made between between these curves in Figure4.15, which shows a comparison of ground measurements with lab measurements and measurement done by the University of Lethbridge (ULB). The university of Lethbridge is an another group studying the surface reflectance properties of sand of the Algodones Dunes. The data are available only through the NIR band as the spectrometer used by the University of Lethbridge only measures the spectral response from 400 nm to 900 nm. The University of Lethbridge data are very close to SDSU field data and lab data, and support the same trend of increasing reflectance of sand as view zenith angle increases.

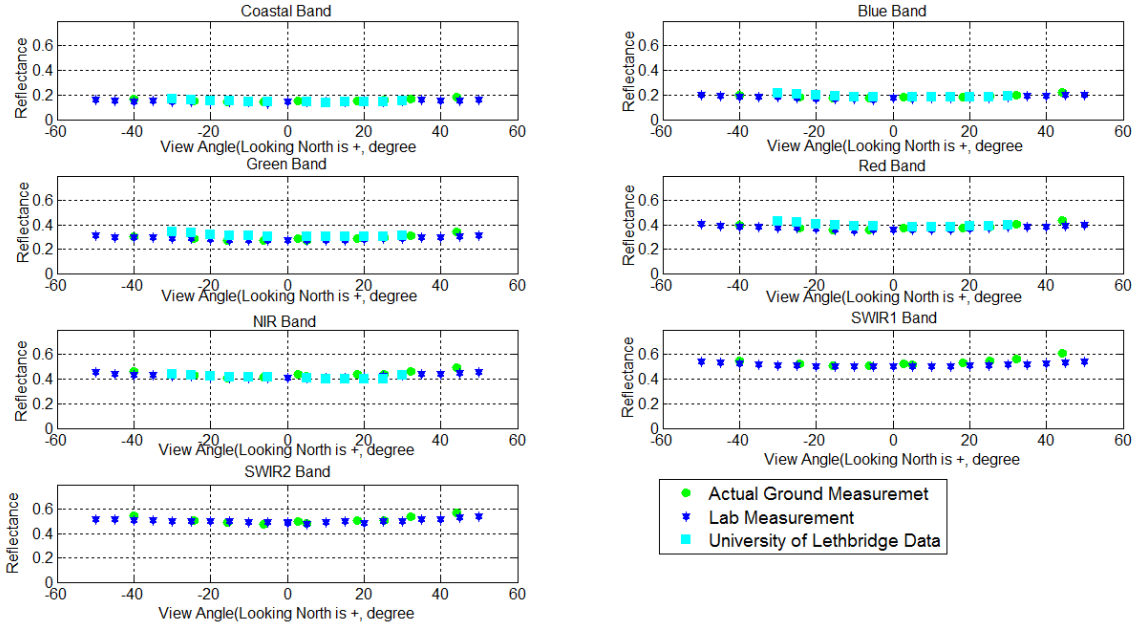

Figure 4.15. Comparison of ground measurement, lab measurement and University of Lethbridge for 6A Perpendicular to Principal Plane in view zenith angle of 45°

4.2.7 Comparison of Sand Samples from Different Test Points

When measurements were taken during the field campaign, all the surfaces were not flat, some surfaces are inclined. To simulate the inclined surface in the laboratory, the calculations detailed in Chapter 3 were used to adjust the view zenith angle to compensate for the incline that could not be truly created in the lab. The percentage difference between the field and lab measurements was then compared for three different test points. Figure 4.14 only shows the difference between lab and field data visually; to find a quantitative difference between laboratory and field data, a sand sample from a nearly flat surface was chosen to simulate. Overall, there were three field surfaces which were nearly flat and were possible to simulate in a laboratory. Those test points were 1C from March 10, and 6A and 6C from March 12. Figures 4.16 and 4.17 show the relative percentage differences and absolute percentage differences between the field measurements and corresponding laboratory simulation, respectively.

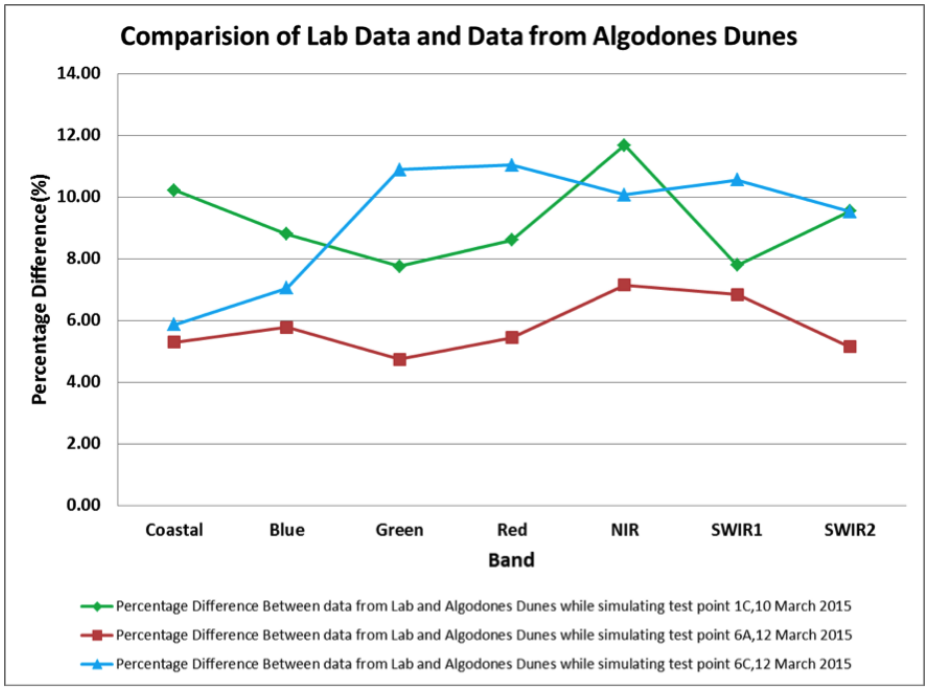

Figure 4.16. Comparison of lab data and different field data of the Algodones Dunes.

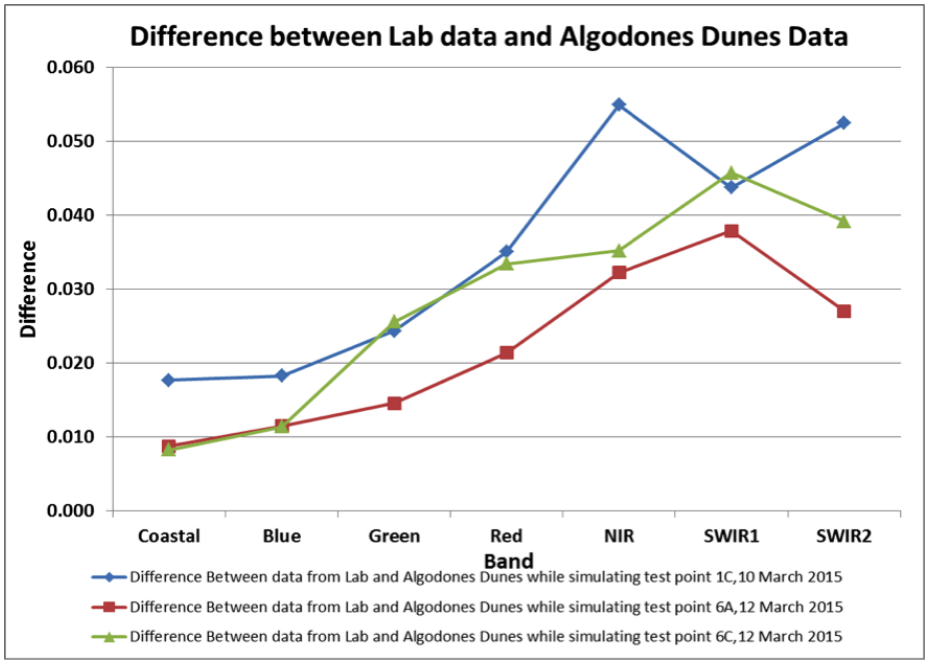

Figure 4.17. Comparison of lab data and different field data of the Algodones Dunes in absolute scale.

Thus, the flatter surfaces of the Algodones Dunes can be simulated more accurately

than inclined surfaces. Percentage difference between lab data and field data for 6A (best case) is within 6 % except for NIR and SWIR1 bands. When the difference is observed on the absolute scale, it is within 0.03 reflectance units except for in the NIR and SWIR1 bands.

4.3 Statistical Analysis

Before generating the BRDF Model, it was very important to determine whether the spectral responses of the sand samples from the Algodones Dunes were the same. This also determines whether the differences seen in previous charts are statistically significant. If the spectral responses of all sand samples are statistically the same, then a single BRDF model can be used for the whole the Algodones Dunes site. Otherwise, different BRDF models should be developed for different regions of the Algodones Dunes.

A halogen light source, ASD and mechanical arms were used to simulate the field environment in the laboratory. Therefore, different degrees of uncertainty are associated with each instrument used and it is very important to include these uncertainties while analyzing the spectral response of the sand.

To calculate the uncertainty of the instruments at different view angles and different bands, nine spectral responses of the same sand were measured in the laboratory, maintaining the same conditions through all measurements.

4.3.1 Multiple BRDF Run

Figure 4.18 shows nine BRDF runs for the NIR band using the same sand and same laboratory setup.

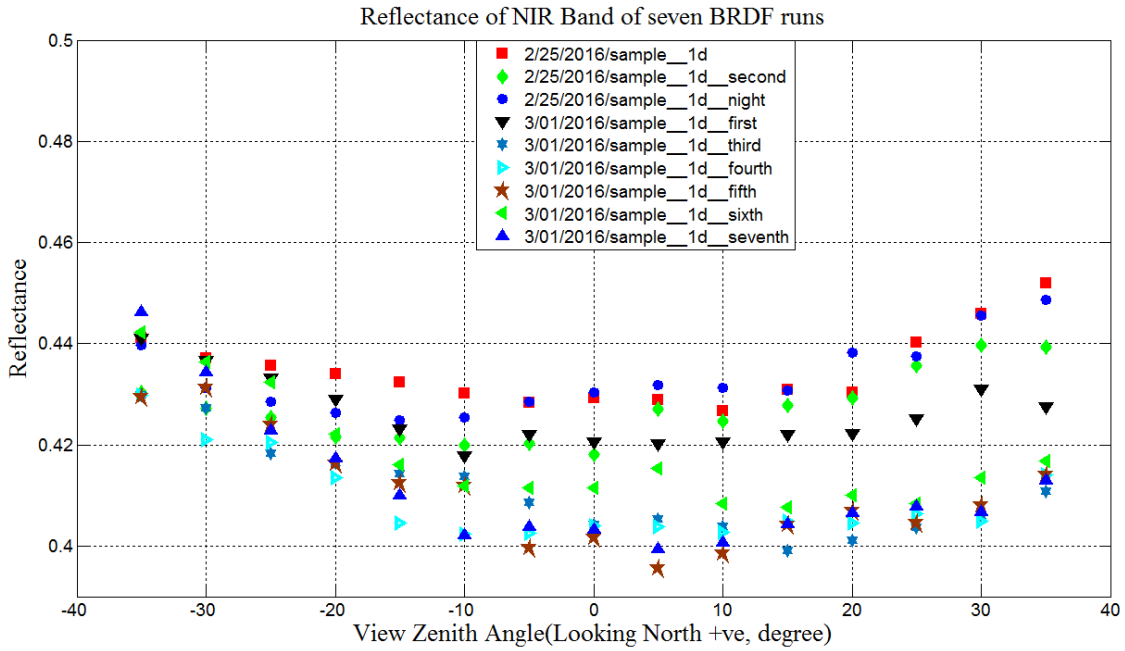

Figure 4.18. Multiple BRDF run for NIR band.

Ideally, all of the BRDF curves would have been on top of each other but, in reality, there are differences to a certain degree. Even though all conditions were maintained while taking the nine measurements, all BRDF curves look different from each other. These differences must therefore be due to uncertainties associated with the laboratory setup and instrumentation used to measure the spectral response of the sand. To better understand these uncertainties, nine BRDF measurement, of the same sand were taken while maintaining the same environment. Results are shown below.

Each reflectance value in Figure 4.19 was calculated by taking the mean of all reflectance values from the nine BRDF runs. Uncertainty associated with each angle was calculated by dividing the standard deviation of reflectance value by its mean. The standard deviation and uncertainty associated with each angle are shown in Figure 4.19 by an error bar and summarized in Table 4.6, respectively. From the figure, it appears that the

uncertainty is slightly higher for the angles looking North than the angles looking South. From Table 4.6, it can be concluded that the uncertainty is higher for the view zenith angles of 5° to 15 ° looking south, and it is also observed that the uncertainty is higher for the SWIR2 and Coastal Aerosol band as expected.

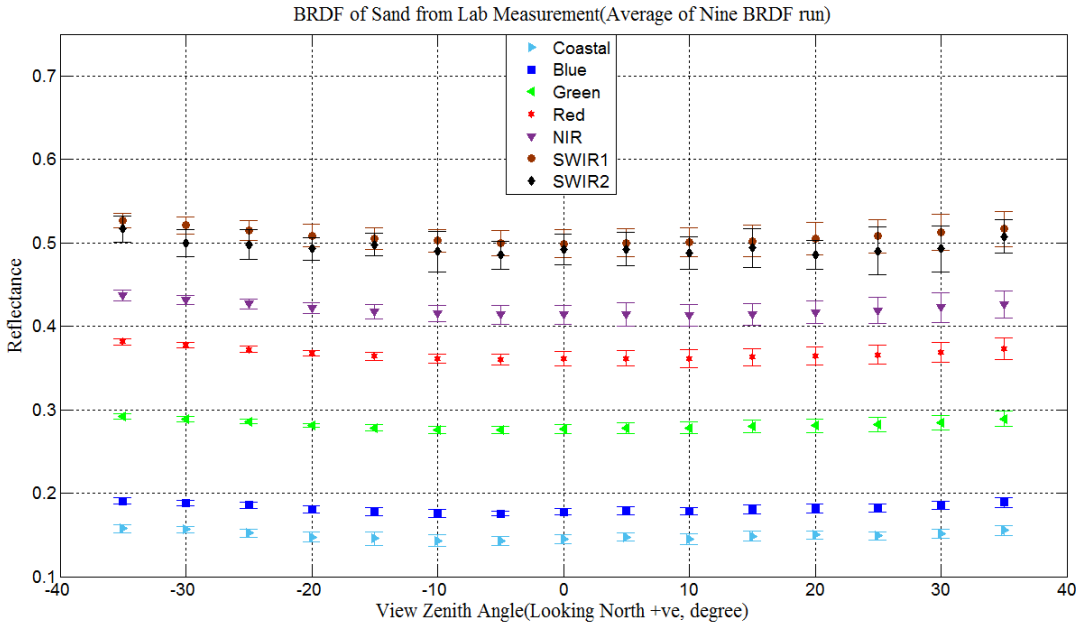

Figure 4.19. Uncertainty associated with each band and view zenith angles

Table 4.6. Uncertainty associated with each band and view zenith angles

Band	-35°	-30°	-25°	-20°	-15°	-10°	-5°	0°	5°	10°	15°	20°	25°	30°	35°
Coastal	3.43	4.38	3.92	3.51	3.45	3.43	3.80	3.78	3.82	4.95	5.54	4.31	3.15	2.43	2.91
Blue	2.64	2.43	2.88	2.93	2.79	2.52	3.23	2.12	1.71	2.77	2.83	2.51	2.31	1.92	2.11
Green	2.38	2.68	2.65	2.85	3.02	3.01	3.24	1.97	1.48	1.66	1.49	0.88	0.97	1.11	1.19
Red	2.45	2.92	2.91	3.03	3.19	3.25	3.49	2.36	1.90	1.62	1.37	0.87	0.89	0.93	0.95
NIR	3.29	3.07	3.14	3.25	3.72	4.24	3.83	2.74	2.70	2.28	2.05	1.60	1.41	1.25	1.53
SWIR1	3.33	3.51	3.73	3.81	3.96	4.25	4.14	3.33	3.10	2.67	2.54	2.63	2.31	2.01	1.67
SWIR2	4.00	3.99	4.75	3.58	5.84	5.60	4.00	3.71	3.51	5.01	2.69	2.76	3.61	3.23	2.98

Each reflectance value in Figure 4.19 was calculated by taking the mean of all reflectance values from the nine BRDF runs. Uncertainty associated with each angle was calculated by dividing the standard deviation of reflectance value by its mean. The standard deviation and uncertainty associated with each angle are shown in Figure 4.19 by an error bar and summarized in Table 4.6, respectively. From the figure, it appears that the

uncertainty is slightly higher for the angles looking North than the angles looking South. From Table 4.6, it can be concluded that the uncertainty is higher for the view zenith angles of 5° to 15 ° looking south, and it is also observed that the uncertainty is higher for the SWIR2 and Coastal Aerosol band as expected.

4.3.2 Fitting a Polynomial to the BRDF Curve

The next step was to determine if the BRDF curve as a function of viewing angle was quadratic or cubic in nature. A linear model was fitted to the mean reflectance graph and statistical results as shown in Table 4.7, 4.8 and 4.8 were analyzed. The results presented in Table 4.7, 4.8 and 4.8 were the R (Statistical Package) output.

Table 4.7. Fitting polynomial on BRDF curve of green band

Call:
$lm(formula = mean\_value\$Green \sim poly(mean\_value\$X, 3))$

Residuals:

Min	1Q	Median	3Q	Max
-0.0035179	-0.0022937	0.0005846	0.0012216	0.0055120

Coefficients:

	Estimate	Std. Error	t value	$Pr(>\|t\|)$
(Intercept)	0.2856190	0.0006149	464.534	<2e-16 ***
poly(mean-value$X, 3)1	0.0067750	0.0028176	2.405	0.0279 *
poly(mean-value$X, 3)2	0.0542501	0.0028176	19.254	5.57e-13 ***
poly(mean-value$X, 3)3	-0.0026484	0.0028176	-0.940	0.3604

Signif. codes: 0 '***' 0.001 '**' 0.01 '*' 0.05 '.' 0.1 ' ' 1

Residual standard error: 0.002818 on 17 degree of freedom

Multiple R-squared: 0.9569, Adjusted R-squared: 0.9493

F-statistic: 125.8 on 3 and 17 DF, p-value: 8.329e-12

Statistical results showed that the cubic term was not significant for the given BRDF curve, the linear term was less significant, and the quadratic term was significant. Low residual standard error and high adjusted R squared values of the model reflected the goodness of fit for the quadratic model. The P value of the F statistic was much smaller than the significance level, which implies the linear model is significant.

Table 4.8. Fitting polynomial on BRDF curve on green band using only linear term

Call:
$lm(formula = mean\_value\$Green \sim mean\_value\$X)$

Residuals:

Min	1Q	Median	3Q	Max
-0.0163749	-0.0121074	0.0006017	0.0070900	0.0248225

Coefficients:

	Estimate	Std. Error	t value	$Pr(>\|t\|)$
(Intercept)	2.856e-01	2.781e-03	102.717	<2e-16
mean-value$X	4.883e-05	9.184e-05	0.532	0.601

Signif. codes: 0 '***' 0.001 '**' 0.01 '*' 0.05 '.' 0.1 ' ' 1

Residual standard error: 0.01274 on 19 degree of freedom

Multiple R-squared: 0.01446, Adjusted R-squared: -0.0372

F-statistic: 0.2827 on 1 and 19 DF, p-value: 0.6011

Table 4.9. Fitting polynomial on BRDF curve on green band using only quadratic term

Call:

$lm(formula = mean\_value\$Green \sim I(mean\_value\$X^2)$

Residuals:

Min	1Q	Median	3Q	Max
-0.005520	-0.003133	0.000662	0.002622	0.004622

Coefficients:

	Estimate	Std. Error	t value	$Pr(>\|t\|)$
(Intercept)	2.723e-01	1.031e-03	264.08	<2e-16 ***
I($mean - value\$X^2$)	1.449-05	8.398e-07	17.25	4.95e-13 ***

Signif. codes: 0 '***' 0.001 '**' 0.01 '*' 0.05 '.' 0.1 ' ' 1

Residual standard error: 0.003145 on 19 degree of freedom

Multiple R-squared: 0.94, Adjusted R-squared: 0.9368

F-statistic: 297.6 on 1 and 19 DF, p-value: 4.59e-13

An investigation of how much the linear and quadratic terms contributed to the model was performed. The approach was to observe one at a time and look at the resulting statistics of the fitted model. First, the quadratic term was removed from the model and the statistics of the model showed that the linear term was not significant. Second, the linear term was eliminated from the model and the statistics showed that the quadratic term was significant. When the statistics of a model with both a linear and quadratic term were compared to the model consisting of only the quadratic term, the standard residual error increased by only 0.001 while the adjusted R-square decreased by 0.01. Those parameters suggest that the quadratic term has the majority of effect on a model containing both a linear and quadratic term. The goodness of fit did not decrease when the

linear term was removed from model and thus it was concluded that the BRDF curve is quadratic in nature.

4.3.3 Comparison of Residual Error

The spectral responses of all sand samples were measured in the laboratory using two solar zenith angles. Unfortunately, data of two of the sand samples at a solar zenith angle of 45.00° were corrupted, so they were removed from analysis. So, for a solar zenith angle of 45.00° , there were data from 15 sand samples while there were data from 17 sand samples for the solar zenith angle of 54.4°. For both solar view zenith angles the data sets were first separated according to band. Then, a linear model was fitted to each band taking sample ‘1a’ as a reference, and it was checked whether the remaining sand samples were different from the reference sand sample. From this initial analysis, it was concluded that most of the sand samples were different from the reference sand sample. The main concern for fitting a linear model was to obtain information about the residual error for different bands, solar zenith angles, and BRDF runs so that a comparison could be made among them.

Figure 4.20 shows a comparison between the standard residual errors of different bands for nine BRDF runs and two solar zenith angles.

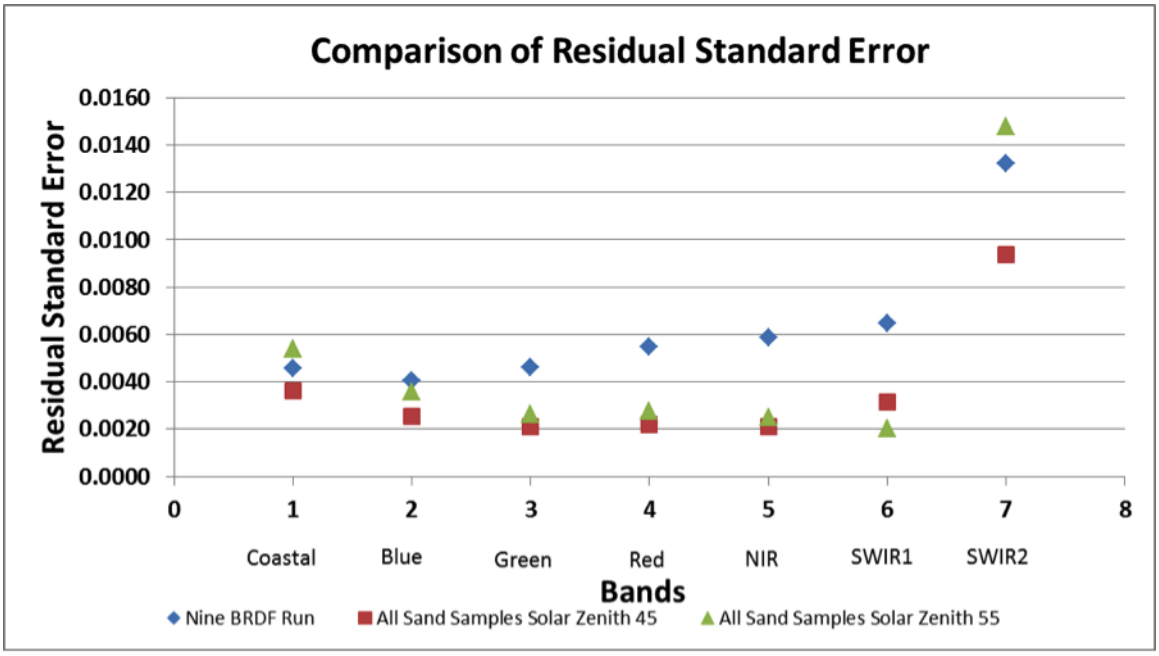

Figure 4.20. Comparison of residual standard error.

Interestingly, the standard residual errors for both solar zenith angles are less than the standard residual error for the nine BRDF runs except for the Coastal Aerosol and SWIR2 bands. This fact provided a sense that the spectral responses of different sands from the Algodones Dunes may be the same and lead to more rigorous analysis. However, a purely linear model was not sufficient to address the phenomena observed in the data. View zenith angle has a fixed effect on the spectral response of sands whereas the sand samples and BRDF runs have random effects on the spectral response. Only a linear mixed model can address both random and fixed effects at the same time.

A linear mixed model was developed for each band. Before interpreting results from the linear mixed model, it was important to know how well the model fit the data and whether the model violated any assumptions of the linear model. There are many ways to do this and several statistical tests exist to evaluate deviations from assumptions.

Generally, different diagnostic plots are evaluated after fitting a model to the data set being studied. Diagnostic plots developed for the BRDF linear mixed models are as follows: fitted residuals, histograms, and QQ plots.

4.3.3.1 Fitted Residuals of the Linear Mixed Model

Figure 4.21 shows residual plots of the fitted linear mixed models for all bands of all sand samples for a solar zenith angle of 55°.

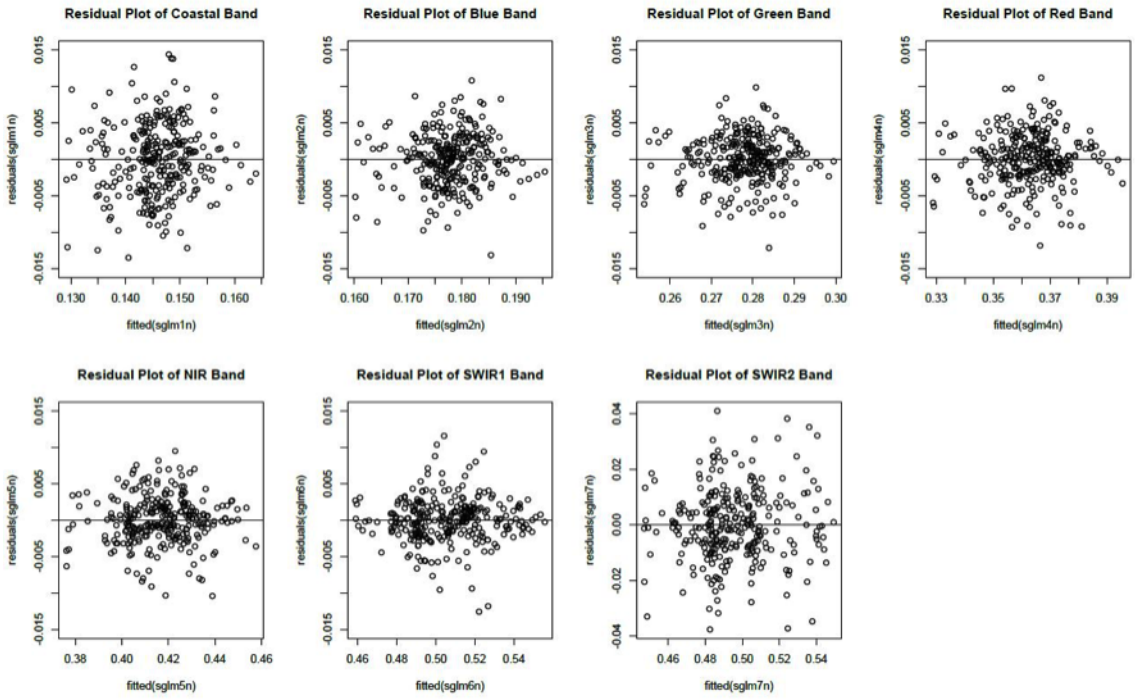

Figure 4.21. Residual plots for linear mixed models for all sand samples of solar zenith angle 55°.

As shown in Figure 4.21, the residuals are randomly dispersed about the horizontal axis. All residuals for all bands are within 0.01 except for in the SWIR2 band, meaning the remaining linear mixed models can predict the data within 1% error. Furthermore, the residuals are centered at zero for the range of fitted values and the plots have asymmetrical patterns which suggests the linear mixed model addresses all predictable variables. If the

model was not able to address all predictable variables, there would have been some pattern visible in the plots due to these unaddressed variables. Thus the linear mixed model is a good fit for the data available.

4.3.3.2 Residuals Histograms of the Linear Mixed Model

The histograms in Figure 4.22 show the underlying frequency distribution of residuals for the linear mixed model. It is observed that the histograms of the residual of all bands except the SWIR1 band have a standard normal distribution, which is due to the randomly distributed residuals. The histogram of the SWIR1 band has a slightly faster roll-off than the histogram of the rest of the bands. Overall, looking at the residuals histograms, it can be concluded that the residuals are randomly distributed.

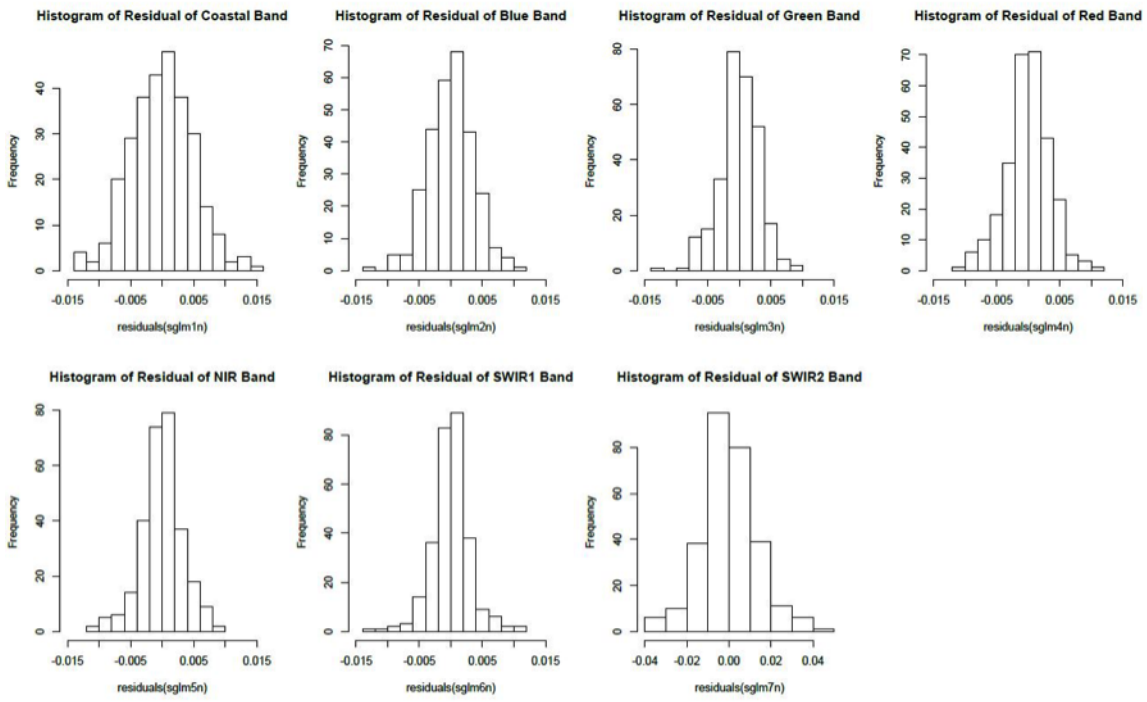

Figure 4.22. Histograms for linear mixed model for all sand samples of solar zenith angle 55°.

4.3.3.3 QQ Plot of Residuals of the Linear Mixed Model

Figure 4.23 shows quantile-quantile plots for all bands of all sand samples. The quantile-quantile plot is a graphical technique for determining if two data sets come from populations with a common distribution. If the residuals are perfectly normally distributed then the QQ plot will exactly follow the y=x line. Most of the residuals in Figure 4.23 are normally distributed and therefore follow a straight y=x line, but the QQ plot of the SWIR1 band deviates slightly from the y=x line which means that the sample quantile differs from the theoretical quantile. The residuals of all remaining bands, however, follow a normal distribution.

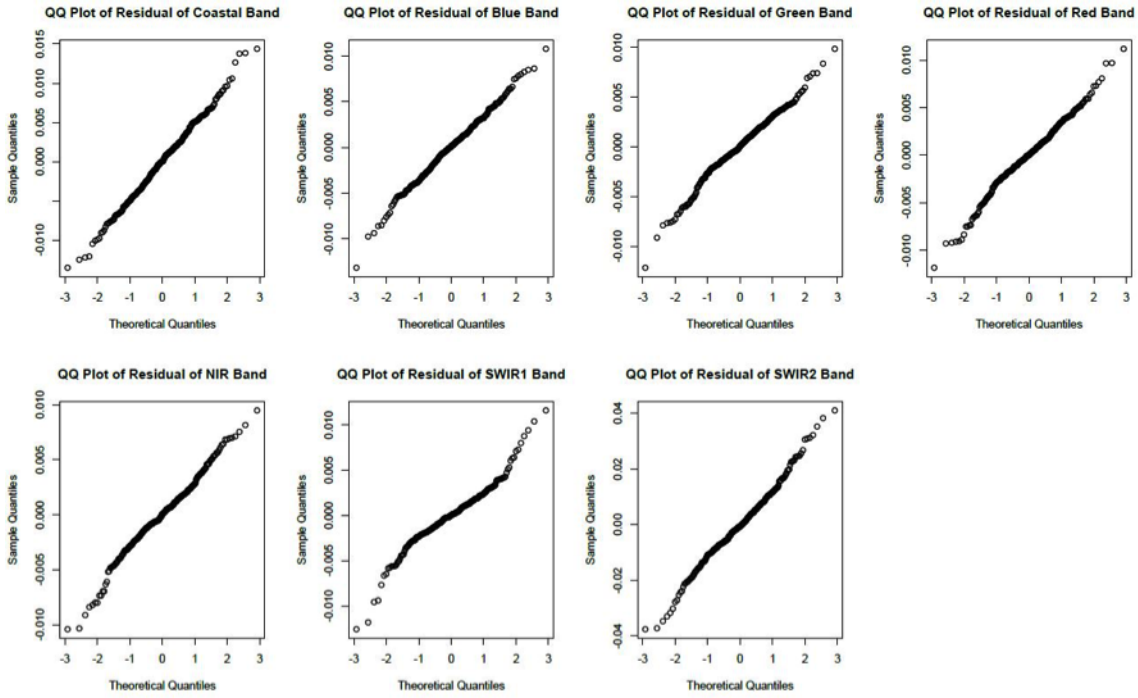

Figure 4.23. QQ plots for linear mixed model for all sand samples with solar zenith angle of 55°.

4.3.4 Comparison of Modeled Curves of Different Sand Samples and BRDF Runs

The generalized linear mixed model (GLM) was used to address the fixed effects and random effects observed in the data set of spectral response of sand samples. Figures, 4.24 and 4.25 show the modeled BRDF curves on top of the raw data for the Coastal Aerosol band measurments from the laboratory. As mentioned earlier, to measure nine BRDF runs, the same sample, 1A, was used. So, overall, sand sample '1A' has ten sets of data whereas the rest of the sand samples have only one set of data. Sample 1A is shown as the upper left plot of Figure 4.24, while the remaining plots are the other sand samples tested. For fitting a linear mixed model, data was separated according to band. All data for each band was kept in individual pools and linear mixed models were fitted to each pool. It was observed that not all raw data from the samples was quadratic in nature, some appeared to be cubic in nature while some even appeared as a higher degree of polynomial. Departure from a quadratic model is believed to be due to uncertainties in the instrumentation used to measure the spectral response of the sand samples in the laboratory. The Linear Mixed Model is able to address those issues and incorporate that uncertainty while predicting coefficients for intercepts and quadratic terms.

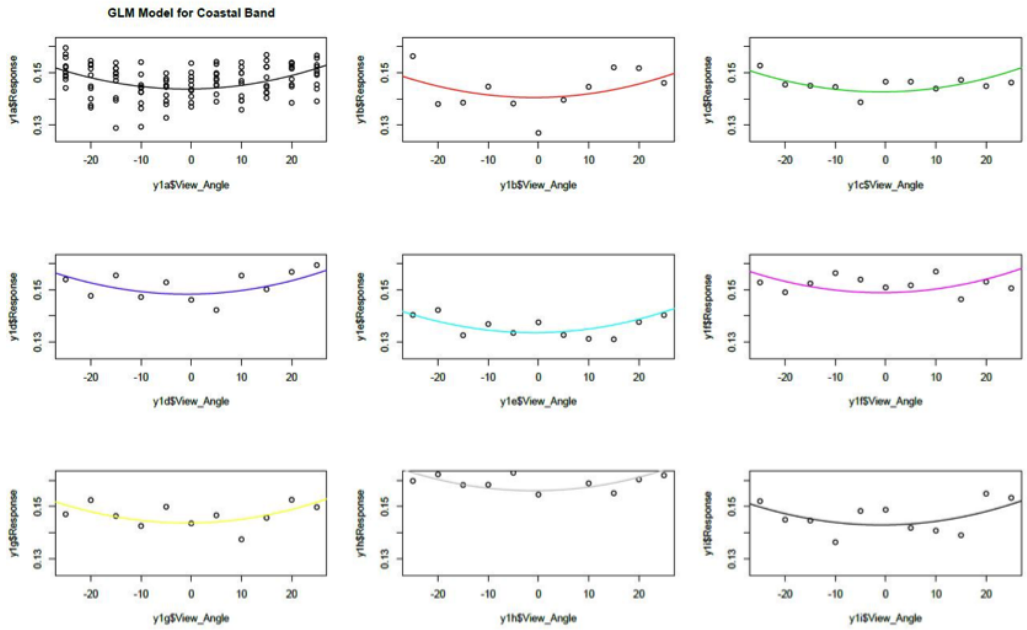

Figure 4.24. Modeled BRDF curves and raw data from lab for first nine sand samples, coastal aerosol band.

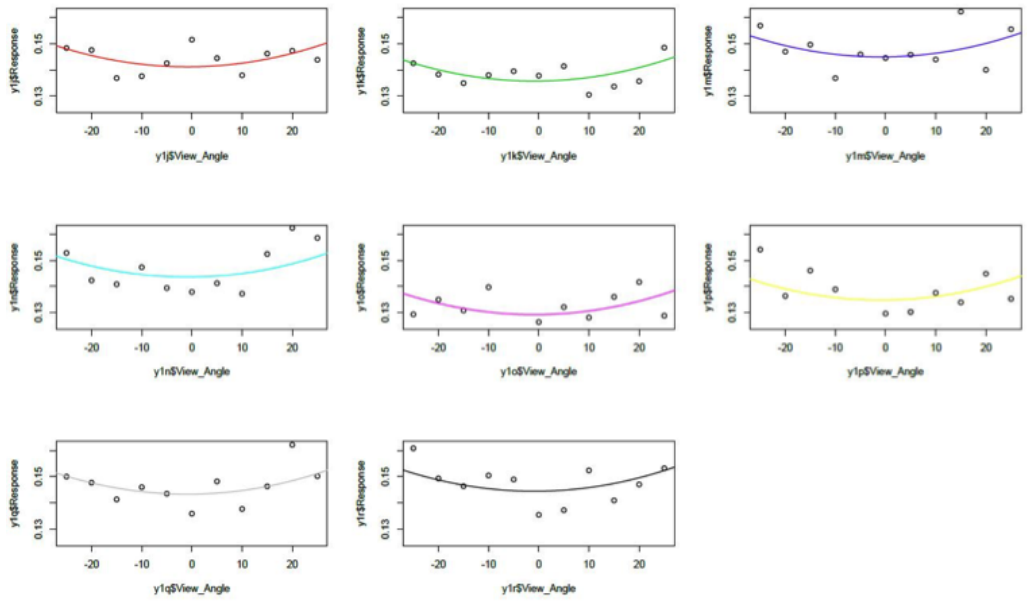

Figure 4.25. Modeled BRDF curves and raw data from lab for last eight sand samples, coastal aerosol.

As shown above, all sand samples don't have an equal number of BRDF runs.

Notably, sand sample ‘1A’ has ten BRDF run whereas the rest of the sand samples have a single BRDF run. Therefore, data from sample ‘1A’ has more dominance on modeling the intercept of all the sand samples. This is why the modeled curve for sand sample ‘1A’ goes through the middle of the raw data while predicted curves for the remaining sand samples may be slightly below the raw data. If the remaining sand samples had ten BRDF runs like sample 1A and had equal weight in the data pool, then the linear mixed model would have gone through the middle of the raw data.

To determine whether the spectral responses of the sand samples brought from Algodones Dunes were the same or not, curves modeled for those sand samples were compared as in Figure 4.26.

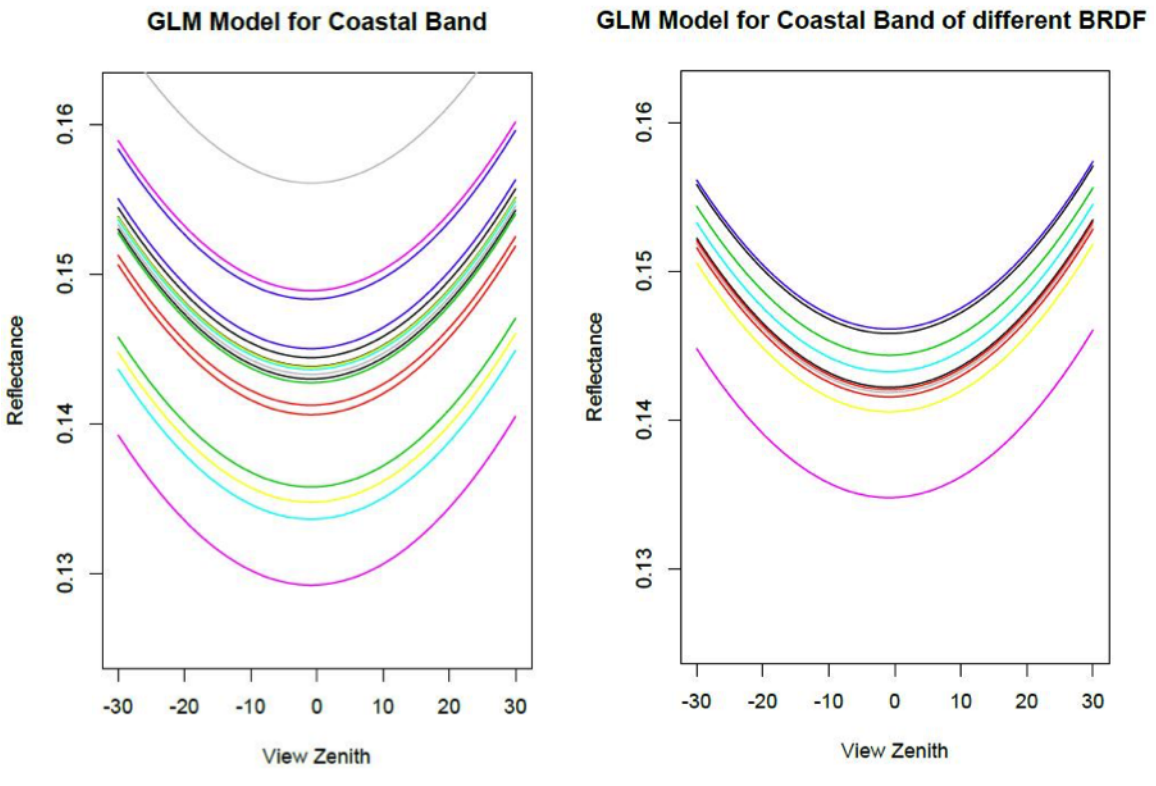

Figure 4.26. Comparison between modeled curve for different sand samples and different BRDF runs.

When modeled curves for multiple BRDF runs of the same sample are compared to curves modeled for different sand samples, it is observed that deviation in the spectral responses of different sand samples is approximately double the deviation in the spectral responses of multiple runs of the same sand sample. The difference between intercepts of all spectral responses of the same sand for multiple BRDF runs is approximately 0.0125, while the difference between intercepts of all spectral responses from different sand samples is approximately is 0.0275. While analyzing these two figures, two facts should be kept in mind. First, the spectral responses of the same sand for multiple runs, still have deviation of 0.0125. Second, if there were multiple BRDF runs for all sand samples, then the deviation in spectral responses for different samples would have been decreased and would likely be equal to the deviation of spectral responses for the same sand with multiple BRDF runs. Also, while predicting intercepts of sand samples, instrument uncertainties have a major contribution to differences in models. Taking into consideration all of the uncertainties of the lab measurements, the limited amount of data available and the results generated from the Linear Mixed Model, the spectral response of sand all over the Algodones Dunes is the same and thus a single BRDF model can be used for all of the Algodones Dunes.

4.4 BRDF Model for Perpendicular to the Principal Plane

A simple BRDF model is developed for perpendicular to the principal plane. Intercepts and quadratic terms for each band were calculated by taking the average of the intercepts from models of all sand samples and BRDF runs predicted by the linear mixed model. Intercepts for models of sand samples for both solar zenith angles studied and

summarized in Table 4.10. The change in solar zenith angles is reflected by the change in the intercepts of the models fitted for each data set. It can also be seen that a change in solar angle also causes a slight difference in the quadratic term of the BRDF curve.

Table 4.10. Simple BRDF model for perpendicular to principal plane.

Band	Solar Zenith 45°		Solar Zenith 55°	
	Intercept	Quadratic term	Intercept	Quadratic term
Coastal	0.1473	8.73E-06	0.1423	1.18E-05
Blue	0.1794	9.97E-06	0.1742	1.27E-05
Green	0.2799	1.14E-05	0.2696	1.39E-05
Red	0.3648	1.32E-05	0.3502	1.69E-05
NIR	0.4156	1.33E-05	0.3978	1.79E-05
SWIR1	0.5096	1.59E-05	0.4845	1.96E-05
SWIR2	0.5083	8.94E-06	0.4868	1.20E-05

CHAPTER 5 CONCLUSION

The Bidirectional Reflection Distribution Function of a Pseudo-Invariant Calibration Site has been studied using the Algodones Dunes. The field environment has been successfully simulated in a laboratory and used to replicate the phenomena observed during the field campaign. A simple BRDF model for the Algodones Dunes has been developed for perpendicular to the principal plane. This chapter summarizes the results, draws the conclusion of this project and gives direction for future work.

5.1 Summary of Results

A comprehensive field campaign was conducted to gain a better understanding about surface reflectance in deserts and to determine the efficacy of using the Algodones Dunes for absolute calibration of optical remote sensing satellites. Different test points were studied during the field campaign and sand samples from spatially different regions were brought to the SDSU lab for further analysis. The study showed that the surface reflectance of sand from the Algodones Dunes at off-nadir viewing angles is different than the surface reflectance at nadir. Off-nadir reflectance is a quadratic function of view zenith angle and is valid for both principal plane and perpendicular to the principal plane. Furthermore, field data from the University of Lethbridge along with ground reflectances calculated through SMACAA using approximately 50 images showed that surface reflectance changes quadratically as view zenith angle increases. To measure the BRDF of sand samples brought from the Algodones Dunes in a more controlled environment, a laboratory setup was built at SDSU. Data from the SDSU laboratory further showed that the reflectance of sand samples changes quadratically as view zenith angle increases. To

determine the repeatability of laboratory measurements, three sets of measurements were taken using the same sand and the same illumination and viewing geometry. Percentage difference of each set of measurements was calculated by considering the mean of the three sets of measurements as a reference. The results showed that the laboratory measurements are repeatable to within 2% except for the Coastal Aerosol, which was repeatable within 5%. It was difficult to obtain repeatability in the Coastal aerosol band because noise was more pronounced in the shorter wavelengths. To correlate field and lab measurements, a comparison between field and lab data was performed. The comparison showed that for view zenith angles up to 20°, lab data and field data closely matched each other. To simulate the field environment and measure the spectral response of sand samples in the laboratory, different components such as a halogen bulb, digital power supply, and mechanical arm were used to create the setup in the SDSU laboratory. A certain degree of uncertainty was associated with each component.

A Linear Mixed Model was developed in order to model the reflectance of different sand samples by taking the component uncertainties into account. The reflectance values predicted by the linear mixed model closely aligned with the raw data generated in the laboratory. Based on the data modeled by the linear mixed model, multiple spectral responses of the same sand sample and spectral responses of different sand samples were compared. The reflectance range of the modeled data for different sand samples was 0.06, whereas the reflectance range of modeled data for different BRDF runs of the same sand samples was 0.03. If more BRDF runs of different sand samples were included in the analysis, then the range of reflectance for different sand samples would likely decrease and fall within the range of reflectance for multiple BRDF runs of the same sand sample.

Based on that reasoning, it was concluded that the spectral responses of sand samples brought to the laboratory for further analysis were the same. A simple BRDF model was then generated for PPP by taking an average of the intercepts predicted by the linear mixed model for different sand samples and different BRDF runs of the same sand sample.

5.2 Conclusions

Upon completion of this project, the following conclusions were established:

- The field environment can be simulated in an SDSU laboratory with the ability to replicate phenomena that were observed in the Algodones Dunes.

  A comparison was done between the field measurement and laboratory measurement. All the surfaces in the Algodones Dunes were not flat. So those surfaces were simulated in the lab by compensating for the view angle. Percentage difference between laboratory and field measurements are within 7% (0.04 in reflectance units) for the best case and 12% (0.06 in reflectance units) for the worst case.

- Laboratory measurements are repeatable to within 2%.

  Three sets of measurements were taken to determine the repeatability of measurements and each of them was compared with the mean of the three set of measurements. Percentage difference for all sets of measurements was with 2% for all bands except Coastal Aerosol band.

- The BRDF curve for sand from the Algodones Dunes is quadratic in nature.

  A linear model was fitted to the mean reflectance value of the sand samples. Both cubic and linear terms were not significant. Only the quadratic term has major

influence on the data.

- The spectral responses of different sand samples from the Algodones Dunes are considered to be the same based on the linear mixed model analysis.

  The difference between the modeled intercept of the same sand sample for multiple BRDF runs is 0.0125 whereas for different sand samples it is 0.0275. If there has been multiple BRDF runs for each and every sand sample from the field. Then that deviation would have decreased and been approximately equal to the deviation of the same sand multiple runs.

- A simple BRDF model has been developed for angles that are perpendicular to the principal plane.

  A linear mixed model predicted the intercepts and quadratic terms for different sand samples and multiple BRDF runs of the same sand sample. All these intercepts and quadratic terms were averaged and a simple model was developed.

5.3 Direction of Future Work

In this study, samples from a small region of the site were brought back for further study in a laboratory. A more comprehensive analysis could have been completed if more sand samples from a different region of the Algodones Dunes were included in the study. One of the main challenges of this study was to address the uncertainty caused by the laboratory setup. In a future project, a light source with symmetric illumination and a more stable mechanical arm for the acquisition of data would reduce the uncertainty from the lab setup. Furthermore, analysis was only done for two solar zenith angles of 45° and 54.4°, but at the Algodones Dunes the solar zenith angle varies from 20° to 60° over a

year. It would therefore be beneficial to include analysis for solar zenith angle from 20° to 20° in future developments.

All of the analysis in this study is based on spectrally banded values. This analysis can be done from a hyperspectral perspective and the result can be compared with the banded value. From this preliminary study, a simple BRDF model has been developed for perpendicular to principal plane. A full BRDF model which includes all solar and view zenith and azimuth angles (supported by lab setup) can be developed. Once a full BRDF model is developed for the Algodones Dunes, absolute calibration models for Saharan Pseudo-Invariant Calibration Sites can be developed with appropriate normalization factors.

CHAPTER A Appendices

A.1 Data Acquisition Pattern

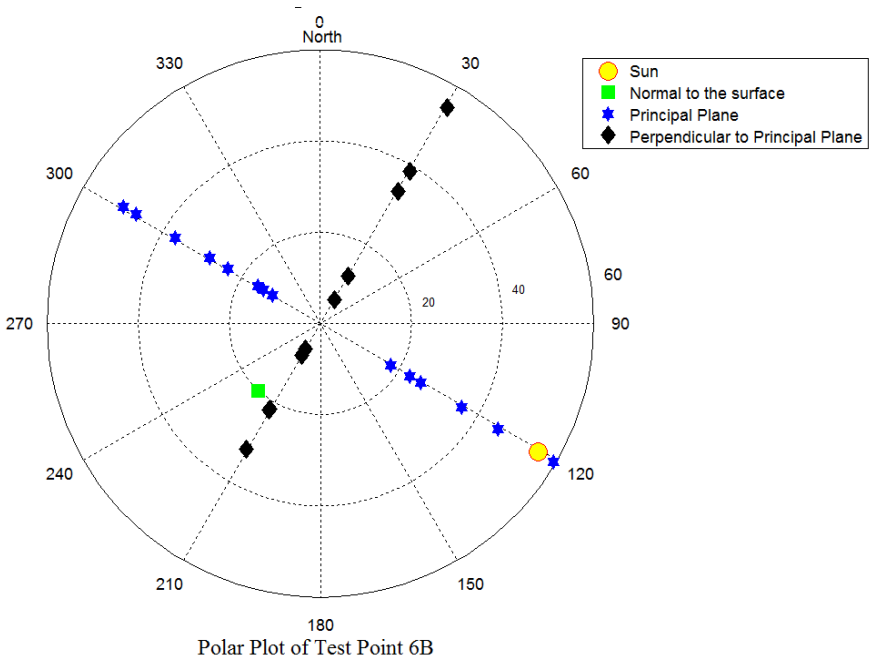

Figure A.1. Polar plot of test point 6B

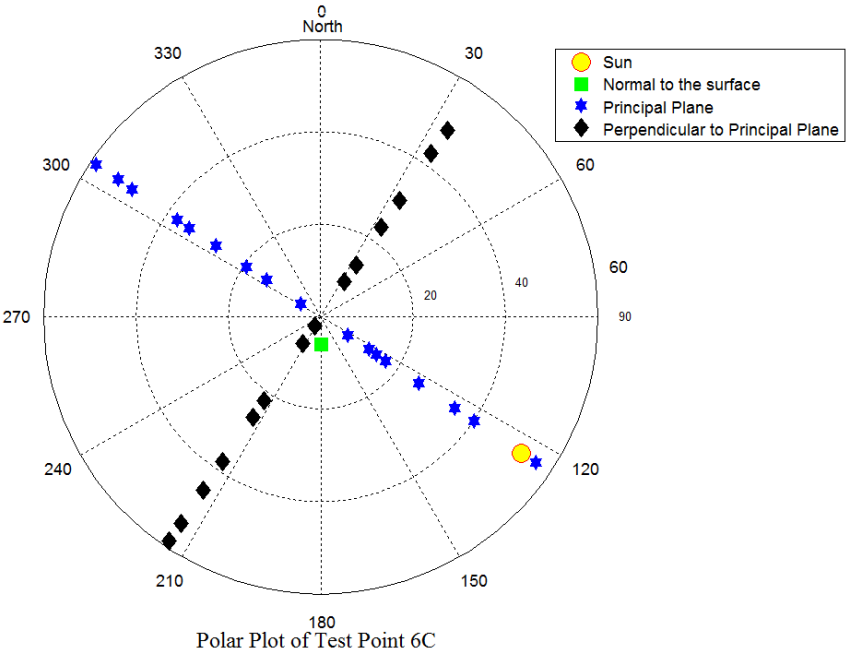

Figure A.2. Polar plot of test point 6C

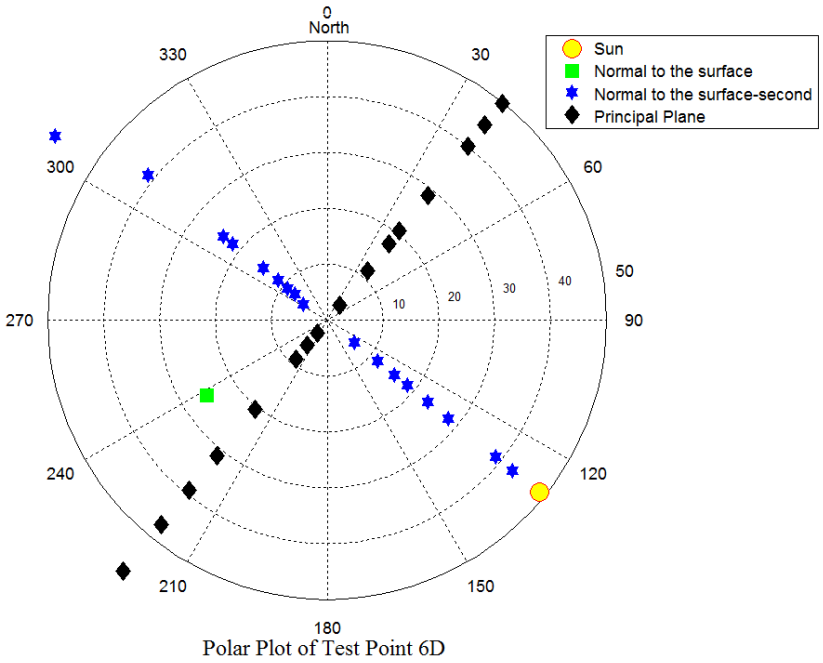

Figure A.3. Polar plot of test point 6D

A.1.1 Results from 12 March, 2015

A.1.1.1 Absolute Scale

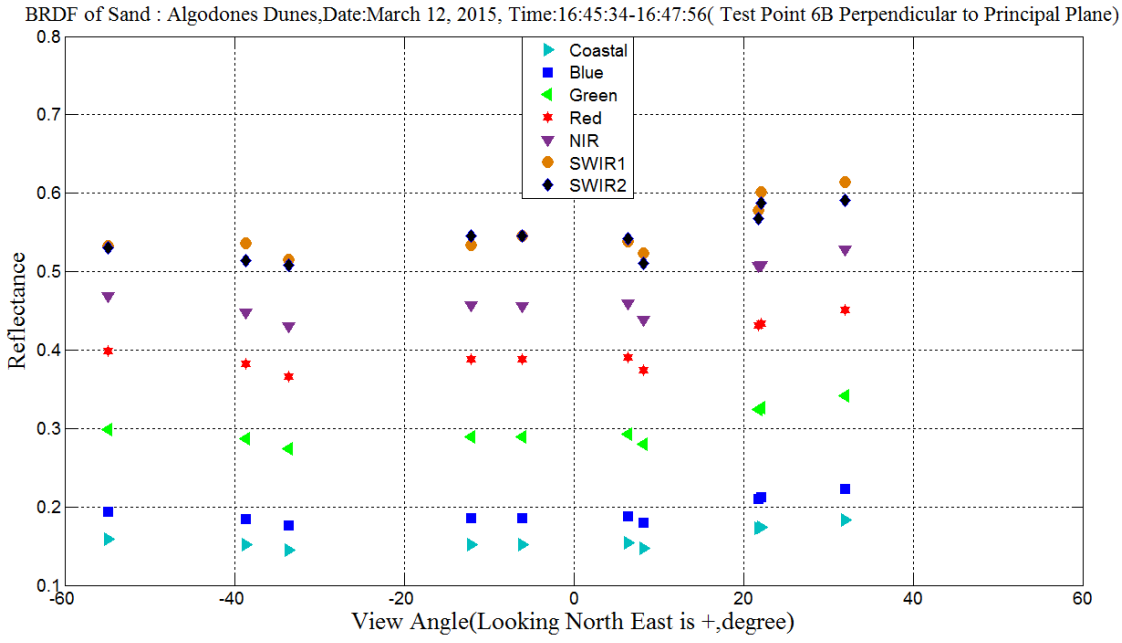

Figure A.4. 6B perpendicular to principal plane

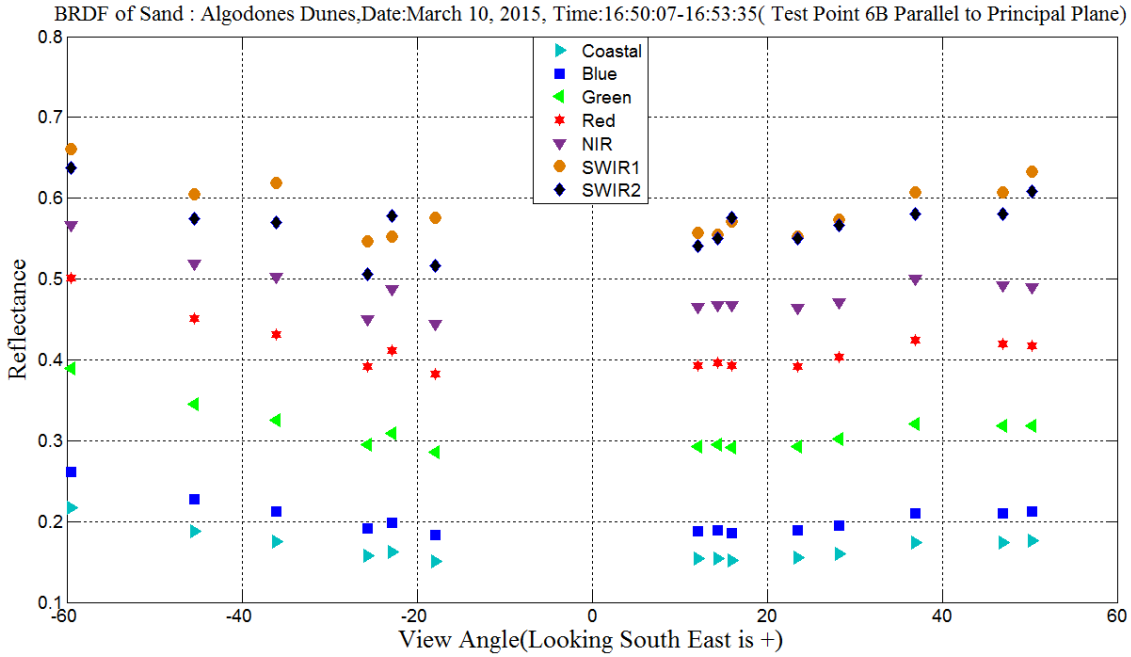

Figure A.5. 6B principal plane

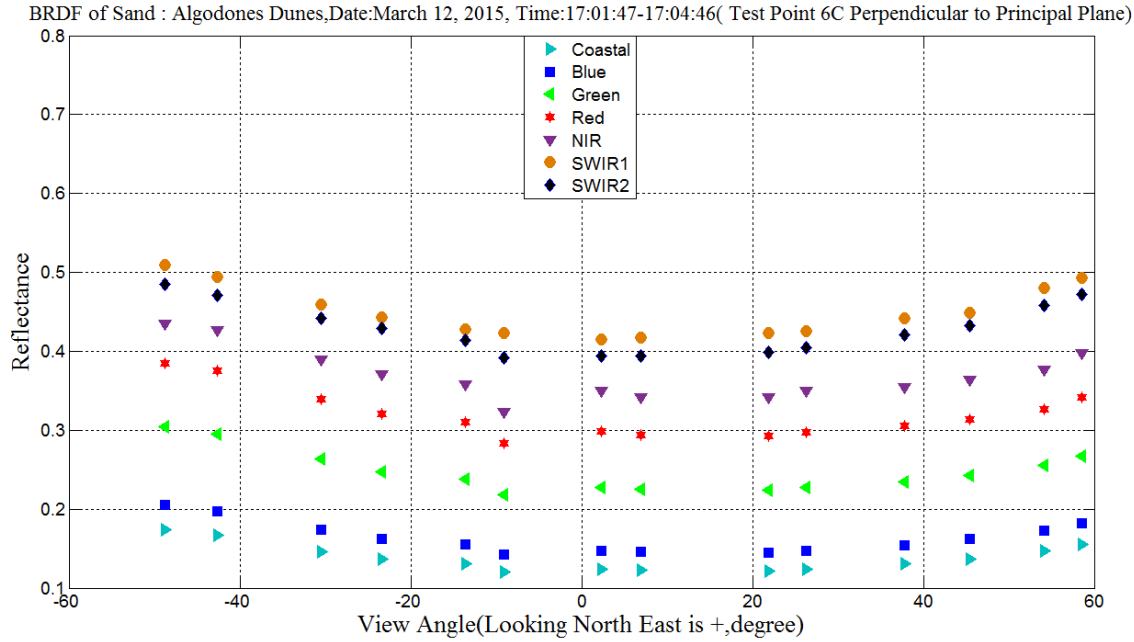

Figure A.6. 6C perpendicular to principal plane

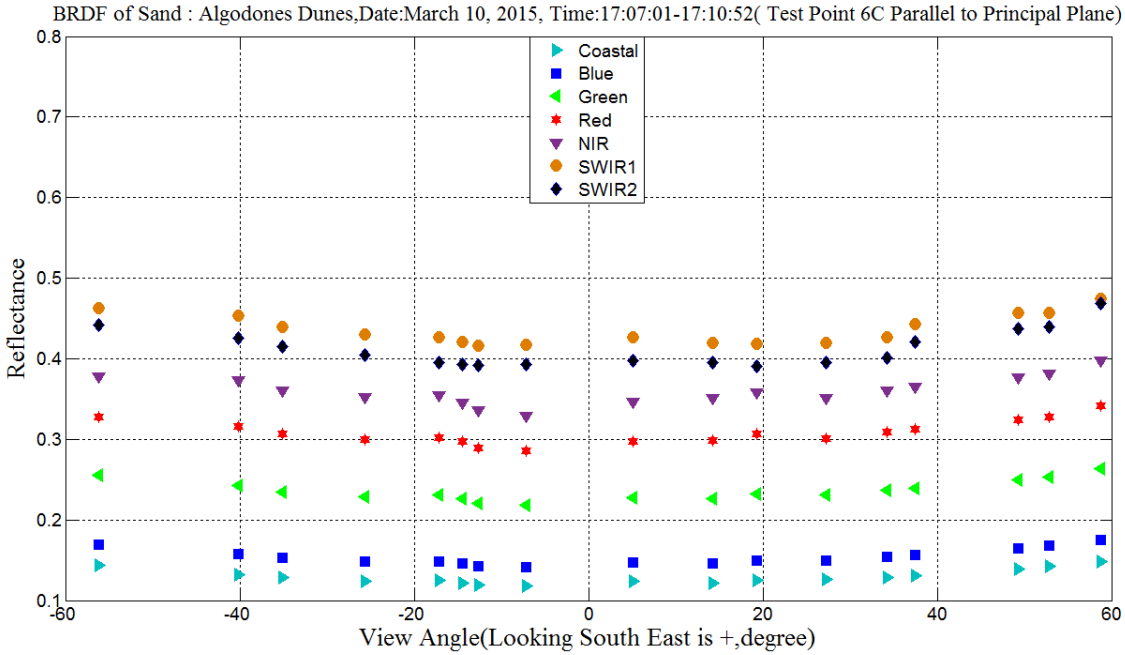

Figure A.7. 6C principal plane

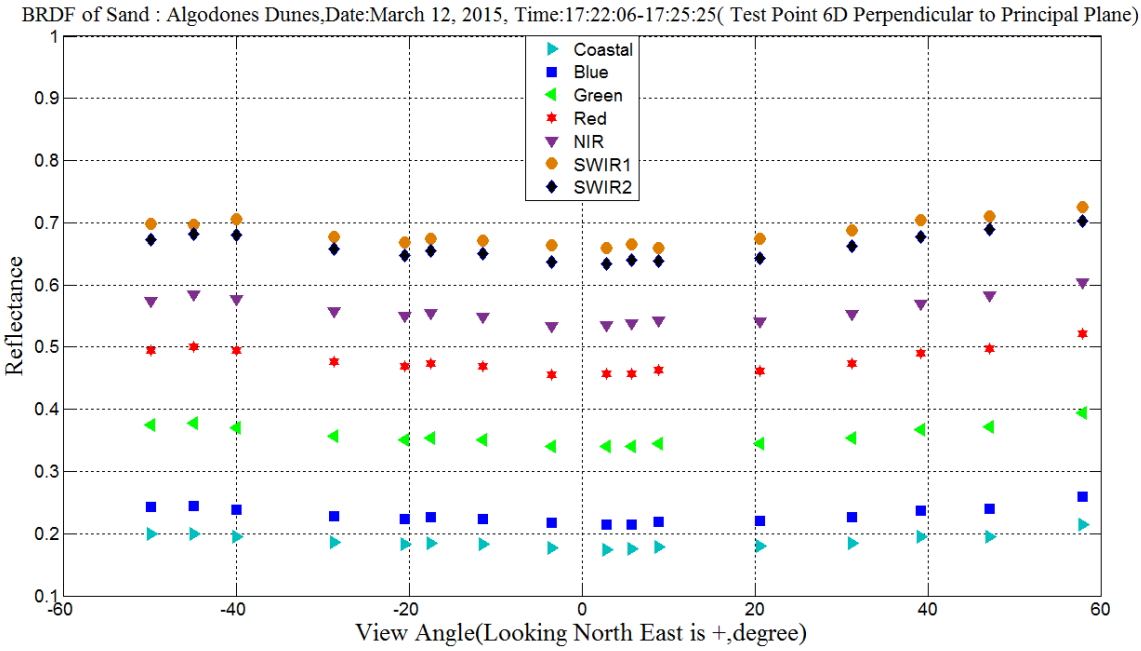

Figure A.8. 6D perpendicular to principal plane

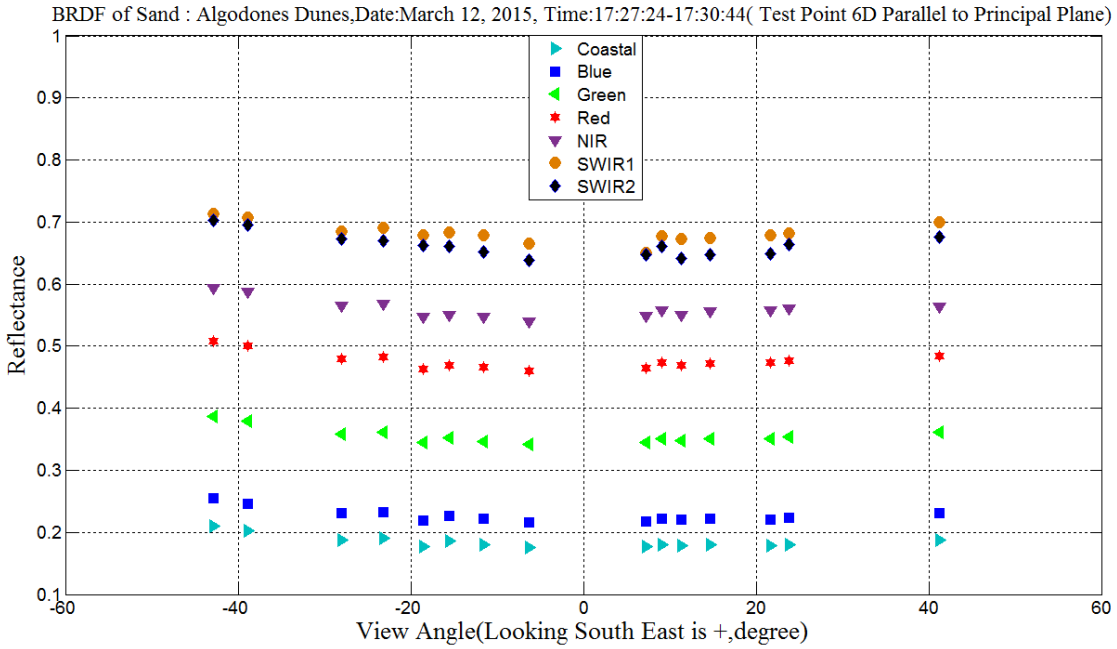

Figure A.9. 6D principal plane

A.1.1.2 Relative Scale

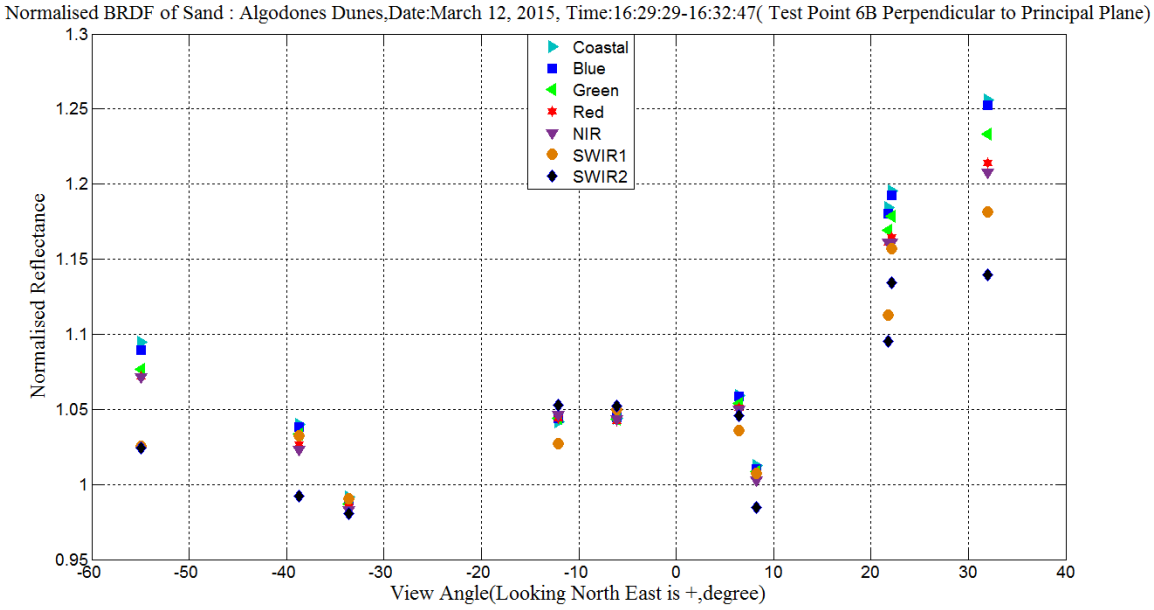

Figure A.10. Normalized 6B perpendicular to principal plane

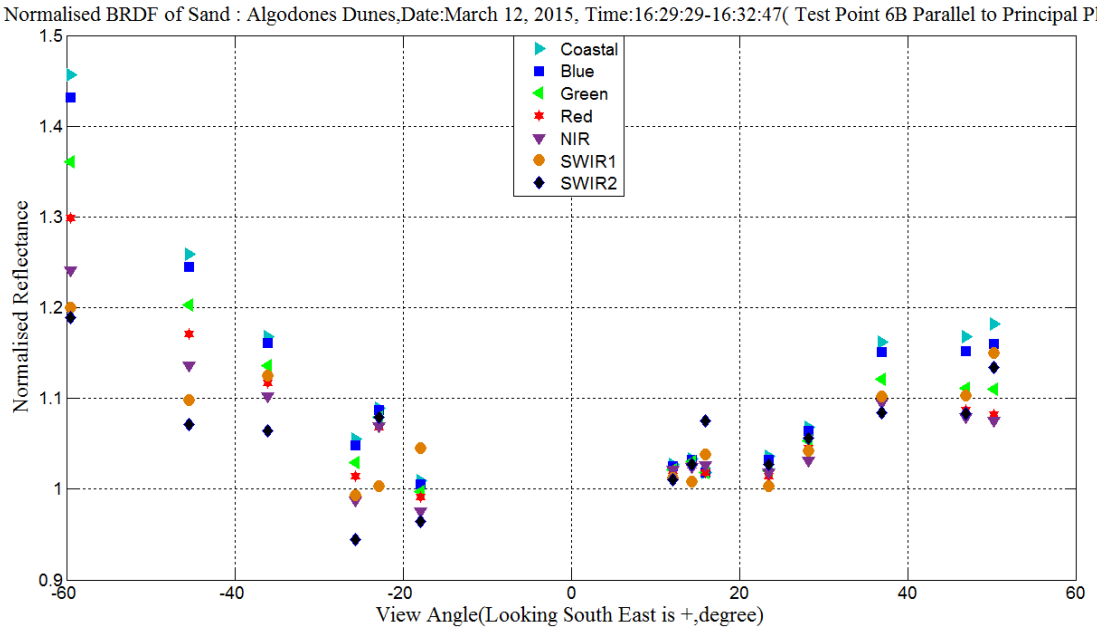

Figure A.11. Normalized 6B principal plane

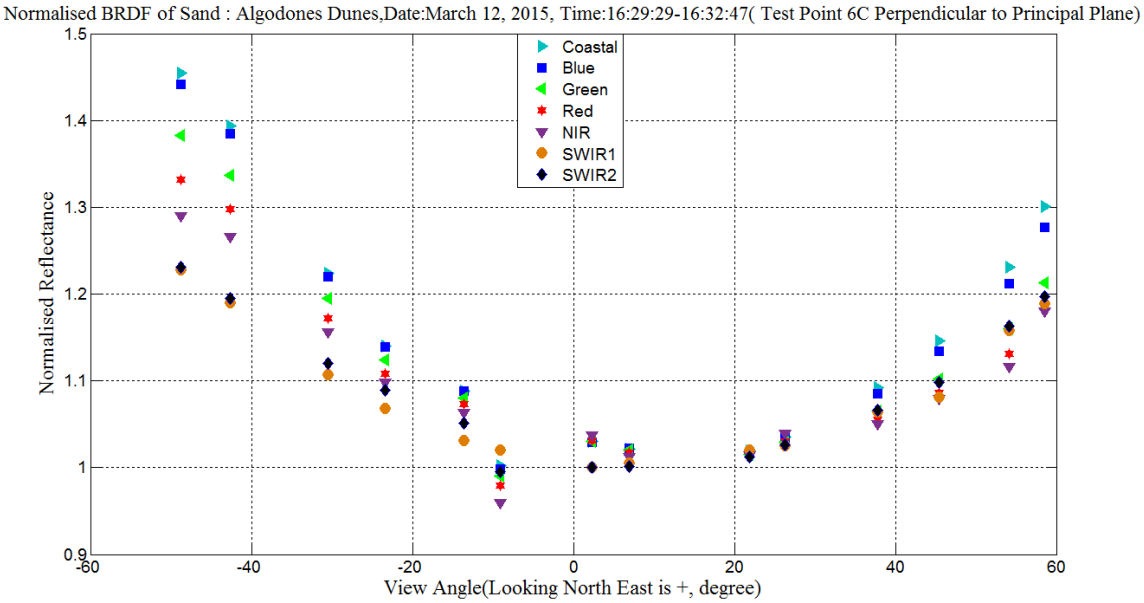

Figure A.12. Normalized 6C perpendicular to principal plane

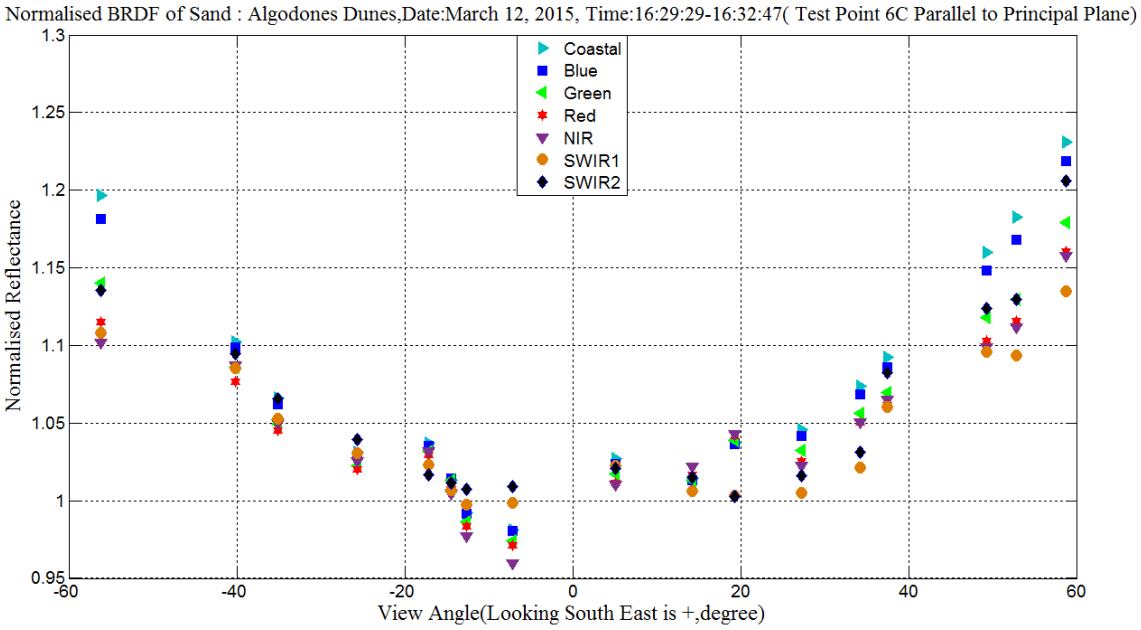

Figure A.13. Normalized 6C principal plane

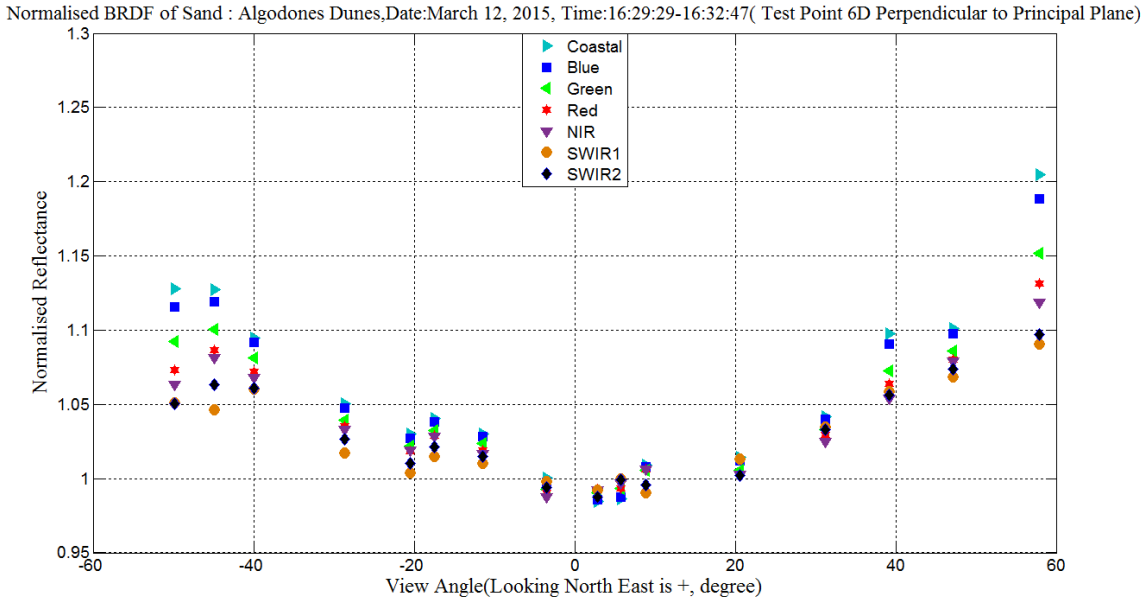

Figure A.14. Normalized 6D perpendicular to principal plane

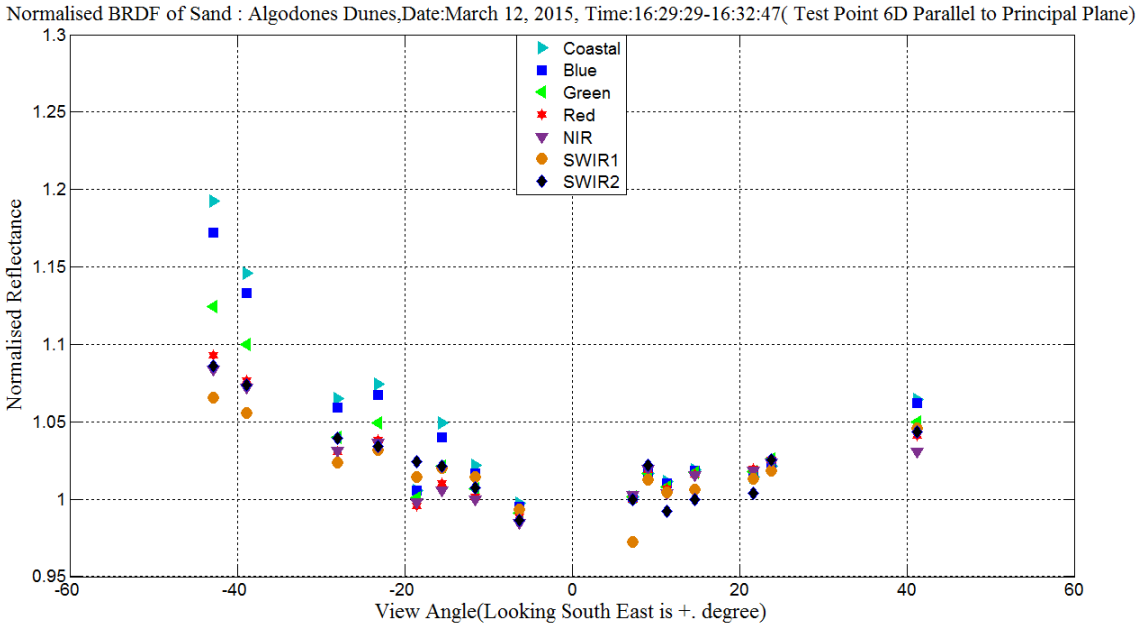

Figure A.15. Normalized 6D principal plane

A.1.2 Results from 10 March, 2015

A.1.2.1 Absolute Scale

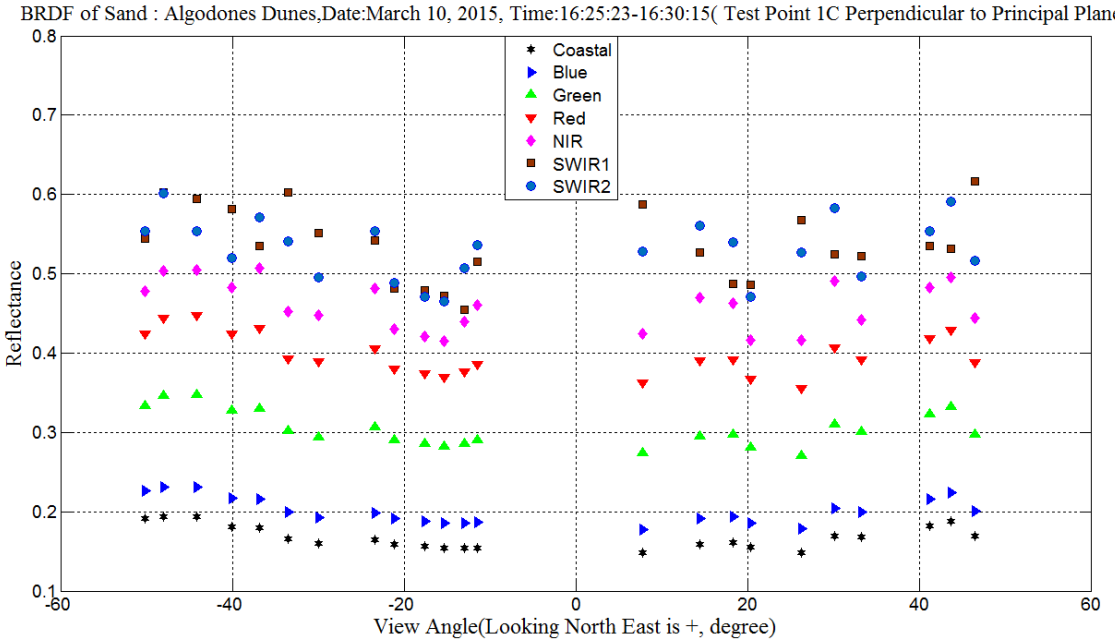

Figure A.16. 1C perpendicular to principal plane

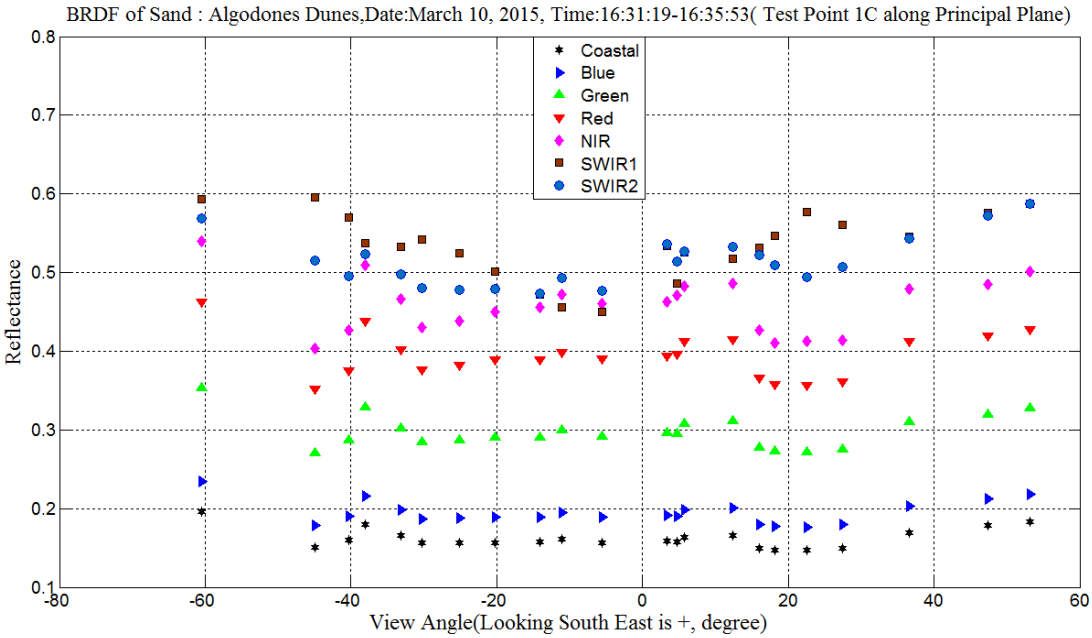

Figure A.17. 1C principal plane

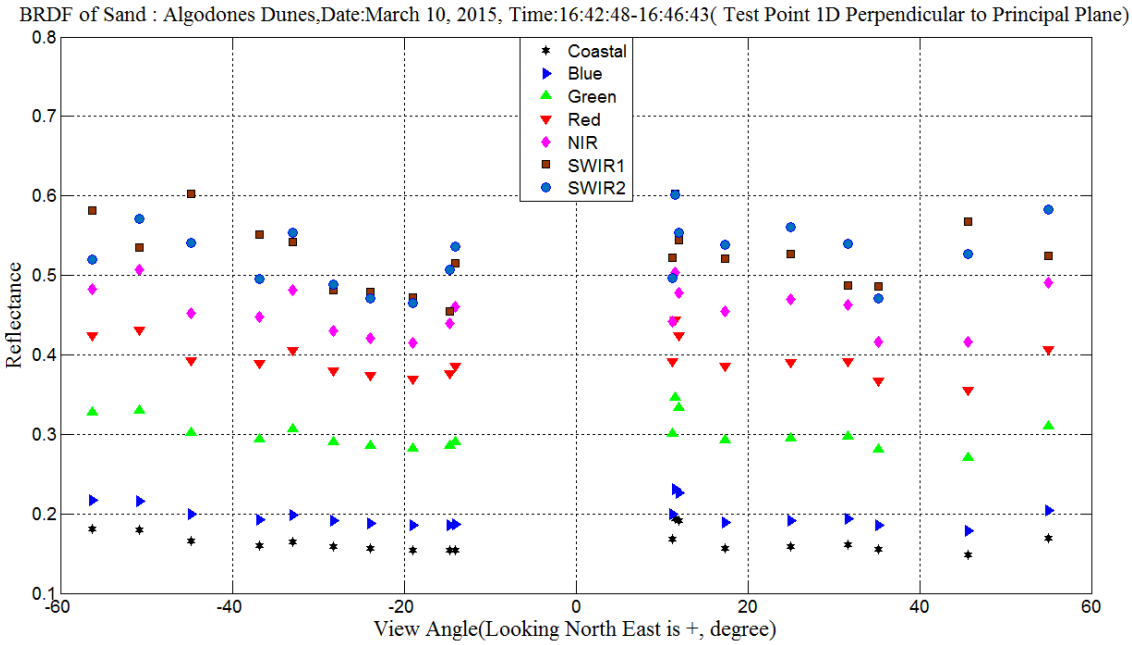

Figure A.18. 1D perpendicular to principal plane

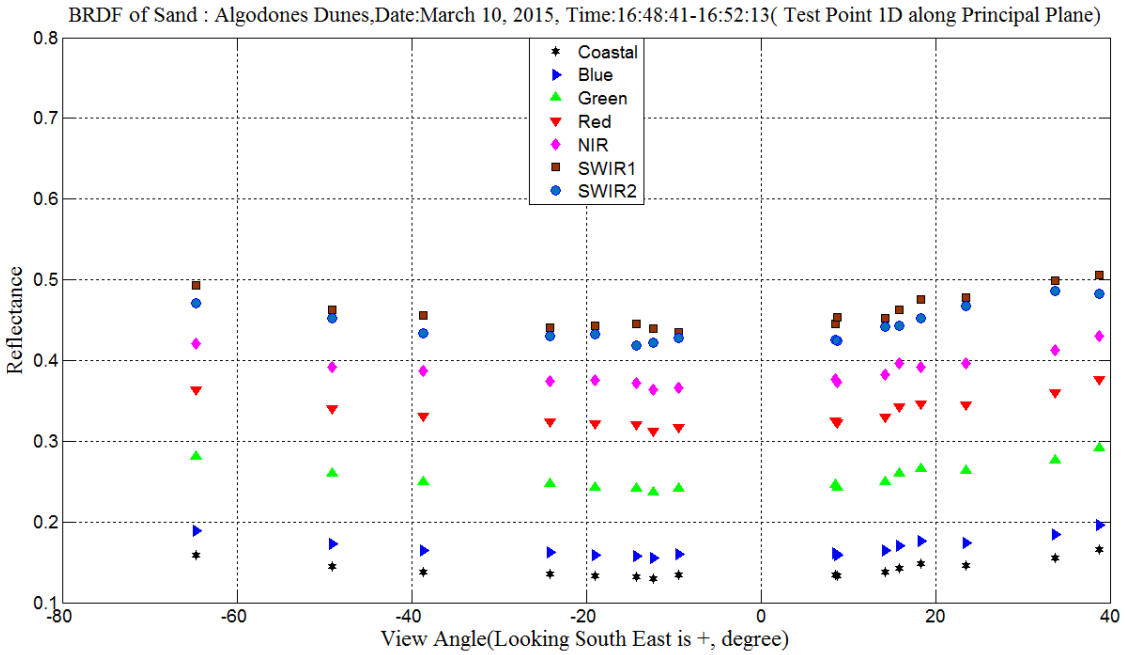

Figure A.19. 1D principal plane

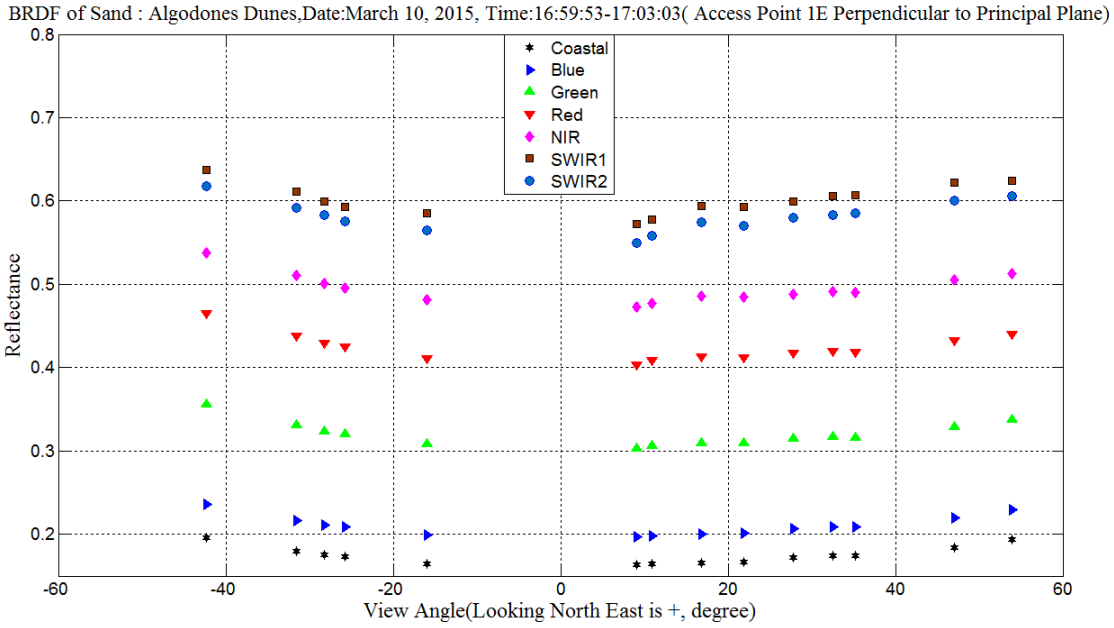

Figure A.20. 1E perpendicular to principal plane

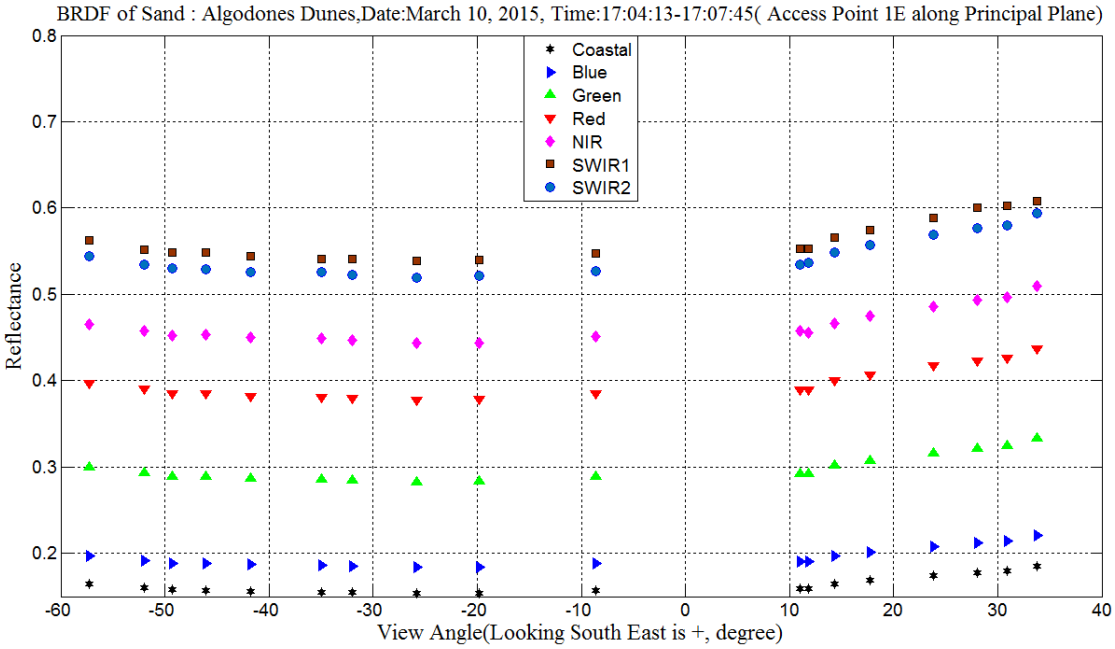

Figure A.21. 1E principal plane

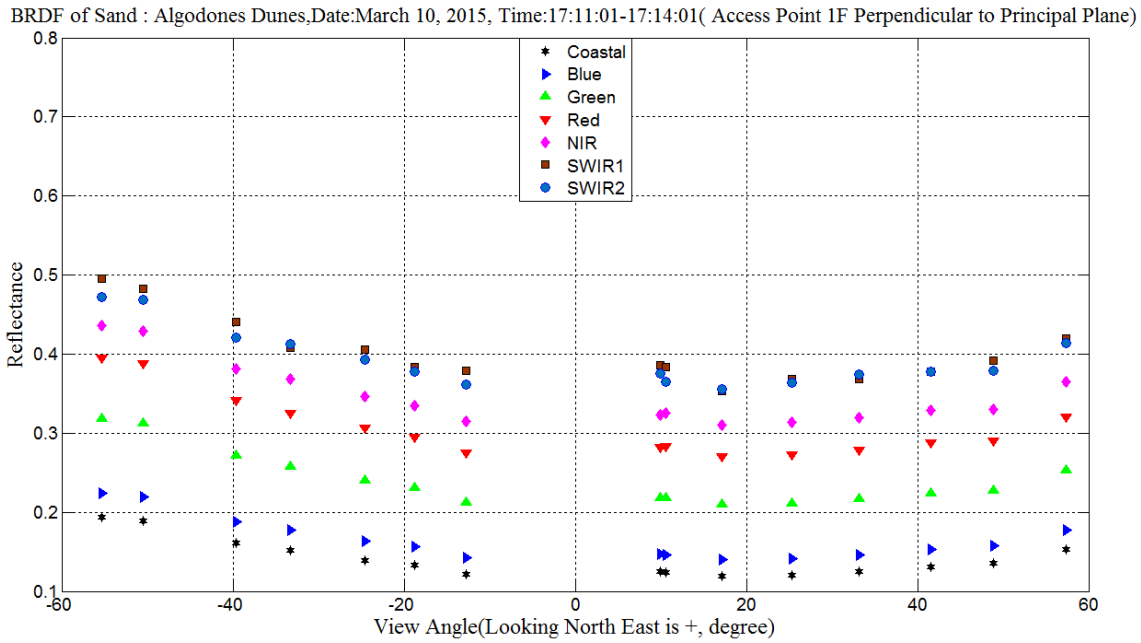

Figure A.22. 1F perpendicular to principal plane

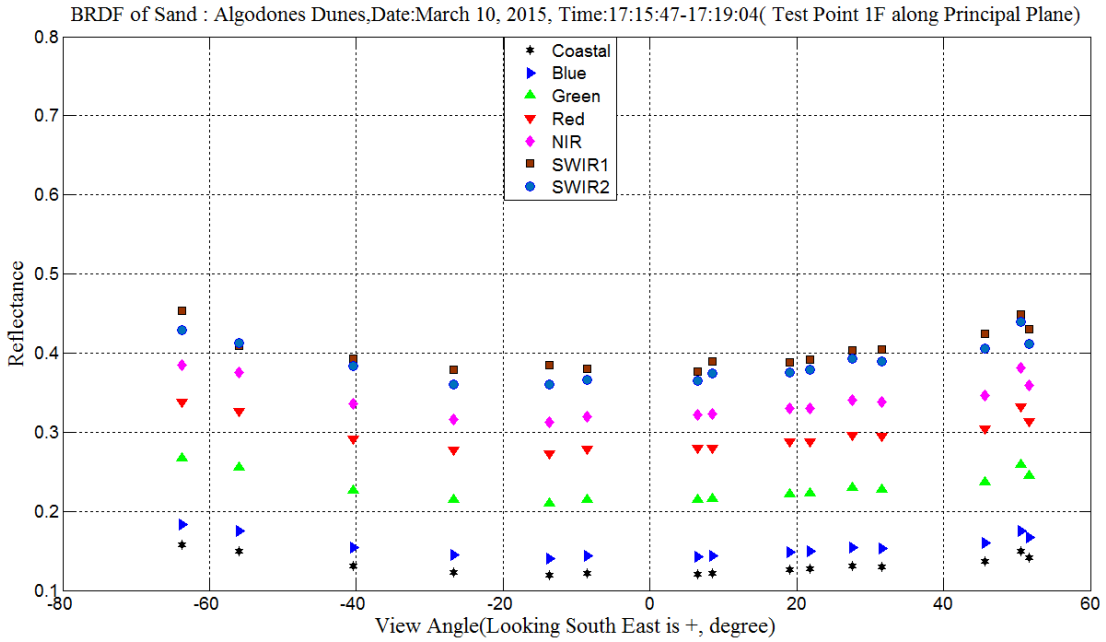

Figure A.23. 1F principal plane

A.1.2.2 Relative Scale

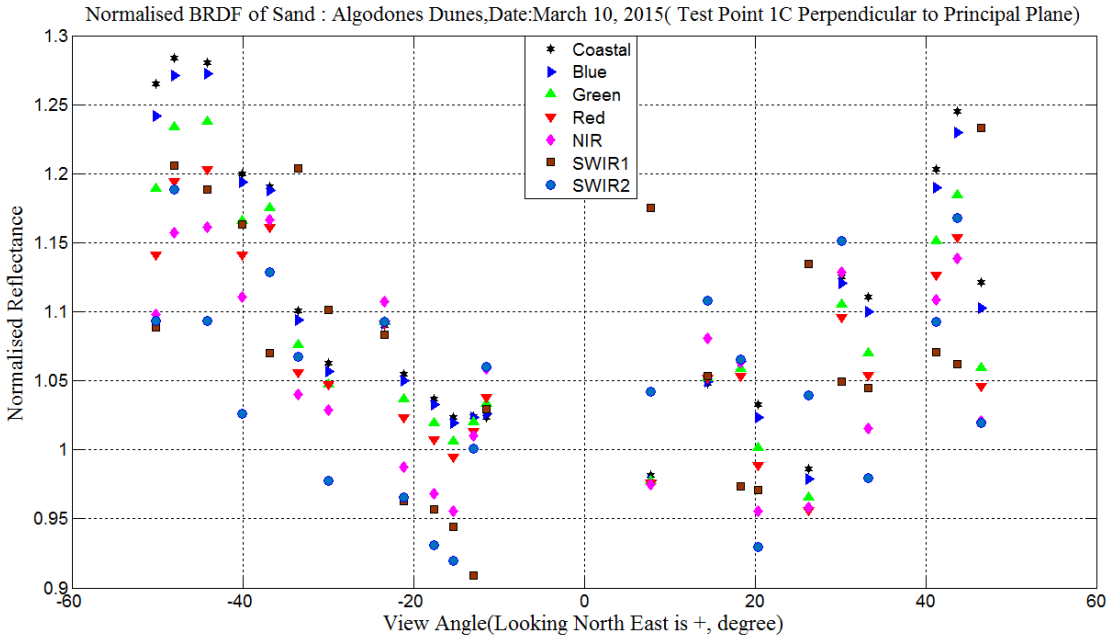

Figure A.24. Normalized 1C perpendicular to principal plane

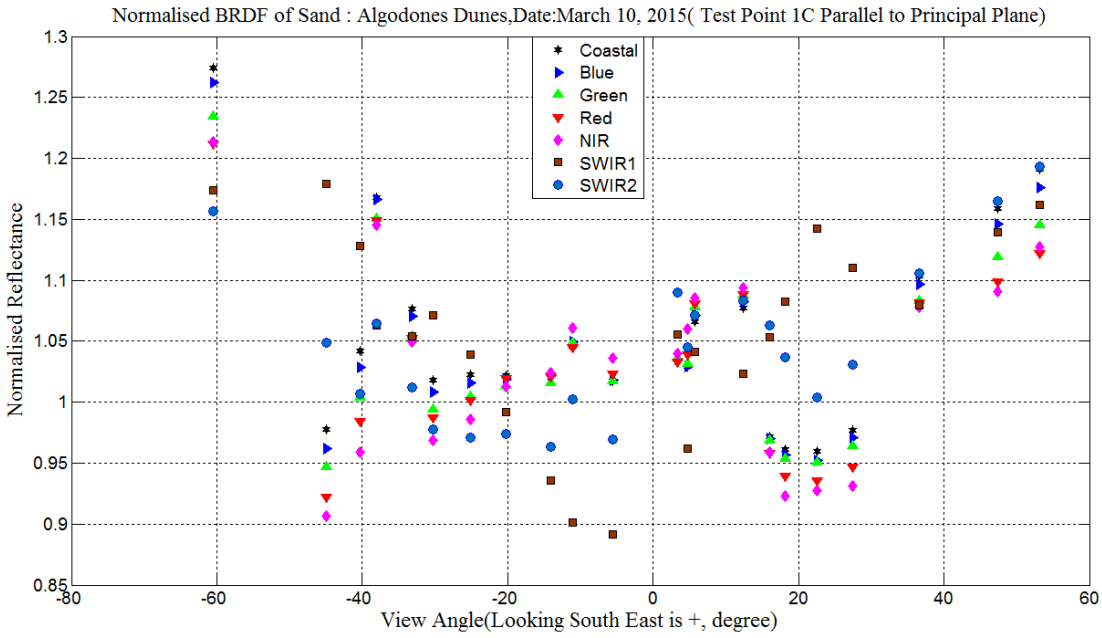

Figure A.25. Normalized 1C principal plane

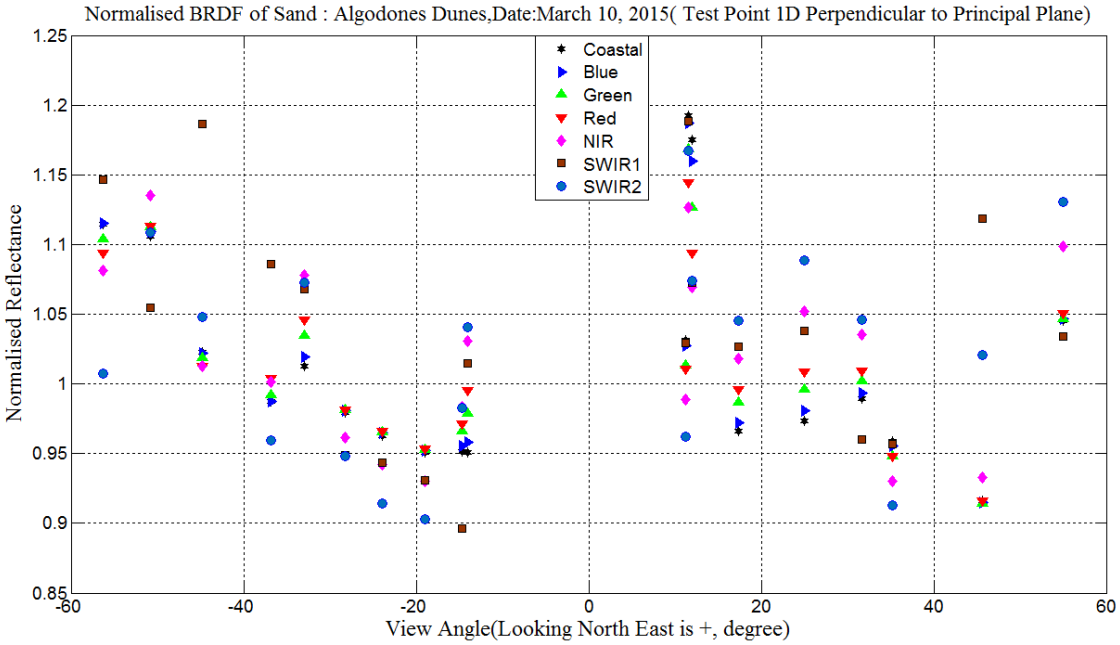

Figure A.26. Normalized 1D perpendicular to principal Plane

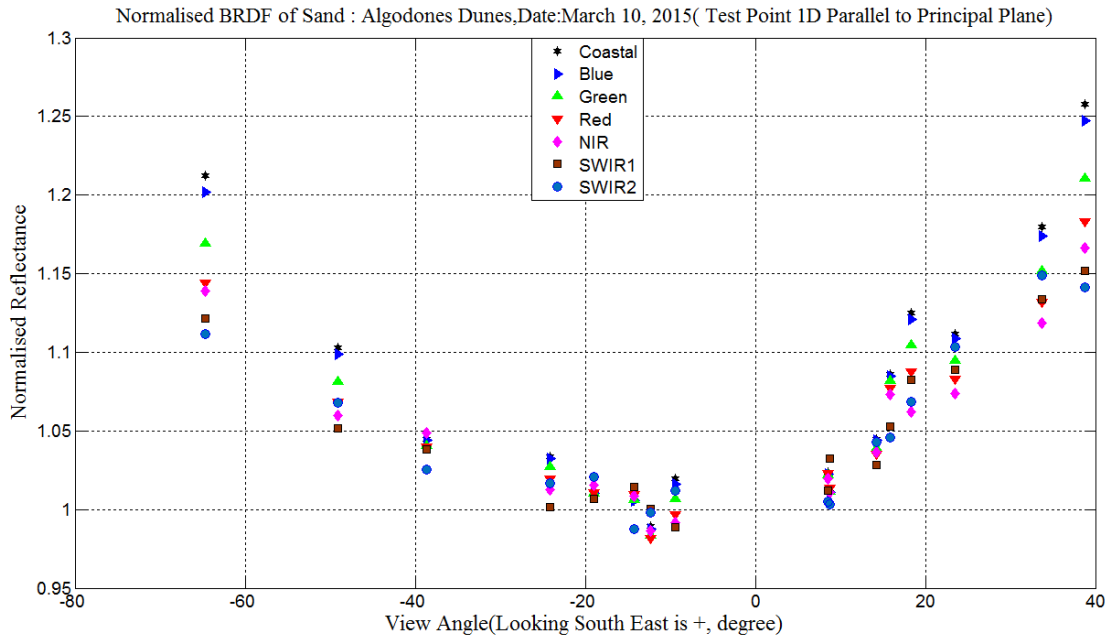

Figure A.27. Normalized 1D principal plane

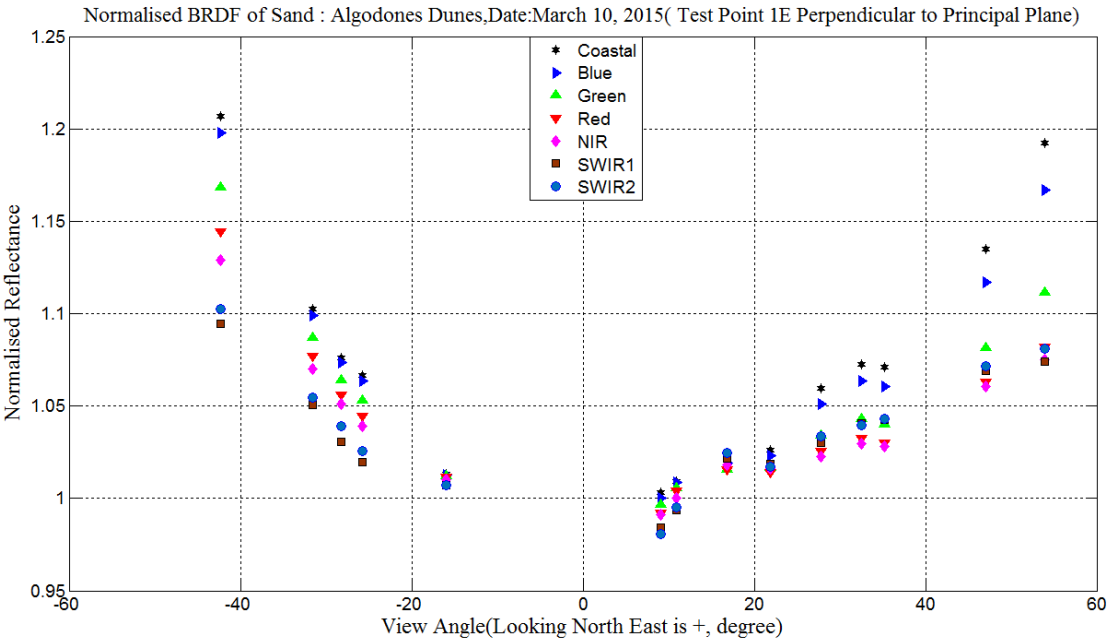

Figure A.28. Normalized 1E perpendicular to principal plane

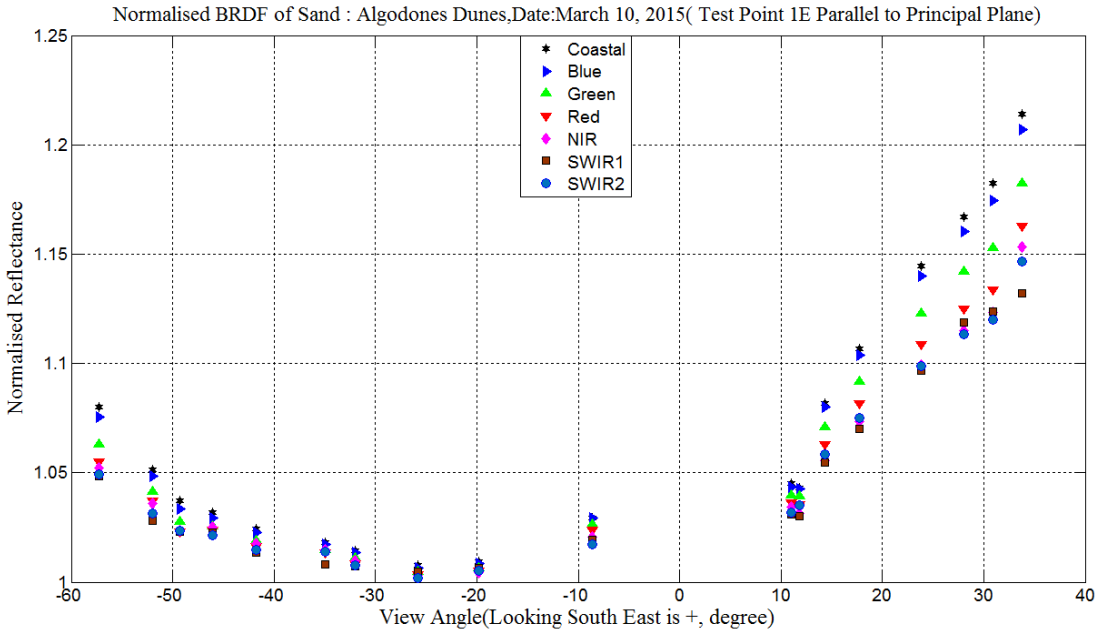

Figure A.29. Normalized 1E principal plane

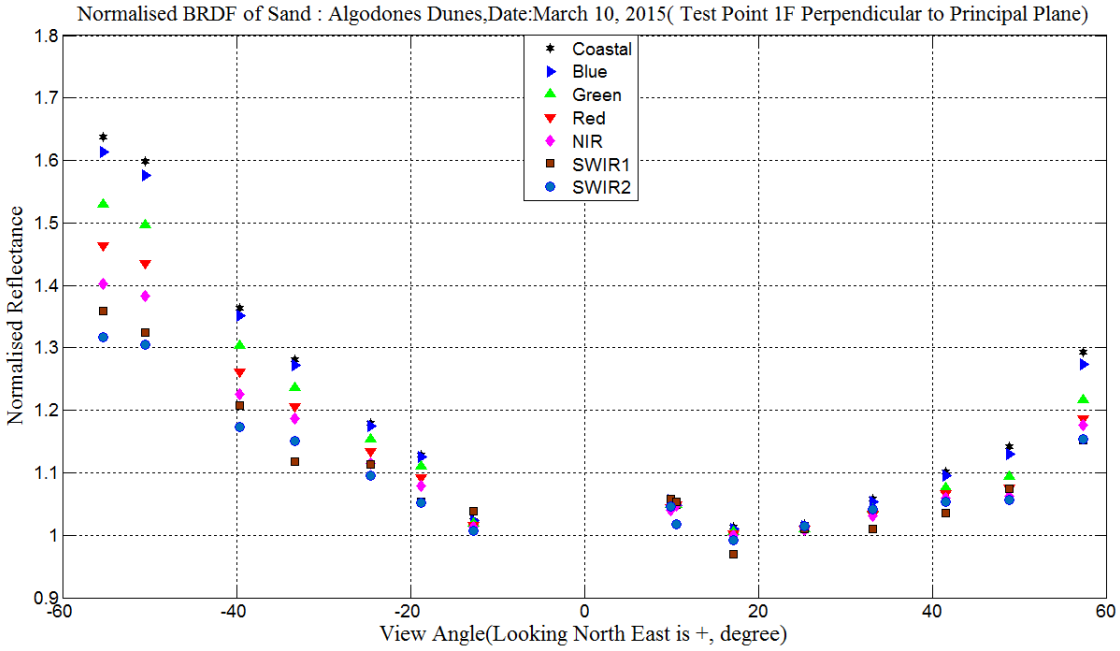

Figure A.30. Normalized 1F perpendicular to principal plane

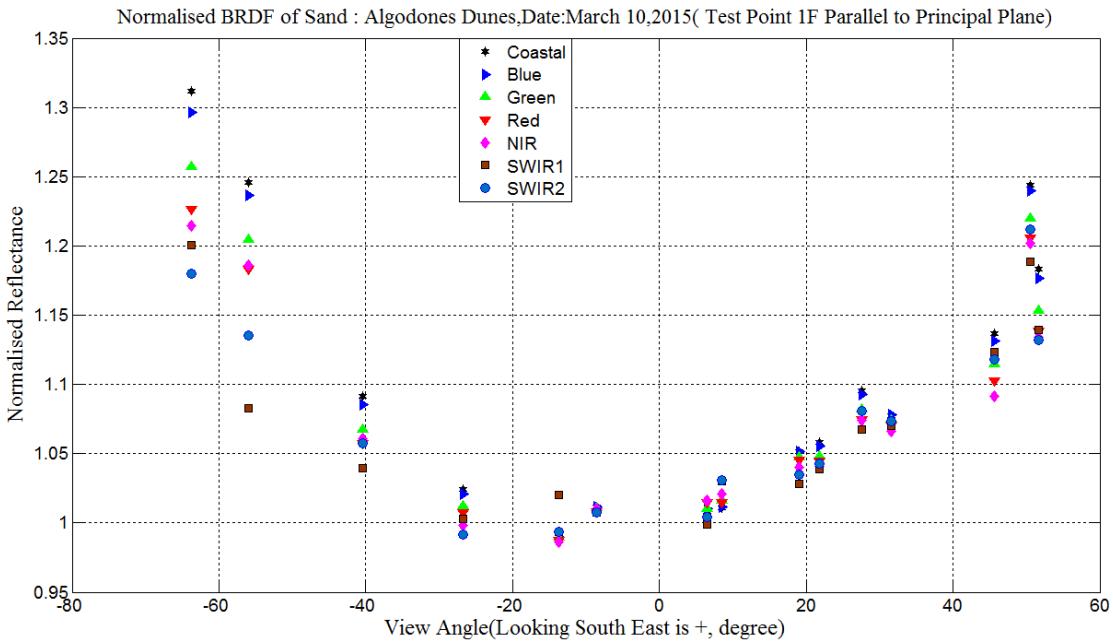

Figure A.31. Normalized 1F principal plane

REFERENCES

[1] J. R. Schott, *Remote Sensing: The Image Chain Approach, 2nd Edition*. Oxford University, 2007.

[2] P. R. Baumann, *History of remote sensing, satellite imagery*, [Online; accessed 25-May-2016], 2009. [Online]. Available: http://www.oneonta.edu/faculty/baumanpr/geosat2/RS%20History%20II/RS-History-Part-2.html/.

[3] N. R. Canada. (2015). Passive vs. active sensing, [Online]. Available: http://www.nrcan.gc.ca/earth-sciences/geomatics/satellite-imagery-air-photos/satellite-imagery-products/educational-resources/14639.

[4] C. Ichoku. (2014). Remote sensing, [Online]. Available: http://earthobservatory.nasa.gov/Features/RemoteSensing/.

[5] K. Z. Doctor, C. M. Bachmann, D. J. Gray, M. J. Montes, and R. A. Fusina, "Wavelength dependence of the bidirectional reflectance distribution function (brdf) of beach sands," *Applied optics*, vol. 54, no. 31, F243–F255, 2015.

[6] CEOS. (2014). Ceos cal/val portal, [Online]. Available: http://calvalportal.ceos.org/cvp/web/guest/literature1..

[7] K. Thorne, B. Markharn, P. S. Barker, and S Biggar, "Radiometric calibration of landsat," *Photogrammetric Engineering & Remote Sensing*, vol. 63, no. 7, pp. 853–858, 1997.

[8] D. Six, M. Fily, S. Alvain, P. Henry, and J.-P. Benoist, "Surface characterisation of the dome concordia area (antarctica) as a potential satellite calibration site, using spot 4/vegetation instrument," *Remote Sensing of Environment*, vol. 89, no. 1, pp. 83–94, 2004.

[9] B. Basnet, *"Identification of Worldwide Optimal Pseudo-Invariant Calibration Sites for Post-Launch Radiometric Calibration of Earth Observation Satellite Sensors"*. South Dakota State University, M.S. Thesis, 2010.

[10] K. Thome, B. Crowther, and S. F. Biggar, "Reflectance-and irradiance-based calibration of landsat-5 thematic mapper," *Canadian Journal of Remote Sensing*, vol. 23, no. 4, pp. 309–317, 1997.

[11] USGS. (2013). Remote sensing technologies, [Online]. Available: http://calval.cr.usgs.gov/sites_catalog_map.php..

[12] K. J. Thome, "Ground-look radiometric calibration approaches for remote sensing images in the solar reflective," *INTERNATIONAL ARCHIVES OF PHOTOGRAMMETRY REMOTE SENSING AND SPATIAL INFORMATION SCIENCES*, vol. 34, no. 1, pp. 255–260, 2002.

[13] B. L. Markham, K. J. Thome, J. A. Barsi, E. Kaita, D. L. Helder, J. L. Barker, and P. L. Scaramuzza, "Landsat-7 etm+ on-orbit reflective-band radiometric stability and absolute calibration," *IEEE Transactions on Geoscience and Remote Sensing*, vol. 42, no. 12, pp. 2810–2820, 2004.

[14] D. L. Morstad and D. L. Helder, "Use of pseudo-invariant sites for long-term sensor calibration," in *IGARSS 2008-2008 IEEE International Geoscience and Remote Sensing Symposium*, IEEE, vol. 1, 2008, pp. I–253.

[15] P. Teillet, J. Barsi, G Chander, and K. Thome, "Prime candidate earth targets for the post-launch radiometric calibration of space-based optical imaging instruments," in *Optical Engineering+ Applications*, International Society for Optics and Photonics, 2007, 66770S–66770S.

[16] R. Bhatt, *Consistent radiometric calibration of Landsat-1 through-5 MSS sensors using pseudo-invariant calibration sites*. South Dakota State University, 2009.

[17] A. Shrestha, *A Validation and Update of Landsat MSS sensor Calibration Using Pseudo-Invariant Sites and Dark Targets*. South Dakota State University, 2015.

[18] C. Coburn and D. Peddle, "A low-cost field and laboratory goniometer system for estimating hyperspectral bidirectional reflectance," *Canadian Journal of Remote Sensing*, vol. 32, no. 3, pp. 244–253, 2006.

[19] Z. Wang, C. A. Coburn, X. Ren, and P. M. Teillet, "Effect of surface roughness, wavelength, illumination, and viewing zenith angles on soil surface brdf using an imaging brdf approach," *International Journal of Remote Sensing*, vol. 35, no. 19, pp. 6894–6913, 2014.

[20] U. S. N. B. of Standards and F. E. Nicodemus, *Geometrical considerations and nomenclature for reflectance*. US Department of Commerce, National Bureau of Standards, 1977, vol. 160.

[21] P. P. Roosjen, J. G. Clevers, H. M. Bartholomeus, M. E. Schaepman, G. Schaepman-Strub, H. Jalink, R. Van Der Schoor, and A. De Jong, "A laboratory goniometer system for measuring reflectance and emittance anisotropy," *Sensors*, vol. 12, no. 12, pp. 17 358–17 371, 2012.

[22] Panalytical. (2016). Asd inc, [Online]. Available: http://www.asdi.com/products-and-services.

[23] J. Estornell, J. M. Martí-Gavliá, M. T. Sebastiá, and J. Mengual, "Principal component analysis applied to remote sensing," *Modelling in Science Education and Learning*, vol. 6, pp. 83–89, 2013.

[24] J. A. Richards, *Remote Sensing Digital Image Analysis An Introduction, 4th Edition*. Springer-Verlag, 2006.

[25] C. M. Bachmann, M. J. Montes, C. E. Parrish, R. A. Fusina, C. R. Nichols, R.-R. Li, E. Hallenborg, C. A. Jones, K. Lee, J. Sellars, *et al.*, "A dual-spectrometer approach to reflectance measurements under sub-optimal sky conditions," *Optics express*, vol. 20, no. 8, pp. 8959–8973, 2012.

[26] W. M. Trochim. (2006). General linear model, [Online]. Available: http://www.socialresearchmethods.net/kb/genlin.php.

[27] R. J. Freund and W. J. Wilson, *Statisctical Methods, Second Edition*. Academic Press, 2003.

[28] B. Winter. (2014). A very basic tutorial for performing linear mixed effects analyses (tutorial 2), [Online]. Available: http://www.bodowinter.com/tutorial/bw_LME_tutorial2.pdf.

[29] Broandband Halogen Fiber Optic Illuminator. [Online]. Available: https://www.thorlabs.com/newgrouppage9.cfm?objectgroup_id=884&pn=OSL2B.